

ABSTRACT

Title of Dissertation: **LARGE EDDY SIMULATION OF
BOUNDARY LAYER COMBUSTION**

Luis Bravo, PhD, 2013

Dissertation directed by: Associate Professor, Arnaud Trouve,
Fire Protection Engineering Department
Mechanical Engineering Department

Numerical simulations of turbulent non-premixed flames occurring in the presence of solid surfaces is a prevalent topic of interest due to the complexity of the near wall physics and the technical modeling challenges it presents. Near wall combustion phenomena is relevant in a variety of combusting environments including but not limited to the occurrence of fire spread, as a result of a heating load to a flammable wall leading to fire growth in enclosure settings; and in engine combustion configurations where the interaction with a cooled surface combined with occurrences of short flame wall distances can lead to extinction events adversely affecting combustion performance. The interaction between the flame and surface can result in a reduction of flame strength near the cold wall region while gas phase heat fluxes can take peak values at flame contact.

To address the aforementioned modeling challenges, an advanced computational fluid dynamics (CFD) solver has been developed by adapting a preexisting numerical simulation solver from a boundary layer code to a code with variable mass density and combustion capabilities to produce high-fidelity simulations of turbulent non-premixed wall-flames. A series of verification studies have been developed using several benchmark laminar flow problems for the following canonical configurations: a binary diffusion controlled mixing problem, Poiseuille flow with heat transfer, and classical Blasius boundary layer flow. The turbulence LES modeling capability is validated by performing wall-resolved heated/non-heated turbulent channel flow and transpired boundary layer simulations to capture the effects of heat and mass transfer on the turbulent eddy structure and statistics. Lastly, an application of a simplified non-premixed wall flame configuration is presented in which the fuel corresponds to pyrolysis products supplied by a thermally-degrading flat sample of polymethyl methacrylate (PMMA) and the oxidizer corresponds to a cross-flow of ambient air with controlled mean velocity and turbulence intensities. Comparisons between numerical results and experimental data are made in terms of flame length, wall surface heat flux and flame structure and the ability of the solver in modeling non-premixed turbulent wall-flames is successfully demonstrated. The solver extends the present state of the art in fire modeling (limited to laminar flows) by providing a high quality numerical tool to study the heat transfer aspects of turbulent wall flame phenomena

LARGE EDDY SIMULATION OF BOUNDARY LAYER COMBUSTION

By

LUIS BRAVO

Dissertation submitted to the Faculty of the Graduate School of the
University of Maryland, College Park, in partial fulfillment
of the requirements for the degree of
Doctor of Philosophy
2013

Advisory Committee:

Professor Arnaud Trouve (FPE), Chair and Adviser

Professor Christopher Cadou (AE), Dean's Representative

Professor Andre Marshall (FPE), Regular Member

Professor Stanislav Stoliarov (FPE), Regular Member

Professor Emeritus James Quintiere (FPE), Regular Member

Professor Emeritus James Wallace (ME), Regular Member

© Copyright by

LUIS BRAVO

2013

Dedication

This thesis is dedicated to the memory of Luis Bravo and Azucena Bravo.

Acknowledgements

I would like to thank my adviser Dr. Arnaud Trouve and co-adviser Dr. Ugo Piomelli for providing the opportunity to work in the field of turbulence modeling through a CBET National Science Foundation Project focusing on numerical simulation of turbulent non-premixed flames. I also would like to show gratitude to my committee members Dr. Christopher Cadou, Dr. Andre Marshall, Dr. Stanislav Stoliarov, Dr. James Quintiere, and Dr. James Wallace for their support and providing their expert feedback to my work and for sharing their wealth of knowledge.

During my tenure at Maryland, I have been the recipient of several doctoral fellowship awards from the Alfred P. Sloan Foundation, and the National GEM Foundation programs. I would like to recognize the faculty who encouraged me to pursue these fellowships: Dr. Darryll Pines Dean of the School of Engineering and University Representative of the Sloan Foundation Program, and Dr. Damian Rouson GEM Employer and sponsor through Sandia National Laboratories, Combustion Reacting Facility. I also would like to acknowledge the departments who have supported me through several teaching assistantships: Mechanical Engineering, Fire Protection Engineering and the Office of Advanced Engineering Education, I have been fortunate to be involved in these programs. Thanks are also due to Ms. Rosemary Parker from the Center for Minorities in Science and Engineering (CMSE) for giving me the privilege to coordinate its recruitment engineering summer programs and for their immense support along my academic career.

Thanks to all the members of our CFD group for providing such a pleasant work environment, and sharing their vision on several technical and non-technical topics, they

are: Dr. Vivien Lecoustre, Ayodeji Ojofeitimi, Andrew Voegele, Zohreh Gorbani, Sebastian Vilfayeau and Ben Trettel.

Last but not least, I would like to thank the immense support from my family along my entire academic career, none of this would have been possible without their encouragement; and to my love Irani who has been my inspiration since the day I have met her.

Table of Contents

Dedication	ii
Acknowledgements	iii
List of Tables	viii
List of Figures	ix
Chapter 1: Introduction	1
1.1 Motivation for Computational Research in Fire Modeling	1
1.2 Physical Description of Fire Phenomena	3
1.3 Emergence of CFD based fire modeling	5
1.4 Fire Modeling Constituents	8
1.5 Introduction/Literature Review on Turbulent Flow Modeling	13
1.5.1 Boundary Layer Flows	16
1.5.2 Transport of scalars in wall-bounded flows	21
1.6 Boundary Layer Combustion – Flame Spread	24
1.7 Research Aims and Thesis Contribution	26
1.7.1 Research Aims	26
1.7.2 Thesis Contribution	27
1.8 Thesis Overview	32
1.8.1 Chapter 2. Numerical Methods	32
1.8.2 Chapter 3. Verification using benchmark laminar flow problems	33
1.8.3 Chapter 4. LES Validation of wall-bounded flows	33
1.8.4 Chapter 5. LES Application of turbulent wall-fires	34
1.8.5 Chapter 6. Conclusions and Future Work	34
Chapter 2: Numerical Methods	35
2.1 Governing Equations	36
2.2 Smagorinsky modeling	38
2.3 Residual stress decomposition	40
2.4 Dynamic modeling	40
2.5 Extension to a variable mass density formulation	44

2.6	Governing Equations and Filtering	45
2.7	Dynamic Modeling.....	46
2.7.1	SGS scalar flux	50
2.8	Time Advancement	52
2.8.1	Time advancement and iterative scheme	52
2.8.2	Discrete Equation.....	54
2.9	Iterative Scheme.....	58
2.10	QUICK scheme for scalar transport	64
2.11	Single Step Mixture Fraction Combustion Model	65
2.12	CHEMKIN Thermodynamic Model	66
2.13	Inflow Boundary Conditions.....	68
2.13.1	Synthetic Turbulent Inflow Generation.....	68
2.13.2	Synthetic Turbulence.....	69
2.13.3	Reynolds Stress Controller	71
2.14	Outflow Boundary Conditions	72
2.14.1	Orlansky conditions.....	72
2.14.2	Freestream boundary conditions.....	73
2.15	Summary	73
Chapter 3:	Verification	74
3.1	Verification procedure.....	76
3.2	One-Dimensional Case Study: Order of Accuracy Analysis	78
3.2.1	Isothermal Binary Mixing	78
3.2.2	Analytical Solution.....	79
3.3	Two-Dimensional Case Study: Order of Accuracy Analysis.....	87
3.3.1	Poiseuille Flow with heat transfer	87
3.4	Classical Boundary Layer Flow	92
3.4.1	Blasius Flow.....	92
3.5	Summary	99
Chapter 4:	Validation.....	100
4.1	Turbulence in Adiabatic Channel Flows.....	102

4.1.1	Wall bounded Terminology and Resolution Requirements.....	103
4.1.2	Computational Domain.....	105
4.1.3	Results.....	108
4.2	Turbulence in Channel Flow with Variable Property	114
4.2.1	Wall-Bounded Terminology and Resolution Requirements.....	114
4.2.2	Computational Domain.....	115
4.2.3	Results.....	117
4.3	Validation of Synthetic Turbulent Inflow Generation	125
4.4	ZeroPressure Gradient Turbulent Boundary Layer	131
4.3.1	Turbulent Recovery Length	133
4.4	The Effect of Transpiration through a Porous Surface	136
4.4	Summary	141
Chapter 5: Turbulent Wall-fires.....		142
5.1	Gas-Phase Combustion Model (PMMA).....	144
5.2	Numerical Configuration.....	146
5.3	Wall-flame results	150
5.4	Summary	155
Chapter 6: Conclusions and Future Work.....		156
6.1	Conclusions	156
6.2	Key Contributions	156
6.3	Future Work	159
Appendix A: Finite Differences Discretization		161
Bibliography		169

List of Tables

Table 1. Physical parameter table for 1-dimensional mixing problem.	82
Table 2. Computational parameter table for 1-dimensional mixing problem. The table presents initial conditions, boundary conditions, and thermodynamic models.	82
Table 3. Computational parameter table for Poiseuille flow with heat-transfer.	88
Table 4. Physical parameter table for Blasius boundary layer flow.	93
Table 5. Computational parameter table for Blasius boundary layer flow with heat transfer. The table presents initial conditions, boundary conditions, and thermodynamic models.	93
Table 6. Physical parameter table for the turbulent channel flow configuration. The table presents initial conditions, boundary conditions, and turbulence models.	107
Table 7. Physical parameter table for the turbulent channel flow configuration. The table presents initial conditions, boundary conditions, and turbulence models.	116
Table 8. Turbulent heated channel with variable properties; comparison of wall properties between les3D-mp results and reference DNS simulations of Nicoud et al [72].	124
Table 9. Physical parameter table for turbulent boundary layer flow configuration. The table presents initial conditions, boundary conditions, controller and turbulence models.	132

List of Figures

Figure 1. Physical processes occurring in an over-ventilated enclosure fire in its development stage (pre-flashover). Notice the development of a fire-plume and lateral ceiling jet providing the mechanism for smoke filling; also observe a natural stratification of hot upper layer (smoke gases) and a cooler lower layer (fresh-air) leading to a description of a zone-model approach. (Figure credit to SFPE handbook, Chapter 9)	5
Figure 2. Turbulent flow energy spectrum $E(K)$ variations with wavenumber, k . The modeling differences between Direct Numerical Simulations (DNS) and Large-eddy simulations (LES) are presented in terms of resolved scales (wavenumbers). Subgrid scale LES model is highlighted demonstrating the need to model the small diffusive spatial scales.....	14
Figure 3. Scalar staggered cell. The right-hand side of the scalar equation is evaluated at the center of the spatio-temporal cell, identified by a black dot.	59
Figure 4. Momentum staggered cell. The right hand side of this equation is evaluated at the bottom right of the spatio-temporal cell, identified by a black dot.	61
Figure 5. Flow chart showing the mass density iterative scheme and time integration advancement.	63
Figure 6. Schematic of the one-dimensional mixing problem. As depicted in the figure, the problem is set up such that a thin layer of light fluid (i.e., fuel) mixes with a heavier column of fluid (i.e., air) due to molecular diffusion.....	79
Figure 7. Temporal variations of peak mass-density ratio (ratio of light over heavier fluid) in the system, compared to the freestream mass-density.	81
Figure 8. Comparison of 1-dimensional mixing problem between numerical solution obtained with LES-BLAC and analytical model (Solid line represents the theoretical solution); comparisons are made for: mass density, wall-normal velocity, and mixture fraction at twenty time units	83
Figure 9. Order of accuracy analysis for mixing variables: mixture fraction, mass density and velocity (a) grid refinements demonstrate the second order accuracy of the spatial scheme (b) time-step refinements demonstrate the 2nd order accuracy of the time integration scheme.	86
Figure 10. Schematic of weakly compressible Poiseuille type canonical flow with heat-transfer. Heating is introduced through a hot isothermal wall on top at 900K.	88
Figure 11. Iso-contours of flow variables: streamwise velocity, temperature, and mass-density for Poiseuille flow with heat transfer.	89
Figure 12. Profiles of streamwise velocity and temperature (Kelvin) for Poiseuille flow with heat transfer. Comparison is made with the analytical solution.	90

Figure 13. Order of accuracy analysis for Poiseuille channel flow variables: streamwise velocity and temperature: grid refinements demonstrate the second order accuracy of the spatial scheme. 91

Figure 14. Spatial variations of wall-shear stress profiles for Blasius boundary layer type flow; comparison to analytical solution and demonstration of the effect of the wall-heating on the shear-stress distribution..... 94

Figure 15. Iso-contours of streamwise and wall-normal velocity in Blasius boundary layer type flow with an isothermal heated wall at $T_{wall} = 450K$ 95

Figure 16. Iso-contours of pressure and temperature in Blasius boundary layer type flow with an isothermal heated wall at $T_{wall} = 450K$ 96

Figure 17. Schematic of the channel configuration showing spatial coordinates and domain size. 107

Figure 18. Statistical presentation of a turbulent channel flow results for $Re\tau = 400$. Top left figure shows the mean velocity profiles in wall-units, the right figure shows the turbulent intensity profiles; Symbols (\ominus) are current LES simulations and the solid black line (-) is the reference DNS. 109

Figure 19. Reynolds shear stress normalized by friction velocity, $Re = 400$; The solid black line represents the total shear stress (summation of each component) across the channel. 111

Figure 20. (a) Instantaneous three dimensional velocity iso-contours (b) Turbulent eddy structure presented using the Q-criterion ($Q=3$) visualization technique – the back plane shows u-velocity iso-contours..... 113

Figure 21. Schematic of the heated channel configuration showing spatial coordinates and isothermal boundary conditions..... 116

Figure 22. First order statistical analysis: (a) Mean velocity and (b) mean temperature profiles across the channel in line-units; for both cold and hot walls..... 119

Figure 23. First order statistical analysis: (a) Mean velocity and (b) mean temperature profiles across the channel in thermal viscous units; for both cold and hot walls..... 120

Figure 24. Second order statistical analysis: (a) velocity turbulent intensity profiles and (b) temperature intensity profiles; for both cold and hot walls..... 121

Figure 25. Second order statistical analysis: (a) wall-normal velocity turbulent intensity profiles and (b) spanwise velocity turbulent intensity profiles; for both cold and hot walls. 122

Figure 26. Instantaneous three dimensional iso-contours of (a) streamwise velocity and , (b) normalized temperature in the channel. 123

Figure 27. Streamwise development of skin friction coefficient for baseline periodic case, compared to Batten inflow case with no forcing and, Batten inflow with controlled forcing planes. 126

Figure 28. Streamwise development of the integrated errors in (a) resolved turbulent kinetic energy and (b) the Reynolds shear stress conducted for baseline periodic case,

Batten inflow case with no forcing ng, and Batten inflow with controlled forcing planes.	127
Figure 29. Streamwise development of (a) mean velocity profiles, (b) turbulent intensity profiles, and (c) Reynolds shear stress profiles across the channel at three different stations at $x/\delta = 10, 15, 20$ with no controlled forcing	128
Figure 30. Streamwise development of (a) mean velocity profiles, (b) turbulent intensity profiles, and (c) Reynolds shear stress profiles across the channel at three different stations at $x/\delta = 10, 15, 20$ with activated controlled forcing planes	129
Figure 31. Schematic of turbulent boundary layer configuration showing synthetic turbulent inflow generation and its recovery length preceding a fully turbulent region.	132
Figure 32. Spatial development of mean skin-friction coefficient to evaluate the recovery length; simulation performed for a reference case with no transpiration.	134
Figure 33. Instantaneous visualization of turbulent structures via (a) iso-contours of velocity and (b) iso-contour of Q colored by streamwise velocity.	135
Figure 34. Transpired turbulent boundary layer (a) schematic , (b) Spatial development of mean skin-friction coefficient to evaluate the recovery length; compared to a full-scale configuration where blowing is specified through the wall beginning at $x=200$; comparison to an integral relationship.	137
Figure 35. First and second order statistical analysis: Effect of mass-transfer -- gas-injection -- in (a) normalized mean velocity profiles and (b) u-turbulence intensity profiles ; normalization in viscous wall-units.	139
Figure 36. Second order statistical analysis: Effect of mass-transfer -- gas-injection -- in (a) wall-normal turbulence intensity profiles and (b) spanwise turbulence intensity profiles ; normalization in viscous wall-units.	140
Figure 37. (a) Calibration of the mixture fraction combustion model with Burke-Schumann solution with constant specific heat (PMMA), (b) mapping of species mass fraction with mixture fraction and chemical state relationships.	145
Figure 38. 2nd order statistical analysis: (a) Spatial variation of turbulence intensity profiles featuring weak-to-moderate intensity levels; solid line represents experimental data of Zhou et al. (b) turbulent kinetic energy variations plotted in log-log coordinates showing a power law rate of decay coefficient ($n=1.2$)	149
Figure 39. Large-eddy simulation of turbulent non-premixed wall-flame subject to isotropic turbulence perturbations at $I = 5\%$ intensity level. Flame location is identified as an iso-surface of stoichiometric mixture fraction, $z_f = 0.108$ for polymethyl methacrylate fuel. The pyrolysis products originate from a small burning region at the wall with length $x_p = 4\text{ cm}$ beginning at $x = 10\text{ cm}$	151
Figure 40. Averaged contours of: (a) mixture fraction and (b) temperature for turbulent intensity $I = 5\%$; note that the flame length is identified by a solid black line (stoichiometric mixture fraction value) $x_f = 10\text{ cm}$	152

Figure 41. Averaged contours of: (a) mixture fraction and (b) temperature for turbulent intensity $I = 15\%$; note that the flame length is identified by a solid black line (stoichiometric mixture fraction value) $x_f = 4 \text{ cm}$ 153

Figure 42. Averaged contours of (a) mixture fraction and (b) temperature for $I = 15\%$; note that flame length is identified through a solid black line $x_f = 4 \text{ cm}$ 153

Figure 43. Average profiles of surface heat flux in the flame region: (a) spatial and averaged value of heat flux for $I = 5\%$, (b) spatial and averaged value of heat flux for $I = 15\%$ 154

Chapter 1: Introduction

Fire modeling presents several technical challenges to the practitioner due to complexity of the underlying physical and chemical processes involved. The uncontrolled growth of fire occurring as a result of fire spread phenomena is a major field of research in combustion science because of its direct impact to compartment settings such as residences or buildings. The application of the concepts involved in the mathematical representation of fire phenomena is not simple because it embraces nearly all the effects found in subsonic chemically reacting flows. The physical processes can include fluid dynamics, heat and mass transfer, combustion (gas and solid phase), finite-rate kinetics, thermal radiation and multi-phase flow effects. This is compounded by a plethora of possible fire scenarios to consider in which the exact composition of the fuel is often unknown. This reality often leads to an inadequate description of the thermal degradation of the condensed phase materials that supply the fuel and adds to the uniqueness and complexity of the problem. Clearly while fire modeling poses major technical challenges, it also offers enormous opportunities to the global research community as it identifies key areas where enhanced fundamental understanding of the physics is needed.

1.1 Motivation for Computational Research in Fire Modeling

The enormous speedup in computing power and networks has enabled simulations of far more complex systems and additional phenomena. As in various other areas of scientific research, fire modelers have begun making significant strides in the field through the use of high-performance computing, digital data, and fast networks to replace and extend traditional efforts. In 2003, a US National Science Foundation Blue Ribbon Committee began an initiative towards a *cyber-infrastructure* for computational research

in science and engineering. Cyber-infrastructure has been defined as the “infrastructure based upon distributed computer, information and communication technology” [1]. This national effort provides the platform for a new research environment linking together several research teams (cyber-based communities), digital data and information libraries (open source data and software), high-performance computational environments (super-computing centers), research instruments and arrays of sensors (smart panels). Largely as a result of the aforementioned initiatives, Computational Fluid Dynamics based fire models have been widely developed as a new approach for fire safety and engineering. The leader in CFD-based fire model development efforts over the past decade has been the National Institute of Standards and Technology, USA through the distribution of the open-source software Fire Dynamic Simulator (FDS) [2]; due to its open-source availability emphasizing end-user features, and wide-domain of fire-scenario applications it has been successfully established in the fire engineering, post-fire forensic investigation and litigation communities. More recently, competing open-source CFD based fire models have appeared (i.e., FireFOAM based on OpenFoam software) providing state of the art high-end features such as: advanced physical models for turbulent combustion and heat transfer, advanced meshing capabilities and massive parallelization [3]. In collaboration with industry leader Factory Mutual Research Corporation, USA it continues strengthening its modeling capabilities through active physics-based research projects. Thus, with the advent of computer power, the growing number of cyber-communities in fire, and the maturing of CFD-based fire models, it is clear that the classical approach to scientific research, theoretical/analytical and

experimental/observational, has been extended to include *computational research* as a new scientific approach in fire modeling.

1.2 Physical Description of Fire Phenomena

The complexity of fire phenomena can be described in detail by observation of the physical process present near the environment where it develops. One categorization of fires is based upon whether or not it is spatially confined. Enclosure fires are typically restricted in the amount of oxygen available to them and are subject to a slow process of smoke accumulation; they occur in several locations such as houses, apartments, vehicles, tunnels, mines, etc. In contrast, fires occurring in unconfined environments are potentially more damaging since they are not limited by enclosures, may cover a wider area, and depend strongly on the terrain and the environmental conditions where they occur. Several conflagrations have been reported in the past from industrial accidents at oil refineries, fires in urban areas, to major forest fires. The scales between enclosure and unconfined fires are also drastically different; in enclosure fires the length scales are on the order of centimeters to meters while in outdoor fires they can range up to several kilometers.

Enclosure fires typically begin by an unwanted ignition of a flammable object inside a confined space; thermal feedback drives the pyrolysis process releasing gaseous volatiles which burn as they mix with air. Convective and radiative heat transfer to the surroundings play an important role in the growth of the fire by raising the virgin fuel solid temperature to ignition. A fire plume develops entraining the surrounding air and raising the smoke/toxic gases and impinging on the enclosure ceiling. Ceiling jets form laterally from the plume impingement region and begin the smoke accumulation process

forming a smoke layer that fills from the top down. The interphase of the smoke layer separates the enclosure into two layers, a hot upper layer and a fresh cooler layer below where bulk properties are nearly homogenous. As the depth of the smoke layer grows, it significantly contributes to the ambient heating process (smoke layer temperature are typically at 800K-900K) increasing the radiative thermal load of potential virgin flammable objects leading to a phenomena called flash-over. This is also referred to as a fully developed fire since the majority of the exposed flammable surfaces have been heated to their pyrolysis temperatures and a series of auto-ignition processes have occurred leading to rapid fire-growth/fire-spread. Because of the increased fire size resulting from flash-over, and depending on the amount of oxygen available to the enclosure (i.e. vents, doors), the fire transitions to under-ventilated combustion or fuel-rich conditions. Under-ventilated fires are characterized by intermittent combustion as a result of insufficient amount of oxygen available to completely react with the fuel (post flash-over) leading to several events of flame-extinction phenomena. The flame location switches from the anchored fuel source to nearby vent locations using the gaseous volatiles available in the fuel rich environment and the oxygen stream from the vents to sustain its burning. Incomplete combustion leads to a surge in toxic product emissions such as carbon monoxide, unburned hydrocarbons and soot particles.

A typical enclosure fire scenario is depicted in Figure 1 showing the physical processes involved characterizing its behavior.

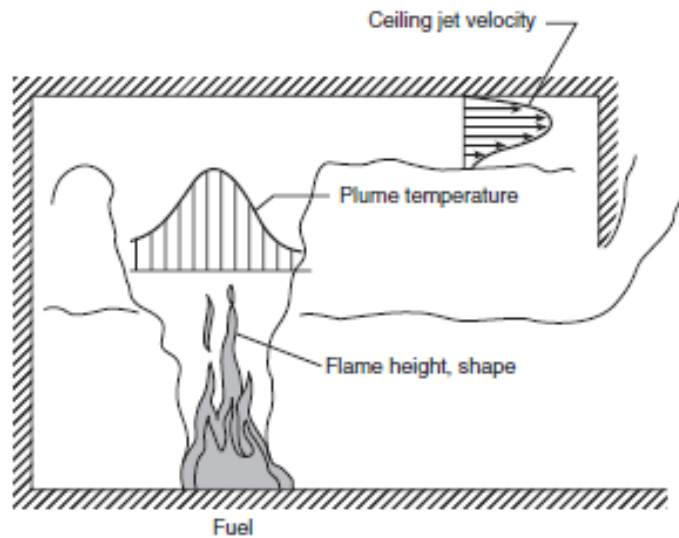


Figure 1. Physical processes occurring in an over-ventilated enclosure fire in its development stage (pre-flashover). Notice the development of a fire-plume and lateral ceiling jet providing the mechanism for smoke filling; also observe a natural stratification of hot upper layer (smoke gases) and a cooler lower layer (fresh-air) leading to a description of a zone-model approach. (Figure credit to SFPE handbook, Chapter 9)

1.3 Emergence of CFD based fire modeling

A review of the relevant literature clearly indicates that fire models can be classified as belonging to three main classes based on the level of accuracy, computing resources at hand, and level of technical expertise of the modeler. The categories are (a) algebraic models, (b) zone models and (c) computational fluid dynamics or CFD-based fire models. Algebraic models are developed principally on experimental correlations and are utilized to estimate the effects of important fire phenomena for simplified configurations. Although these models are basic, they are based on physical correlations obtained from governing parameters and scaling analysis and often provide a reliable prediction of the fire phenomena. The US Nuclear Regulatory Commission developed an algebraic fire

model library called Fire Dynamics Tools (FDT) used for quantitative fire hazard analysis for several postulated nuclear power plant scenarios [4]. FDT is a set of algebraic fire dynamic equations including a number of correlations for estimating fire characteristics such as the average hot gas layer temperature, smoke layer height, flame height under varying conditions. One of the objectives of this fire modeling tool is to provide information on the ability of specific fire models to predict the consequences of fire scenarios relevant to nuclear power plants. Although these tools are basic it has provided a methodology for fire protection inspectors to use in assessing potential fire hazards with credible fire scenarios. However, there are various modeling assumptions making them limited for several conditions such as: steady flow, averaged quantities, prescribed heat release rate and geometrical simplicity (often found in conventional sized residential compartments) [4].

Zone models describe a fire in an enclosure by discretizing the domain into a limited number of zones or control volumes. They have emerged very early in fire research (1970s) and have been used mainly to study the impact of fire on building compartments with considerable success [5] [6] [7]. The most common fire model in this category makes use of a two zone model where the discretization accounts for an upper layer near the ceiling containing hot combustion gases, and a cooler lower layer containing fresh air. Mass and energy balances are used to obtain simplified conservation statements combined with Bernoulli equations and engineering correlations to provide the conditions produced by the fire at a given time in a specified zone. This model assumes that the predicted conditions within each zone are homogenous at any time. Real-scale fire experiments have demonstrated that developing fires (pre-flash over) stratify in two

layers; although variations within each layer exist they are small compared to the differences between the layers. In spite of its recent success in practical engineering scenarios, zone models suffer from significant limitations inherent to their formulation[6]. One of the major drawbacks arises in the case of rapidly growing fires where there may not be enough time for the flow to restructure into layers; the validity of the model is also questionable for complex geometries such as a compartment obstructed by a variety of flammable objects. In these cases, CFD-based fire models will be more accurate since a more detailed description of the smoke transport can be captured.

CFD-based fire models have emerged due to the rapid growth of computer power, advancements in numerical techniques, and the need for a more detailed description of the smoke, heat transfer, and mass transfer process resulting from combustion. This is the current research topic of interest presented in this dissertation. A CFD model uses discretization techniques to represent the full governing equations of mass, momentum, and energy and integrates them in time numerically with the use of high-speed computing for a specified configuration (empirical models may be incorporated for consideration of complex physics); subject to boundary and initial conditions at a resolution that is determined by the characteristic length and time scales of the problem. The accuracy depends on the number of cells that is incorporated into the simulation, which is limited by the scales of the phenomena but also by the computer power available. In real life fire scenarios there are several length scales related to the geometry of the enclosure on the order of 1 m , the size of the turbulent eddies transported 1 cm and the reaction zone or flame thickness on the order of 1 mm . In addition, the intermittent nature of the turbulent and combustion phenomena involved in the fire requires adequate resolution of the time-

scales which are on the order of milliseconds. A simulation fully resolving the spatial scales for representative fire duration of 10 minutes (assuming a conservative time step of $dt = 1 \times 10^{-2}$) would have to solve the partial differential equations discretized in one-billion computational grid-cells for one-thousand time steps, resulting in a prohibitive cost. This demanding resolution requirement motivates the need for turbulent combustion modeling by which spatial and temporal scales and further physical restrictions may be relaxed.

1.4 Fire Modeling Constituents

A complete description of fire phenomenon demands several sub-models to account for the large number of physical processes involved. The models are derived from the conservation equations particular to each phenomenon and at times simplifications and empirical parameters are used in the formulation. A complete CFD-based fire modeling tool should provide a detail model description for several important processes present in fire scenarios. An excellent review of the major modeling processes present in fires can be found in the literature where details of each models are presented and discussed in terms of compartment fire modeling [7]. The modeling constituents are:

- Turbulence Modeling
- Combustion Model (Gas-Phase combustion)
- Thermal Radiation and Soot Transport Model
- Pyrolysis Model (Solid-Phase combustion)
- Fire Suppression Modeling
- Flame Extinction Modeling

Turbulence models are differentiated based on the amount of the flow resolution needed which typically depends on the accuracy desired and computing resources available. The consensus today, from industry and academia, is that Large-eddy simulation technique is the method of choice for fire modeling practitioners [8], [9]. In LES, the large geometric dependent flow-structures are solved directly while the smaller high-frequency eddies (the most computationally expensive) are accounted through a dissipative “subgrid-scale” model. A more comprehensive literative review of turbulence modeling in wall-bounded flows is presented in Section 1.5 of this Chapter.

Numerous gas-phase combustion models are based on a conserved-scalar approach suitable for “equilibrium” fast chemistry systems. The conserved scalar approach allows major simplifications since the chemical composition of the flow can be re-constructed by transport of a single scalar (mixture fraction) through classical chemical state relationships. This assumption is justified in many practical cases, since many reactions have high rates and can be considered complete as soon as the reactants are mixed. The problem of chemistry-turbulence interaction is drastically simplified in this case since the statistics of all chemical variables can be obtained from the statistical information of the conserved variable. This may be achieved through the use of Favre Probability Density functions (presumed PDF approach) for the conserved scalar and integration over the mixture fraction space. Several extensions of the conserver-scalar approach for the treatment of combustion modeling that have also received much attention in the community are: Eddy Break-up Model and Flamelet models; they are presented in detail in several review papers [7], [8], [10].

The dominant role of radiation in fires makes the numerical simulation more computationally expensive. Thermal radiation is proportional to the black body Plank function and the emissivity of the participating medium, increasing with radiating path length and absorption coefficient of the medium. The exchange of radiation heat transfer is independent of any medium; it has strong direction and wave number dependence in most practical situations, such as a developing fire where the radiated gas is highly non-gray and non-homogenous. This implies that an exact solution of radiation heat transfer in practical fire scenarios is not available and demonstrates that the modeling of such can be expensive. There exist several practical models to solve the radiation transfer equations, one that has been successfully applied to several fire modeling problems is the Discrete Transfer Method (DOT). This technique traces rays of radiation through the computational domain, and a simplified equation for the radiation intensity is solved along each ray. The number of and direction of rays from each points are chosen a priori to provide a desired level of accuracy; the net gain or loss of radiant energy in each control volume is calculated based on the number of rays crossing it [11]. Several extensions exist that remove the gray assumption by dividing the spectrum into bands, applying recurrence relationship for each band and summing it up [7].

When solid fuel is present such as in compartment fires, consideration also has to be given to the response of the solid fuel and the interaction between gas and solid phases. The solid fuel may undergo a series of complex physical and chemical processes largely driven by the local conditions. The interaction includes the mass, energy and momentum exchanges between the two phases. The treatment of pyrolysis process in CFD-based fire modeling is still not very mature and remains semi-empirical; the difficulty lies in the

lack of knowledge of the thermal degradation process itself. Numerous studies have been conducted that describe the fuel degradation by kinetic models of different complexity, varying from a simple one-step global reaction, to multi-step reaction mechanisms [12], [13], [14].

Suppression by water sprinklers is one of the most common widespread fire control system and is presently an area of strong research interest due to its impact on fire safety in compartment settings [15] [7], [16]. Water sprays are commonly used in fire suppression applications for cooling the fire environment. This cooling is achieved through the evaporation of droplets (dispersed in the fire gases) and through the wetting of surfaces (from hot or burning materials), inhibiting both the growth and spread of the fire. The water spray is typically modelled as a Eulerian-Lagrangian system, where the gas phase is solved using Eulerian techniques and the liquid phase is tracked as multiple Lagrangian particles with mass, momentum, and temperature. It is the most popular method used in spray simulations because of its simple implementation and computational efficiency. Several experimental studies have been carried out to fully characterize sprinkler sprays at the exit from the nozzle including measurements for: water discharge rates, droplet size and droplet velocity distributions. To further characterize spray effectiveness, an Actual Delivery Density (ADD) parameter is defined as the density of the water flux, it measures the ability to penetrate the fire region; this is one of the quantities that can be directly compared with CFD predictions [7]. More recent work on water-based suppression systems have focused on characterizing the initial spray properties of water-sprays. A comprehensive atomization model capturing the initial physical features (pre-atomization) and atomization characteristics has been presented in

several research studies providing a more accurate model description to be used in CFD-based modeling tools [16][15].

Due to the presence of fire-suppression systems, as well as the physical mechanisms inherent to fire (fuel burn-out, oxygen depletion, flame cooling), total flame extinction models are also important for realistic CFD-based fire models. Earlier extinction models, defined extinction conditions based on a critical adiabatic flame temperature $T_c \sim 1700K$ and a lower-oxygen index limit, $Y_{O_2} = 0.17$ required for sustained burning. This analysis resulted in a two parameter flammability map with a clear discrimination between a flammable and non-flammable domain used to determine the conditions under which the local ambient oxygen concentration will no longer support a diffusion flame [2]. This model assumes that extinction is dominated by air-vitiation effects while leaving out important extinction mechanisms such as flame-stretch, fuel vitiation and simplifying the effects of heat losses. In more recent studies, the effect of flame stretch, heat losses, fuel and air vitiation on the extinction limits of ethylene air diffusion flames were presented using large activation energy asymptotic (AEA) theory [8][17]; providing a six dimensional parameter predictive model for extinction. The AEA analysis features a phenomenological soot model that accounts for particles inception, growth and oxidation, and a generalized treatment of thermal radiation that accounts for both emission and absorption phenomena and applies to participating media ranging from optically-thin to optically-thick. The AEA analysis leads to a critical Damkohler number based extinction criterion providing more descriptive flammability maps. Numerical comparison with the AEA model demonstrates that the FDS model overestimates the size of the flammability domain leading to a less accurate description of the extinction event [17].

To meet the needs of fire engineering applications, models are developed and implemented to represent the physics approximately and speed up the numerical computations to an acceptable level, with proper compromise between accuracy and CPU cost.

In this work, models for high-fidelity turbulent transport, chemically reacting flows, and the development of numerical methods for fire modeling are presented with an emphasis to correctly capturing the near-wall physics present in turbulent boundary layer flows. The developments have been incorporated into a CFD solver called LES-BLAC (Boundary Layer Combustion); extensive verification and validation studies have been devised and executed. Several numerical simulations have been carried out relating *to wall-bounded turbulent flows* with multi-physics components such as heat transfer and mass transfer . Lastly, the heat transfer aspects of wall-flames is presented (Chapter 5) in a validation study showing good agreement with reference measurements.

1.5 Introduction/Literature Review on Turbulent Flow Modeling

Often conducting wind tunnel experiments to study turbulent flows can be expensive and numerical simulations may provide an attractive low cost option. The solution of turbulent flows is possible through computational simulations that vary by their level of resolution and accuracy. The most reliable computational strategy is Direct Numerical Simulation (DNS) in which all length-scales are fully resolved; due to its unparalleled accuracy and high computational cost it is only feasible for low Reynolds number flows. At the other end of the spectrum, Reynolds Averaged Navier Stokes Equation (RANS) resolve only the mean motion and rely on modeling the entire Reynolds stress tensor, it has been most widely used in the engineering community for simulating practical high

Reynolds number or complex flows. However, RANS will typically fail to capture large scale instabilities that are fundamental to turbulent flow transport. Large Eddy Simulations (LES) represent a compromise between DNS and RANS since it does not intend to numerically resolve all turbulent length scales, but only a fraction of the larger energy-containing scales within the inertial sub range. Modeling is then applied to represent the smaller unresolved (SGS) scales, which contain only a small fraction of the turbulent kinetic energy.

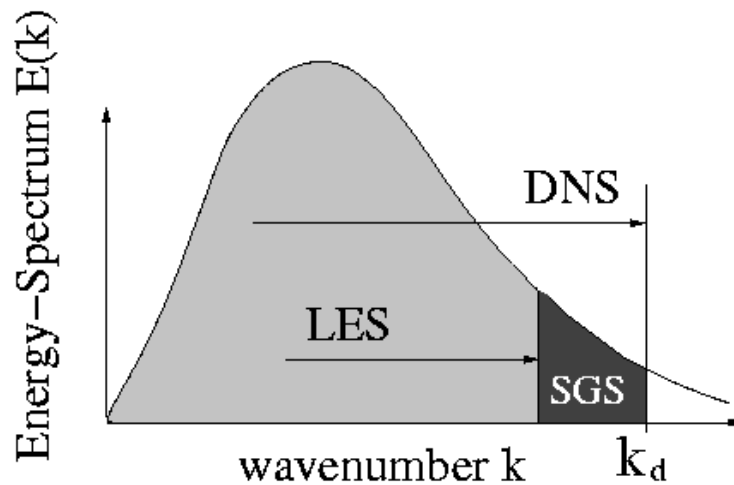


Figure 2. Turbulent flow energy spectrum $E(K)$ variations with wavenumber, k . The modeling differences between Direct Numerical Simulations (DNS) and Large-eddy simulations (LES) are presented in terms of resolved scales (wavenumbers). Subgrid scale LES model is highlighted demonstrating the need to model the small diffusive spatial scales.

The solution of turbulent flow problems is theoretically possible through the direct numerical simulation (DNS) of the Navier-Stokes equations (with appropriate boundary conditions). This method constitutes the conceptually simplest approach to the

problem of turbulence. Practically, however, the cost of DNS confines this approach to simple applications in terms of Reynolds number and geometry complexities. In fact, in DNS all scales of motion must be resolved, from the integral to the Kolmogorov scales. The computational domain must be on the order of the largest scale. This results in a number of grid points in each direction that is proportional to the ratio between the largest and the smallest scale, L/η . Defining a Reynolds number based on the integral scale L, Re_L , the number of grid points (in each direction) will be proportional to $Re_L^{3/4}$, so a total number of points proportional to $Re_L^{9/4}$ is required by DNS. Moreover, the time step of the calculation Δt is typically limited by a CFL condition, that is $\Delta t < \frac{\Delta x}{U}$ where U is the local velocity determined by the integral time and length scale, we have that the total number of steps in time is $T/\Delta t$ again proportional to L/η (where the CFL condition measures how much information traverses a computational grid cell in the given time step). Thus the total cost of a DNS calculation will be on the order of Re_L^3 . This means that for high Re numbers, DNS corresponds to a prohibitive computational cost: assuming that computer power will increase by a factor of 5 every five years, Spalart [18] estimates that DNS will not be applicable for the study of the flow over an airliner or a car until 2080. In this context, a Large-eddy simulation (LES) presents a feasible alternative to DNS calculations since modeling is limited to the smallest scales of the flow. The large eddies containing the bulk of the energy, typically anisotropic and dependent on boundary conditions, are simulated directly. The fact that the small, dissipative eddies are modeled helps reduce the cost of LES considerably compared to DNS.

1.5.1 Boundary Layer Flows

Wall bounded flows are constrained by the presence of a solid wall which will enforce the no-slip condition (the velocity of the fluid at the surface must be equal to the velocity of the surface). They present a challenge since velocity and temperature gradients must be resolved and computed accurately to provide useful quantities such as wall shear stress, skin friction and heat fluxes. They may be categorized into homogenous or non-homogeneous according to certain characteristic presented along the direction of the mainstream. This feature is related to the behavior of the flow parameters after some distance or period due to a restriction imposed to the flow. Typical examples are given by flow in pipes and channels after the development section, where boundary layers merge leading to a fully developed flow. From this point, the flow becomes homogeneous in the streamwise and spanwise and periodic conditions can be assumed. On the contrary, a spatially evolving boundary layer is a case of non-homogeneous flow due to the unrestricted growth downstream. The non-homogeneity showed along the flow direction makes them much more challenging to compute numerically than homogeneous flows because of the need to prescribe turbulent inflow information at the inlet of the domain at each time step.

The presence of turbulent eddies in wall-bounded flows presents an additional challenge since they are characterized by much less universal properties than free shear flows and are thus more challenging to compute. A two layer model is normally assumed where the near wall region where viscosity (and diffusion) dominates is referred to as the viscous sublayer and the outer adjacent region is called the outer (log) layer. Within the viscous sublayer, the characteristic velocity and length scales are set by the friction

velocity and the viscosity providing wall viscous-units (See Chapter 4). As the Reynolds number increases and the thickness of the viscous sublayer decreases, the number of grid points required to resolve the near-wall structures increases. Thus, when LES is applied to wall-bounded flows at moderate to high Reynolds number it is still very demanding because of the inner layer resolution requirements. In fact, as found in Chapman [19], considering a flat plate boundary layer, the outer part has energy-carrying structures on the order of the boundary layer thickness, δ . Assuming that the grid spacing is fixed in the streamwise and spanwise direction and on the order of 0.1δ , Chapman estimates a total number of grid points proportional to $Re_L^{0.4}$. In the inner part of the boundary layer, on the other hand, the number of points must be based on the inner layer scales; in fact, the dimension of quasi-streamwise vortices are constant in wall units (i.e., normalized by kinematic viscosity, wall stress and fluid density). Thus, the total cost of the calculation in the inner layer is estimated to be proportional to $Re_L^{1.8}$ which makes wall-resolved LES only suitable for moderate Reynolds number applications.

Alternatives to wall-resolved methods are wall-layer models for large-eddy simulations in which three classes of models exist: equilibrium stress models, zonal models, and hybrid LES/RANS methods. Equilibrium laws typically make use of wall-function relationships that provide the mean velocity (or temperature) in the near-wall region as a function of distance from the wall. The idea is to bypass the inner layer by using approximate boundary conditions. These boundary conditions assume the existence of an equilibrium layer in which the stress is constant resulting in the existence of a logarithmic layer that is typically used to relate the velocity in the outer layer to the wall stress. However, this technique is likely to fail for engineering flows having strong

pressure gradients, separated flows or flows where the mean velocity is three dimensional (since these conditions eliminate the equilibrium stress layer approximation). These observations fueled the development of hybrid models in which simpler transport equations are solved in the inner layer and coupled to the outer flow LES. This idea was proposed by Balaras et al [20], Two-layer model (TLM), with a weak coupling between the inner and outer layers. A fine one-dimensional grid is embedded between the first grid point and the wall, and a simplified set of equations (generally, the Reynolds-averaged turbulent boundary-layer equations) is solved in the embedded mesh. The outer-layer LES provide the boundary condition for the inner layer, whereas the inner-layer calculation provides the wall stress required by the LES [20]. Hybrid simulations in which the RANS equations are used in the inner layer, while the filtered Navier–Stokes equations (LES) are solved in the outer layer are also of practical interest. Several strategies can be used to switch between one model and the other, such as changing the length scale in the model from a RANS mixing length to one related to the grid size, or using a blending function to merge the SGS and RANS eddy viscosities. In terms of computational cost equilibrium models are the least expensive. According to Piomelli et al [21], the cost of this simulation scales like the outer layer, $Re_L^{0.6}$. Zonal models require between 10% and 20% more CPU time for the solution of the boundary layer equations (in the inner layer), and an additional memory overhead. The cost of hybrid RANS/LES methods is higher due to the restriction of resolving the wall normal direction ($y^+ \sim 1$) and the number of grid points in the wall-normal direction is proportional to $\log(Re_L)$ making the cost scale like $Re_L^{0.6} \log(Re_L)$.

It is observed from the literature that numerical simulations, both DNS and LES, about fully developed turbulent channel are numerous. On the contrary, numerical predictions of spatially evolving turbulent boundary layers are rather scarce because of the numerical challenge to prescribe time-dependent fluctuations at the domain inlet. Therefore, simulating a streamwise evolving flow implies the selection and application of a procedure able to generate realistic turbulent inflow data with a relatively high computational cost. Several techniques for turbulent inflow generation have been employed with different degrees of success and a comprehensive review of these methods can be found in Lund et al [22] and Moin and Mahesh [23], and more recently in Keating et al [24]. The first DNS of a spatially developing boundary layer was carried out by Spalart [25]. Spalart used a coordinate transformation to treat the streamwise inhomogeneity of evolving boundary layers as a homogeneous flow, and, consequently, agreeable to periodic conditions. The pioneering Spalart's approach is very ingenious but is limited to flows whose mean streamwise velocity variation is small as compared to the vertical variation, such as zero-pressure gradient (ZPG) flows. Consequently, in numerical simulations of more complex flows, both inflow and outflow boundary conditions must be established introducing an additional model for the treatment of flow leaving the domain. Originally, inflow conditions were generated by specifying a mean velocity profile and superimposing some random fluctuations, so called synthetic turbulence. Le and Moin [26] produced inflow conditions for DNS of a backward-facing step basically from a three dimensional, divergence free field of random fluctuations with prescribed moments and spectra. Random fluctuations were created by the proposed method of Lee et al [27]. Thus, this turbulent field was convected through the inflow

plane by using the Taylor's hypothesis. However, the inlet turbulent structures required a long distance for accommodation and reaching a realistic state because the inflow information was void of the phase information of the real turbulent eddies. It was reported by Le and Moin [26] that 50 displacement thicknesses from the inlet channel were required to get a realistic turbulent flow, which seriously penalized the streamwise length of the computational box and, thus, increased the cost of the simulation. An improvement of the previous approach was proposed and tested by Na and Moin [28], and Akselvoll and Moin [29] by convecting an instantaneous turbulent field computed from an auxiliary temporal simulation. This modification was observed to shorten significantly the evolution distances but at a high computational cost of having an extra numerical simulation.

More recently, Batten et al [30] introduced a new method to generate synthetic turbulence that takes into account the anisotropy of the flow. The method by Batten et al is based on the superposition of sinusoidal modes with random frequencies and wave-numbers, with given moments and spectra. Their approach includes an ingenious way to modify the wave numbers to yield eddies that are more elongated in the direction of larger Reynolds stresses, thus introducing more realistic anisotropic eddies into the flow. Later on, Spille-Kohoff [31] proposed a method that seeks to establish the correct Reynolds stress profiles earlier in the domain. They used a synthetic turbulent field at the inflow and a number of control planes downstream. At these planes, a controller amplifies the wall-normal velocity fluctuations to try to match the required Reynolds shear stress. These last two methods are further analyzed in the turbulence validation section of Chapter 4. Finally, the simulations of even more complex evolving flows, of

great value in engineering applications, require the use of appropriate methodologies for inflow conditions which is part of the focus of the present study.

1.5.2 Transport of scalars in wall-bounded flows

The transport of scalars is important in various engineering applications ranging from combustors, boilers to thermal boundary layers as found in turbine blade film cooling. In many cases, there is a two way coupling between the scalars and the flow: the transported field can influence the velocity field – which is known as active scalar transport. This is the case, for example, of the temperature field that acts on velocity through density changes. Conversely, situations where the feedback of the scalar field is negligible and the velocity determines the properties of the scalar, but not vice versa, are termed passive. This ideal case is well approximated by the use of dye in laboratory experiments or by the transport of smoke and low concentration pollutants. Although active and passive scalars are governed by the same advection-diffusion equation, their nature is radically different. Passive scalars belong to the category of linear problems, despite being highly nontrivial. Celani et al [32] reports that as a consequence of the statistical independence of the forcing and the advecting velocity, the transported fields depend linearly on the forcing. This property allows a theoretical treatment of the problem, and has the major consequence that the passive scalar scaling laws are universal with respect to the injection mechanism. On the contrary, for active fields, the presence of the feedback couples the velocity with the transported scalar and makes the problem fully nonlinear. In this case, the theoretical tools developed for studying the passive problem may fall short of explaining the behavior of active scalars, and the current understanding of active turbulent transport lags far behind the knowledge accumulated on the passive counterpart.

One of the first numerical simulations with respect to the transport of passive scalar fields was performed by Kim and Moin [33] at a Reynolds number of 180 (based on wall friction velocity and channel-half width) and at various molecular Prandtl numbers. They considered two different types of boundary conditions. In the first case, the heat is generated internally and removed from isothermal walls at the same temperature. In the second case, isothermal walls at different temperatures create a temperature gradient and drive the heat transfer. More recent work of DNS of turbulent heat transfer in channels have been performed and a comprehensive review of progress on the topic can be found in Kasagi and Iida [34], Kasagi et al [35] and Keating [24].

The case of streamwise homogeneous flows with strong heat transfer and variable property has been studied extensively by various researchers. Two regimes of interest often found in the literature with this configuration are: subsonic, low Mach number flow and compressible high Mach number flow; where the role of pressure becomes vital in understanding the difference between the two methods. Fully compressible numerical formulations are constrained by the need to resolve fast acoustic wave motions; hence the density is dependent on both temperature and pressure increasing the complexity of the system. In the low Mach number limit where density becomes independent of pressure, the role of pressure is to act on velocity through continuity so that conservation of mass is satisfied. For low speed flows, the pressure gradient needed to drive the velocities through momentum conservation is of such magnitude that the density is not affected significantly and the flow can be considered nearly incompressible. Hence, density and pressure are very weakly related. Thus for slow flows, the low Mach number formulation,

where the acoustic properties are filtered out, becomes a computationally cost effective method to use.

One of the first variable property channel flow numerical study was carried out by Wang and Pletcher[36]. They performed a LES study of low Mach number isothermal channel flows with one hot wall and one cold wall, with temperature ratios as high as 3. The heat transferred by the hot wall was removed from the channel through the cold wall so there was no bulk temperature rise. Results showed that velocity fluctuations are minimum at the center because there was no mean velocity gradient at that location. However, the temperature fluctuations remained large near the center of the channel. Since there is energy transfer from the heated to the cooled wall, the whole domain contains temperature gradients including the center of the channel. The compressible formulation of the dynamic SGS model was utilized in a staggered grid finite volume method that was fully implicit. Later on, Nicoud and Poinso [37] applied DNS to a very similar configuration and pointed out that some of the observed effects might be explained through the different local values of Reynolds number obtained near the hot and cold walls. A higher Reynolds number was observed near the cold wall and a lower one was found near the hot wall. The variations in Reynolds number were thought to be responsible for a variation in the size of the turbulent structures. The structures near the hot wall were much larger than those near the cold wall. These different Reynolds numbers were likely due to different density and viscosity values which were functions of temperature. Another observation from this study was that the effect of lower density near the hot wall is to locally laminarize the flow, effectively yielding a frictional Reynolds number close to the transition state. Further studies consisted in re-defining the

Sutherland's law such that the physical properties near the hot-wall could remain in a fully turbulent state. This configuration will be explained in more detail in Chapter 4 of this dissertation.

1.6 Boundary Layer Combustion – Flame Spread

The main, long-term objective of this work is the detailed study of flame-spread over solid combustibles. A brief literature review is presented in this section to introduce the concept, mechanism and models of flame spread. Flame spread over fuels such as cellulosic paper, fiber, textiles, polymeric and wooden material is a fundamental problem in boundary layer combustion and of practical value in fire safety. One important flame spread mechanism is the heat transfer from the burning region to the unburned solid for heating up and vaporizing the fuel. The rate of heat transfer to the unburned material plays an important role in the flame spread mechanism and should be accounted for in models. In the study of flame spreading mechanisms, two distinctive modes have been considered in the past. In the mode of opposed-flow flame spread, flame spreads against the oxygen flow; while in concurrent flame spread, flame propagates in the same direction as the oxidizer flow. The concurrent flame spread is generally considered more rapid than the opposed flow mode except under certain conditions in a microgravity environment. Typically, upward flame spread over a vertically solid fuel is the case of concurrent flame spread since the buoyancy-induced flows are driven upward. The upward flame spread has been thought to be an accelerating process and more hazardous than downward spread [38]. However, considerations in most of these studies were given to a single flame spreading over a single solid. Most practical heterogeneous combustion processes involve interacting discrete burning elements. The flame spread rate is

determined largely by the forward heat transfer rate, which depends on the burning conditions, flame configurations and physical properties of the solid [38] (flame spreading behavior would be quite different when flame interacts with other flames).

Several studies starting with de Ris [38] and followed by Altenkirch et al.[39], Zhou et al. [40], Wichman et al. [41], [42], and Bhattacharjee et al.[43], [44] have focused on opposed flow flame spread. Other studies have focused on vertical flame spread (wind-aided or concurrent flow spread). Concurrent flow flame spread rates are inherently unsteady, accelerating as pyrolysis height increases. Markstein and de Ris [45] investigated upward fire spread over textiles. They found an accelerating flame spread rate and characterized it by a power-law relationship between pyrolysis spread rate V_p and pyrolysis height x_p : $V_p = \beta x_p^n$. Orloff et al. [46] examined the upward fire spread rate for vertical polymethyl methacrylate (PMMA). With 4.5 cm thick, 41 cm wide, and 157 cm high vertical PMMA slabs, they observed flame spread that remained relatively constant for pyrolysis heights from 10 to 15 cm and subsequently became proportional to x_p : $V_p = 0.0041x_p^{0.964}$. Fire behavior of PMMA was studied comprehensively by Tewarson and Ogden [47]. They also found flame spread rates accelerate for upward spread. The total heat fluxes to the solid flame region ranged from 20 to 30 kW/m² for 0.61 m PMMA samples, which agreed with the analysis by Quintiere et al. [48] Wu et al. [46] conducted a 5 m high PMMA vertical wall panel experiment. The heat release rate and pyrolysis height increased exponentially as a function of time. Total heat fluxes to the fuel surface varied from 30 to 40 kW/m².

1.7 Research Aims and Thesis Contribution

1.7.1 Research Aims

The main objective of this body of work is to provide the fire research community with a state-of-the-art CFD-based fire modeling tool, called LES-BLAC, to study the heat transfer properties of non-premixed wall flames in momentum driven turbulent boundary layer flows. The solver is an “in-house” Large-eddy simulation CFD research tool that is an extension of the solver developed by Dr. Keating and Dr. Piomelli; it was initially developed to study problems in chemically inert turbulent boundary layer and channel flows. LES-BLAC provides an advanced computational platform written in FORTRAN 90, including distributed memory parallelism using MPI libraries, allowing for flexible integration for application development. Numerous multi-physics developments were implemented to expand its previous capabilities to include the treatment of several configurations previously not available (for both periodic and spatially-developing flows). The configurations include a broad range of problems in periodic turbulent channel flows with an emphasis on heat-transfer with variable properties and its effect on turbulence statistics, boundary layer flows, and turbulent wall-flames in boundary layers. The overall research aims for LES-BLAC are: *(i)* to provide high-fidelity LES simulations of wall-flames over flammable solids, *(ii)* to study the coupling between gas-phase and solid-phase combustion process, and *(iii)* to devise and conduct simulations of canonical fire spread configurations. Further research aims for les3D-mp, not addressed in this manuscript, is the integration of an advanced solid-phase pyrolysis solver, called ThermaKin, to provide a more accurate description of the burning rates of polymers (i.e. PMMA) needed for a complete treatment of flame-spread.

1.7.2 Thesis Contribution

The current work is an extension of previous efforts by several researchers working with this CFD solver. The most notable contribution is by Dr. Keating and Piomelli for providing the initial solver and demonstrating its accuracy for several challenging flows; and Dr. Cruz for validating the code for subsonic wall-jet film cooling simulations. The current study builds upon this earlier work by introducing further multi-physics models to study the heat-transfer aspects of non-premixed turbulent diffusion flames near flammable/non-flammable walls. The CFD model developments as a result of this PhD thesis are enumerated below:

- Development of a Low Mach number Navier Stokes formulation (allowing variations in mass density due to temperature, but not pressure)
- Development of an implicit LES filtering formulation (including a dynamic Smagorinsky approach with a classical eddy viscosity/diffusivity model for subgrid scale transport. Coefficients are calculated dynamically and averaged over Lagrangian pathlines)
- Development of a 2nd order central differences spatial scheme (computed on a spatio-temporal staggered grid)
- Development of a 2nd order fully implicit time integration scheme (integrated with a high-accuracy iterative algorithm developed to provide coupling to the fractional step treatment)

- Development of an upwind numerical treatment for convective terms (QUICK scheme) for handling of scalar transport equations (used for numerical stability and correction of spurious temperature “spikes” observed for high-frequency temperature oscillations in turbulent channel flows.
- Development of a Mixture Fraction Combustion Model (including two scalar transport equations for mixture fraction and total enthalpy; featuring a Newton-Raphson technique utilized for temperature field calculation)
- Implementation of CHEMKIN databases for multiple species calculation of thermodynamic properties allowing for large temperature variations in specific-heat and enthalpy. A simplified model is adopted to include thermodynamic properties of PMMA for wall-flame calculations.
- Development and evaluation of several boundary conditions including: an advanced synthetic turbulence inflow generation technique with multiple-plane treatment enforcing a target Reynolds stress profile, an Orlandi type outflow boundary condition, and a mixed convective-diffusive boundary condition for porous wall.

The model developments enumerated above provide the back-bone of the current version of LES-BLAC and are here-after used in simulating turbulent combustion and heat transfer configurations of interest. Wall-flame configurations typically occur in

boundary layer mode and thus a correct numerical treatment of “wall-bounded” flows (i.e. channel-flows, boundary layers) is essential. To this end, numerous Large-eddy simulation studies of canonical turbulent channel flows featuring strong heat transfer and variable property physics were carried out showing excellent quantitative and qualitative comparisons with established results. A detailed analysis of the turbulent statistics, including first and second order moments of flow and thermal properties, were found to be in good agreement with fully-resolved turbulent calculations. Laminar simulations of basic engineering flows (where analytical solutions are available) were also conducted to assess the performance of the CFD model for internal and external spatially developed flows with strong variations in mass-density. Several boundary conditions corresponding to synthetic turbulent generation inflow, outflow boundary condition, and handling of the fuel injection process at the wall were also tested and validated. The reacting flow simulations presented as a result of this work emphasize “small-scale” momentum driven wall-flames (total length less than 0.3 meters) where the heat transfer process is convectively dominated (thermal radiation is currently neglected). Fuel injection is introduced through a wall-boundary condition that models the thermal degradation process of a common Plexiglas material polymethyl-methacrylate (PMMA). This flow is subject to an external cross-flow of oxidizer at various bulk velocities and features weak-to-moderate turbulence fluctuations. It is a unique configuration since it provides a framework to study the effect of flow properties and turbulence intensity on wall-flames.

Some of the combustion properties affected by the flow-characteristics are the flame length, wall heat-flux, and the flame structure. Further discussion of the wall-flame

configuration is provided in Chapter 5. In summary, the candidate's contributions are listed below:

- Introduced a high fidelity CFD-based fire modeling tool by adapting a well validated turbulent boundary layer code to include variable mass density and combustion capabilities. The solver extends the present state of the art in fire modeling (limited to laminar flows) by providing a high quality numerical tool to study the heat transfer aspects of turbulent wall flame phenomena.
- Devised and performed verification studies of diffusion dominated isothermal binary mixing case, laminar heated Poiseuille flow, and classical laminar boundary layers. Numerical studies have shown the correct order-of accuracy for spatial discretization and time integration schemes and good agreement with velocity profiles and wall shear stress for the Blasius case.
- Devised and performed several validation studies of canonical turbulent channel flows. Numerical studies include classical adiabatic turbulent channel flows; further studies have emphasized the effect of heat transfer and variable properties on turbulence statistics. Further studies of turbulent boundary layer with uniform transpiration (mass transfer) have shown good agreement with integral relationships for wall friction properties and turbulent scaling showing self-similarity.

- Devised and performed validation studies relevant to wall-flame configurations where the fuel is injected through a prescribed burning rate wall boundary condition. This study considers the effect of flow variables (mean velocity and turbulence intensity) on flame structure, flame length and surface heat flux. To the author's knowledge, this work provides the first LES computational study of horizontal flame spread in the open literature

1.8 Thesis Overview

This section provides a brief description of each chapter presented in this dissertation. It is intended to be a short abstract of each chapter highlighting the technical content, main results, and accomplishments obtained at each milestone. The overall spirit of this manuscript in subsequent order is: the motivation of CFD-based fire modeling as a research tool, the presentation of the models and numerical schemes used in LES-BLAC, the presentation of verification studies for wall-bounded variable density flows, the presentation of validation studies for turbulent flows with heat transfer and variable properties, and the presentation of a turbulent wall-fire validation study and comparisons with published experimental results. The abstracts of each chapter are listed below.

1.8.1 Chapter 2. Numerical Methods

A detailed description of the fundamental governing equations is provided with emphasis on the discretization and numerical techniques for the low Mach number transport equations. A second order fractional-step implicit scheme is presented as the time-integration technique (featuring a mass density based iterative loop); spatial discretization is handled through a second order finite difference scheme on a conservative spatio-temporal computational cell devised for the treatment of variable density flows. The turbulence modeling framework specific to “Large eddy simulations” is also presented with emphasis on Reynolds averaged and mass-weighted filtered variables for flows with strong variation in mass density. Combustion is treated using a classical infinitely fast chemistry description in which the composition and temperature of the reacting flow are described in terms of mixture fraction Z and total enthalpy h (enthalpy of formation plus sensible enthalpy)

1.8.2 Chapter 3. Verification using benchmark laminar flow problems

Numerical characterization of the spatial and temporal discretization schemes is presented for basic internal/external flows with analytical solutions. Of interest here is the canonical flow featuring a one-dimensional diffusion dominated binary fluid mixing configuration. The analytical solution to the problem is presented and several order-of-accuracy analyses are executed as a verification study to establish the solver's accuracy. Further verification studies in two dimensions are presented, as well as classical laminar boundary layer flows to demonstrate the capability of the solver.

1.8.3 Chapter 4. LES Validation of wall-bounded flows

The main aspects of turbulent channel flows are presented, including a discussion on Large-eddy simulation techniques vs. Direct Numerical Simulation. The viscous “wall” units are presented as the normalization parameters of choice for turbulent channel flows leading to a universal law of the wall model. Numerical results are presented for the classical turbulent channel configuration (without heat transfer) obtaining good agreement for mean velocity and turbulence intensity with DNS databases. A vortex identification method “Q-criterion” is presented to obtain a visual representation of the coherent flow structure. Further turbulent channel studies conducted are presented to demonstrate the influence of heat transfer on the turbulence statistics, namely the Reynolds stress tensor and temperature fluctuations. Comparisons are made with DNS databases in terms of first and second order statistics, friction velocities, wall-heat flux, and skin friction showing good agreement. A canonical turbulent boundary layer configuration with surface transpiration is analyzed in terms of turbulence characteristics

and the effect of mass transfer on the results. This is a relevant configuration since it represents the blowing process observed in the fire spread pyrolysis process.

1.8.4 Chapter 5. LES Application of turbulent wall-fires

A review of flame spread is presented with emphasis on momentum driven wall-flames such as ceiling/floor flames. The present study considers a simple non-premixed wall flame configuration in which the fuel corresponds to pyrolysis products supplied by a thermally-degrading flat sample of polymethyl methacrylate (PMMA) and the oxidizer corresponds to a cross-flow of ambient air with controlled mean velocity and turbulence properties. This configuration was previously studied experimentally at the University of California at Berkeley[49–51] ; the air cross-flow features moderate turbulence levels, i.e. a free stream velocity of 2 m/s and turbulence intensities between 5 and 15%. The numerical simulations use an advanced inflow forcing technique to simulate the air cross-flow as well as experimental data to prescribe the fuel mass flux at the wall; the wall surface temperatures are obtained by using a simple one-dimensional thermal conduction solver coupled with the gas-phase heat transfer. Comparisons between numerical results and experimental data are made in terms of flame structure, heat flux and flame length.

1.8.5 Chapter 6. Conclusions and Future Work

A comprehensive summary of the numerical work conducted in each chapter is presented with emphasis on the contributions proposed in this thesis. Future work in vertical turbulent wall fires and pyrolysis modeling is identified as having a prevalent role in CFD-based fire modeling.

Chapter 2: Numerical Methods

This chapter presents the fundamental equations and numerical methods necessary in modeling boundary layers with heat transfer and reacting flow in cartesian coordinates. This requires adequate discretization of the governing equations, a stable time advancement scheme, advanced turbulence modeling, and a suitable combustion model. The first part of the document presents the governing equations and derivation of the large-eddy simulation technique applied within a constant density framework. Of particular interest is the classical dynamic model proposed by Germano et al [52]. An extension to a low mach number, variable density numerical framework is introduced for the governing equations as well as for the turbulence model showing that no additional terms need to be introduced in the subgrid scale description, and the inclusion of a filtered density field is a suitable extension [53], [54]. Time marching is based on a classical implicit second order fractional step time advancement scheme featuring a mass density explicit/implicit iterative treatment with an explicit iterative scheme to treat convection and streamwise diffusion and an implicit iterative scheme to treat wall normal diffusion. The solver currently uses an “equilibrium” fast-chemistry combustion model with mixture fraction and total enthalpy as primary variables and takes thermodynamic properties from CHEMKIN databases. The primary focus of this work is the extension of an existing turbulent boundary layer code to handle low Mach number flows with heat transfer and combustion capabilities. The original code was provided by Keating; it is described in detail in his PhD dissertation [24]. The extension of the current code is based on the work by Pierce et al. as is presented in his PhD dissertation [53] .

2.1 Governing Equations

The philosophy in large eddy simulation is to decompose the flow field into two regions. The large scales are called the 'resolved' scales and the small scales are also known as the 'subgrid' or 'residual' part. This is achieved by applying a filtering operation in the domain Ω :

$$\bar{\mathbf{u}}(\mathbf{x}, t) = \int_{\Omega} \mathbf{u}(\mathbf{x} - \mathbf{r}, t) G(|\mathbf{r}|; \bar{\Delta}) d\mathbf{r} \quad (1)$$

where $\bar{\mathbf{u}}(\mathbf{x}, t)$ is the filtered velocity, and G is some suitably chosen filtering function. Then the quantity u may be described by $u = \bar{u} + u'$, where \bar{u} is the resolved part and u' is the residual (subgrid) part. This may appear similar to the Reynolds decomposition however \bar{u} refers to a random (and not mean) field, and the filtered residual may not be zero $\bar{u}' \neq 0$. The filtering function G by definition also satisfies the normalization condition $\int G(r, x) dr = 1$. In a finite difference approach the filter function is a simple top-hat filter, having a cut off frequency corresponding to the grid size itself. The filter operation can then be applied to the incompressible fluid equations to obtain the governing equations for the large scale variables.

In this section the governing equations consist of conservation of mass, momentum and multi-scalar transport where the scalars transported are mixture fraction and total enthalpy. These are now written in dimensionless form as:

$$\frac{\partial \bar{u}_i}{\partial x_i} = 0 \quad (2)$$

$$\frac{\partial \bar{u}_i}{\partial t} + \frac{\partial \overline{u_i u_j}}{\partial x_j} = \frac{1}{Re} \frac{\partial}{\partial x_j} (2\bar{S}_{ij}) - \frac{\partial \bar{p}}{\partial x_i} \quad (3)$$

$$\frac{\partial \bar{Z}}{\partial t} + \frac{\partial \overline{Z u_j}}{\partial x_j} = \frac{1}{Re Pr} \frac{\partial^2 \bar{Z}}{\partial x_j \partial x_j} \quad (4)$$

where \bar{u}_i is the resolved velocity, \bar{p} is the pressure, Z is the mixture fraction scalar, Re is the Reynolds number of the flow and Pr is the Prandtl number of the fluid. S_{ij} is the rate deformation tensor, for a solenoidal field $\frac{\partial u_i}{\partial x_i} = 0$. This equation differs from the unfiltered Navier Stokes equation because the filtered product $\overline{u_i u_j}$ is not equal to the product of the filtered velocities $\bar{u}_i \bar{u}_j$. The difference is now defined as the residual stress tensor, $\tau_{ij}^R = \overline{u_i u_j} - \bar{u}_i \bar{u}_j$, which is analogous to the Reynolds stress tensor $\langle u_i u_j \rangle = \langle u_i u_j \rangle - \langle u_i \rangle \langle u_j \rangle$. The residual isotropic kinetic energy is $k_r = \frac{1}{2} \tau_{ii}^R$ and the anisotropic residual stress tensor is defined by $\tau_{ij}^r = \tau_{ij}^R - \frac{2}{3} k_r \delta_{ij}$. In terms of anisotropy tensors, the Reynolds stress tensor can be written as $\tau_{ij}^R = \tau_{ij}^r + \frac{2}{3} k_r \delta_{ij}$ leading to the following expression $\overline{u_i u_j} = \tau_{ij}^r + \frac{2}{3} k_r \delta_{ij} + \bar{u}_i \bar{u}_j$ that when substituted for the convective term in equation (3) leads to a modified pressure defined as the sum of the filtered pressure and the isotropic residual stress $\bar{p} = \bar{p} + \frac{2}{3} \rho k_r$. It is only the anisotropic component τ_{ij}^r that is effective in transporting momentum. Substituting this into the filtered Navier Stokes and similarly for the scalar yields:

$$\frac{\partial \bar{u}_i}{\partial t} + \frac{\partial \bar{u}_j \bar{u}_i}{\partial x_j} = \frac{1}{Re} \frac{\partial}{\partial x_j} (2\bar{S}_{ij}) - \frac{\partial \tau_{ij}^r}{\partial x_j} - \frac{1}{\rho} \frac{\partial \bar{p}}{\partial x_i} \quad (5)$$

$$\frac{\partial \bar{Z}}{\partial t} + \frac{\partial \bar{Z} \bar{u}_j}{\partial x_j} = \frac{1}{RePr} \frac{\partial^2 \bar{Z}}{\partial x_j \partial x_j} - \frac{\partial q_j}{\partial x_j} \quad (6)$$

where the subgrid-scale stress term τ_{ij} , and the subgrid-scale heat flux term q_j , contains the effects of the subgrid-scales on the resolved scales:

$$\tau_{ij} = \overline{u_i u_j} - \bar{u}_i \bar{u}_j \quad (7)$$

$$q_j = \overline{Z u_j} - \bar{Z} \bar{u}_j \quad (8)$$

These terms contain quantities that cannot be explicitly obtained from the resolved fields and must be modeled. As in classical mechanics, the rate of strain tensor and characteristic rate of strain can be defined for the filtered variables as follows:

$$\bar{S}_{ij} = \frac{1}{2} \left(\frac{\partial \bar{u}_i}{\partial x_j} + \frac{\partial \bar{u}_j}{\partial x_i} \right) \quad (9)$$

$$|\bar{S}| = (2\bar{S}_{ij}\bar{S}_{ij})^{1/2} \quad (10)$$

2.2 *Smagorinsky modeling*

Using a classical Smagorinsky type model where one assumes isotropicity and homogeneity of the smallest eddies, τ_{ij}^r can be parametrized by an eddy viscosity model of the following form:

$$\tau_{ij}^R - \frac{\delta_{ij}}{3} \tau_{kk}^R = \tau_{ij}^r = -2\nu_t \bar{S}_{ij} = -2C_{ev} \Delta^2 |\bar{S}_{ij}| \bar{S}_{ij} \quad (11)$$

where δ_{ij} is the Kronecker delta, ν_t is the eddy viscosity and $|\bar{S}_{ij}|$ is the magnitude of the large-scale strain rate tensor. Note that the trace of the subgrid scale stresses is

incorporated in the pressure term as described earlier. Also, Δ is the filter width which reads for a finite difference discretization as $\Delta = (\Delta x \Delta y \Delta z)^{\frac{1}{3}}$. By analogy with what is normally done with the ensemble Reynolds equations, the subgrid scale tensors are in most of the cases expressed in terms of eddy viscosity and diffusivity coefficients in the form: $\tau_{ij}^r = \frac{\delta_{ij}}{3} \tau_{kk} - 2\nu_t \bar{S}_{ij}$, and for a scalar (i.e., mixture fraction Z) a similar model can be used to parameterise the subgrid-scale heat flux:

$$q_j = \alpha_t \frac{\partial \bar{Z}}{\partial x_j} \quad (12)$$

where the subgrid scale eddy diffusivity is modeled similarly to the eddy viscosity with:

$$\alpha_t = C_\theta \Delta^2 |\bar{S}| \quad (13)$$

where C_θ can either be calculated using a subgrid-scale turbulent Prandtl number, $C_\theta = C_{ev}/Pr_t$, or by using a dynamic procedure. Then the LES equations for momentum and scalar transport become:

$$\frac{\partial \bar{u}_i}{\partial t} + \frac{\partial \bar{u}_j \bar{u}_i}{\partial x_j} = \frac{\partial}{\partial x_j} [(\nu + \nu_t)(2\bar{S}_{ij})] - \frac{1}{\rho} \frac{\partial \bar{p}}{\partial x_i} \quad (14)$$

$$\frac{\partial \bar{Z}_i}{\partial t} + \frac{\partial (\bar{u}_j \bar{Z})}{\partial x_j} = \frac{\partial}{\partial x_j} \left[(\alpha + \alpha_t) \left(\frac{\partial \bar{Z}}{\partial x_j} \right) \right] \quad (15)$$

where as described earlier $\bar{p} = \bar{p} + \frac{1}{3} \tau_{kk}$ is a modified pressure (macro pressure), which can be determined with the aid of the filtered continuity equation [55].

2.3 Residual stress decomposition

A decomposition of the residual stresses will now be presented to introduce the commonly used three component stresses: Leonard, Cross and SGS Reynolds stresses.

This is obtained from the decomposition of $u = \bar{u} - u'$ to obtain $\tau^R = L_{ij} + C_{ij} + R_{ij}$

$$\tau_{ij}^R = \overline{u_i u_j} - \bar{u}_i \bar{u}_j \quad (16)$$

$$\tau_{ij}^R = \overline{(\bar{u}_i + u'_i)(\bar{u}_j + u'_j)} \quad (17)$$

$$\tau_{ij}^R = \overline{\bar{u}_i \bar{u}_j + \bar{u}_i u'_j + u'_i \bar{u}_j + u'_i u'_j} \quad (18)$$

$$\tau_{ij}^R = \overline{\bar{u}_i \bar{u}_j} + \overline{\bar{u}_i u'_j} + \overline{u'_i \bar{u}_j} + \overline{u'_i u'_j} \quad (19)$$

$$\tau_{ij}^R = \underbrace{\overline{\bar{u}_i \bar{u}_j} - \bar{u}_i \bar{u}_j}_{L_{ij}} + \underbrace{\overline{\bar{u}_i u'_j} + \overline{u'_i \bar{u}_j}}_{C_{ij}} + \underbrace{\overline{u'_i u'_j}}_{R_{ij}} \quad (20)$$

$$\tau_{ij}^R = L_{ij} + C_{ij} + R_{ij} \quad (21)$$

The Leonard stress tensor is explicit since it is defined in terms of the filtered field, and it has been used in scale similarity models to provide information on subgrid stresses [4].

Leonard's stresses are also a major ingredient of the Germano's identity for the dynamic approach in physical space. The subgrid scale tensors and fluxes presented need of course to be modeled.

2.4 Dynamic modeling

The dynamic model provides a methodology to determine an appropriate local value for C_s to be used with a Smagorinsky type model. The underlying principle is to extract information via a double filtering operation in physical space [52]. Two grid filters are

now introduced: the grid filter $\bar{\Delta}$ and the test filter $\tilde{\Delta}$. The grid filter's width is usually taken to be that of the grid spacing, h , or $2h$ for better resolution. The operation of grid filtering is denoted by an overbar, e.g.,

$$\bar{\mathbf{u}}(\mathbf{x}, t) = \int \mathbf{u}(\mathbf{x} - \mathbf{r}, t) G(|\mathbf{r}|; \bar{\Delta}) d\mathbf{r} \quad (22)$$

The test filter, of larger width, is defined as $\hat{\Delta} = \alpha \bar{\Delta}$ (for instance $\alpha = 2$).

$$\hat{\mathbf{u}}(\mathbf{x}, t) = \int \mathbf{u}(\mathbf{x} - \mathbf{r}, t) G(|\mathbf{r}|; \hat{\Delta}) d\mathbf{r} \quad (23)$$

Since $\bar{\mathbf{u}}(\mathbf{x}, t)$ is unknown in a LES calculation, it is more relevant to consider the test filter applied to $\bar{\mathbf{u}}$, to yield the doubly filtered quantity $\hat{\mathbf{u}}$. Thus, for both filters, the double-filtering operation can be written as

$$\hat{\mathbf{u}}(\mathbf{x}, t) = \int \mathbf{u}(\mathbf{x} - \mathbf{r}, t) G(|\mathbf{r}|; \hat{\Delta}) d\mathbf{r} \quad (24)$$

Accordingly, the subtest-scale stresses and scalar flux appear which are parameterized as

$$T_{ij} = \widehat{\bar{u}_i \bar{u}_j} - \hat{u}_i \hat{u}_j \quad (25)$$

$$Q_j = \widehat{\bar{Z} \bar{u}_j} - \hat{Z} \hat{u}_j \quad (26)$$

In the dynamic SGS model, these are modeled in the same manner as the residual terms,

$$T_{ij} - \frac{\delta_{ij}}{3} T_{kk} = -2C_{ev} \hat{\Delta}^2 |\hat{S}| \hat{S}_{ij} \quad (27)$$

$$Q_j = -\widehat{\alpha}_t \frac{\partial \widehat{Z}}{\partial x_j}, \quad \widehat{\alpha}_t = C_\theta \widehat{\Delta}^2 |\widehat{S}| \quad (28)$$

Test filtering the residual stress tensor $\widehat{\tau}_{ij}^R = \widehat{u}_i \widehat{u}_j - \widehat{u}_i \widehat{u}_j$ and subtracting it from subtest-scale stress tensor defines what is known as the Germano's identity. It yields the known Leonard subtest scale stress also known as the resolved (turbulent) stress. Similarly, subtracting the filtered residual heat flux vector from the subtest-scale scalar flux yields,

$$L_{ij} = T_{ij} - \widehat{\tau}_{ij}^R = \widehat{u}_i \widehat{u}_j - \widehat{u}_i \widehat{u}_j \quad (29)$$

$$F_j = Q_j - \widehat{q}_j = \widehat{Z} \widehat{u}_j - \widehat{Z} \widehat{u}_j \quad (30)$$

Its main advantage is that it is known in terms of \widehat{u} , whereas T_{ij} , τ_{ij}^R , q_j and Q_j are not. They are the contribution to the residual stress (and scalar flux) from the largest resolved motions (with respect to the test filter). By substituting the eddy viscosity and diffusivity models for L_{ij} and F_{ij} , one finds that the coefficient C_{ev} and C_θ are determined by relations,

$$\begin{aligned} L_{ij} - \frac{\delta}{3} L_{kk} &= -C_{ev} \widehat{\Delta}^2 M_{ij}, \quad M_{ij} \\ &= -\left(2 \widehat{\Delta}^2 \widehat{S} \widehat{S}_{ij} - 2 \widehat{\Delta}^2 \widehat{S} \widehat{S}_{ij} \right) \end{aligned} \quad (31)$$

$$F_j = -C_\theta \widehat{\Delta}^2 N_j, \quad N_j = -\left(\widehat{\Delta}^2 \widehat{S} \frac{\partial \widehat{Z}}{\partial x_j} - \widehat{\Delta}^2 \widehat{S} \frac{\partial \widehat{Z}}{\partial x_j} \right) \quad (32)$$

Similarly, the double filtered deformation tensor is defined $\widehat{S}_{ij} = \frac{1}{2} \left(\frac{\partial \widehat{u}_i}{\partial x_j} + \frac{\partial \widehat{u}_j}{\partial x_i} \right)$ and its characteristic counter part also as $|\widehat{S}| = (2\widehat{S}_{ij}\widehat{S}_{ij})^{1/2}$. Further, taking C_{ev} to be uniform, a

scale similar tensor M_{ij} was previously defined and can be confirmed by re-expressing the Leonards stress $L_{ij} = T_{ij} - \widehat{\tau}_{ij}^R$ and obtaining the following expression which contains M_{ij} : $L_{ij} = -2C_{ev} \widehat{\Delta}^2 |\widehat{S}| \widehat{S}_{ij} + 2C_{ev} \bar{\Delta}^2 |\bar{S}| \bar{S}_{ij}$, yielding the final relationship,

$$L_{ij} = C_{ev} M_{ij} \quad (33)$$

We may observe that both M_{ij} and L_{ij} are known in terms of $u(x, t)$, which can be used to determine C_{ev} for the present modelling technique. Also, a single coefficient C_{ev} cannot be chosen to match 5 independent equations. Therefore, a mean square error is minimized. Following Lilly et al [56], the square of the residual is required to be minimal and an equation for the local value of C_{ev} is:

$$C_{ev}(\mathbf{x}, t) = -\frac{1}{2} \frac{\langle L_{ij} M_{ij} \rangle_{avg}}{\langle M_{ij} M_{ij} \rangle_{avg}} \quad (34)$$

Where the brackets $\langle \rangle_{avg}$ indicate the type of averaging in the numerator and denominator used to overcome instabilities (Standard techniques used are line and plane spatial averaging or Lagrangian averaging for general inhomogeneous flows in which weighted averages are formed backward in time along fluid-particle paths based on the filtered velocity field [55]). With this procedure the eddy viscosity tends to zero near the wall without the use of a Van Driest type of damping function. In addition, C_{ev} can take on negative values and apparently capture the effects of backscattering. Similarly, the eddy diffusivity model coefficient C_θ is now computed based on similar formulation,

$$C_\theta(\mathbf{x}, t) = -\frac{\langle F_j N_j \rangle_{avg}}{\langle N_j N_j \rangle_{avg}} \quad (35)$$

where the coefficient C_θ is computed through Lagrangian averaging and is limited to positive values.

2.5 Extension to a variable mass density formulation

This section includes the principles and methodology needed to account for the effects of variable mass-density in the governing LES equations. The introduction of mass density weighted average, Favre averaging, is needed to satisfy the continuity equation while also retaining the standard form of the governing equations. The modeling corresponds to subsonic flows where the magnitude of the velocity corresponds to the low-mach number regime. The LES modeling terms are introduced and it is shown that the inclusion of the filtered density field is a suitable extension to the turbulence model. Recall that in this work, filtering is implicitly defined by the computational grid used for the large-scale equations and that it is not invoked explicitly. Quantities per unit volume are treated using the Reynold decomposition,

$$\rho = \bar{\rho} + \rho'$$

while quantities per unit mass are best described by a Favre (density weighted) decomposition, $u = \tilde{u} + u''$, where

$$\tilde{u} = \frac{\overline{\rho u}}{\bar{\rho}} = \frac{\int \int \int_\Omega G(|\mathbf{r}|; \tilde{\Delta}) \rho((\mathbf{x} - \mathbf{r}), \mathbf{t}) u((\mathbf{x} - \mathbf{r}), \mathbf{t}) d\mathbf{r}}{\int \int \int_\Omega G(|\mathbf{r}|; \tilde{\Delta}) \rho((\mathbf{x} - \mathbf{r}), \mathbf{t}) d\mathbf{r}}$$

2.6 Governing Equations and Filtering

With Favre decomposition, filtered variables represent mass-weighted averages over subgrid volumes. This ensures that the filtering process does not alter the form of the conservation laws. Applying these procedures to the working equations, the Favre LES equations are now written as:

Continuity:

$$\frac{\partial \bar{\rho}}{\partial t} + \frac{\partial \bar{\rho} \tilde{u}_j}{\partial x_j} = 0 \quad (36)$$

Momentum:

$$\frac{\partial \bar{\rho} \tilde{u}_i}{\partial t} + \frac{\overline{\rho u_i u_j}}{\partial x_j} = -\frac{\partial \bar{p}}{\partial x_i} + \frac{\partial \bar{\sigma}_{ij}}{\partial x_j}$$

Using the decomposition $\overline{\rho u_i u_j} = \bar{\rho} \tilde{u}_i \tilde{u}_j + (\overline{\rho u_i u_j} - \bar{\rho} \tilde{u}_i \tilde{u}_j)$, where the first term is the LES grid resolved convective flux and the second term the corresponding subgrid scale (SGS) contribution. The filtered viscous stress tensor is modeled as:

$$\bar{\sigma}_{ij} = 2\bar{\mu} \left(\tilde{S}_{ij} - \frac{1}{3} \frac{\partial \tilde{u}_k}{\partial x_k} \delta_{ij} \right), \quad \text{where } \bar{\mu} = \mu(\tilde{T}) = \mu_0 \left(\frac{\tilde{T}}{T_0} \right)^b, \quad b = 0.76$$

where $\tilde{S}_{ij} = \frac{1}{2} \left(\frac{\partial \tilde{u}_i}{\partial x_j} + \frac{\partial \tilde{u}_j}{\partial x_i} \right)$. It is also customary (in the literature) to define the stress tensor

as $\bar{\sigma}_{ij} = 2\bar{\mu}(\tilde{S}_{ij}^d)$, where now the deviatoric deformation tensor is defined as $\tilde{S}_{ij}^d =$

$\frac{1}{2} \left(\frac{\partial \tilde{u}_i}{\partial x_j} + \frac{\partial \tilde{u}_j}{\partial x_i} \right) - \frac{1}{3} \nabla \cdot \tilde{u}_j \delta_{ij}$. Incorporating the decomposition yields the following

momentum equations,

$$\frac{\partial \bar{\rho} \tilde{u}_i}{\partial t} + \frac{\partial \bar{\rho} \tilde{u}_i \tilde{u}_j}{\partial x_j} = -\frac{\partial \bar{p}}{\partial x_i} - \frac{\partial \tau_{ij}}{\partial x_i} + \frac{\partial}{\partial x_j} (2\bar{\mu} \tilde{S}_{ij}^d) \quad (37)$$

where $\tau_{ij} = \bar{\rho}(u_i \tilde{u}_j - \tilde{u}_i \tilde{u}_j)$ are the same terms that must be modeled.

Scalar Transport:

$$\frac{\partial \bar{\rho} \tilde{Z}}{\partial t} + \frac{\partial \overline{\rho Z u_j}}{\partial x_j} = \frac{\partial}{\partial x_i} \left(\overline{\rho \alpha \frac{\partial Z}{\partial x_i}} \right)$$

Again, we can use the standard LES decomposition: $\overline{\rho Z u_j} = \bar{\rho} \tilde{Z} \tilde{u}_j + (\overline{\rho Z u_j} - \bar{\rho} \tilde{Z} \tilde{u}_j)$,

where the first term is the LES grid resolved convective scalar flux and the second term

the corresponding SGS contribution. We approximate $\overline{\rho \alpha \frac{\partial Z}{\partial x_i}} = \bar{\alpha} \frac{\partial \tilde{Z}}{\partial x_i}$, where $\bar{\alpha} = \bar{\alpha}(\tilde{T}) =$

$\frac{\mu(\tilde{T})c_p}{Pr}$, which finally yields the following filtered LES, Favre averaged equation:

$$\frac{\partial \bar{\rho} \tilde{Z}}{\partial t} + \frac{\partial \bar{\rho} \tilde{Z} \tilde{u}_j}{\partial x_j} = \frac{\partial}{\partial x_i} \left(\bar{\rho} \tilde{\alpha} \frac{\partial \tilde{Z}}{\partial x_i} \right) - \frac{\partial q_j}{\partial x_j} \quad (38)$$

where, $q_j = \bar{\rho}(\tilde{Z} \tilde{u}_j - \tilde{Z} \tilde{u}_j)$

State relation:

$$\bar{p} = \bar{\rho}(R/M) \tilde{T} \quad (39)$$

2.7 Dynamic Modeling

The extension to variable density of the SGS dynamic modeling is presented by inspection of the turbulent (and scalar flux) stress constituents

$$\tau_{ij} = \left(\tau_{ij} - \tau_{kk} \frac{\delta_{ij}}{3} \right) + \tau_{kk} \frac{\delta_{ij}}{3} = \tau_{ij}^A + \tau_{ij}^I \quad (40)$$

The anisotropic part is modeled based on an eddy-viscosity concept:

$$\tau_{ij}^A = -2\bar{\rho}v_\tau \tilde{S}_{ij} \quad (41)$$

Invoking the classical Smagorinsky model, where C_{ev} is the model coefficient that is dynamically computed from the LES solution

$$v_\tau = (C_{ev} \Delta)^2 |\tilde{S}| \quad (42)$$

The anisotropic part is as follows,

$$\tau_{ij}^A = -2\bar{\rho}(C_{ev} \Delta)^2 |\tilde{S}| \tilde{S}_{ij}^A \quad (43)$$

Although not accounted for in the present work, previous researchers have additionally modeled the isotropic constituent of the subgrid scale stress tensor based on the Yoshiwaza relation [6] from which $k_{sgs} = (C_I \Delta)^2 |\tilde{S}|^2$, we have

$$\tau_{kk} = 2\bar{\rho}(C_I \Delta)^2 |\tilde{S}|^2 \quad (44)$$

and the entire modeled term becomes

$$\tau_{ij} = -2\bar{\rho}(C_{ev} \Delta)^2 |\tilde{S}| \tilde{S}_{ij}^A + \frac{\delta_{ij}}{3} 2\bar{\rho}(C_I \Delta)^2 |\tilde{S}|^2 \quad (45)$$

where C_I is a model coefficient. Erlebacher et al [57],[58] neglected the isotropic term on the grounds that it is negligible compared to the thermodynamic pressure. Similarly, Pierce et al also left this term out since the authors decoupled pressure from the thermodynamic variables as in done for low-mach number flows [53]. Currently, a low

Mach number formulation is utilized which neglects acoustic interactions and compressibility effects. This present approach therefore leaves out the isotropic term and the modeling becomes:

$$\tau_{ij} = -2\bar{\rho}(C_{ev} \Delta)^2 |\tilde{S}| \tilde{S}_{ij} \quad (46)$$

In order to close the momentum equations, τ_{ij} must be modeled: (Using $\tilde{f} = \overline{\rho f} / \bar{\rho}$)

$$\tau_{ij} = \bar{\rho}(\tilde{u}_i \tilde{u}_j - \tilde{u}_i \tilde{u}_j) \quad (47)$$

$$= \overline{\rho u_i u_j} - \left(\frac{\overline{\rho u_i} \overline{\rho u_j}}{\bar{\rho}} \right) \quad (48)$$

Utilization of the spectral data is performed with the introduction of the test filter in the resolved field. This has a larger width than the resolved grid filter, generating a region with larger scales which can be used dynamically. This width is denoted as $\hat{\Delta}$. Therefore, the test filtered stresses T are defined as:

$$T_{ij} = \overline{\widehat{\rho u_i u_j}} - \frac{(\widehat{\rho u_i} \widehat{\rho u_j})}{\hat{\rho}} \quad (49)$$

Using Germano's identity, the Leonard stresses L_{ij} can be expressed in terms of T_{ij} and

τ_{ij}

$$\begin{aligned} L_{ij} &= T_{ij} - \hat{\tau}_{ij} \\ &= \overline{\widehat{\rho u_i u_j}} - \frac{(\widehat{\rho u_i} \widehat{\rho u_j})}{\hat{\rho}} - \left(\overline{\rho u_i u_j} - \left(\frac{\overline{\rho u_i} \overline{\rho u_j}}{\bar{\rho}} \right) \right) \end{aligned} \quad (50)$$

$$\begin{aligned}
&= \overline{\widehat{\rho \tilde{u}_i \tilde{u}_j}} - \frac{\widehat{\rho \tilde{u}_i} \widehat{\rho \tilde{u}_j}}{\widehat{\rho}} \\
&= \overline{\widehat{\rho \tilde{u}_i \tilde{u}_j}} - \frac{\widehat{\rho \tilde{u}_i} \widehat{\rho \tilde{u}_j}}{\widehat{\rho}}
\end{aligned}$$

This identity is useful because it provides results (rhs) which can be obtained from the filtered variables. Knowing L_{ij} and re-expressing it in terms of its modeled terms will yield a useful expression for the dynamic coefficient C_s . The anisotropic part of the Leonard stress tensor therefore becomes:

$$\begin{aligned}
L_{ij} &= T_{ij} - \hat{\tau}_{ij} & (51) \\
&= 2(C_{ev} \overline{\Delta})^2 \overline{\widehat{\rho |\tilde{S}| \tilde{S}_{ij}}} - 2(C_{ev} \widehat{\Delta})^2 \widehat{\rho |\widehat{S}| \widehat{S}_{ij}} \\
&= C_{ev}^2 M_{ij}
\end{aligned}$$

where

$$M_{ij} = \left(2 \overline{\widehat{\rho |\tilde{S}| \tilde{S}_{ij}}} - 2 \left(\frac{\widehat{\Delta}}{\overline{\Delta}} \right)^2 \widehat{\rho |\widehat{S}| \widehat{S}_{ij}} \right) \overline{\Delta}^2$$

This equation corresponds to 5 independent relations for C_{ev} making it overspecified. Therefore, the classical least squares approach is followed to calculate the model coefficients in analogy to the incompressible case.

$$C_{ev}(\mathbf{x}, t) = \frac{\langle L_{ij}M_{ij} \rangle_{avg}}{\langle M_{ij}M_{ij} \rangle_{avg}} \quad (52)$$

2.7.1 SGS scalar flux

A similar solution is obtained through the use of the eddy diffusivity concept to model the SGS heat flux, q_j .

$$q_j = -\bar{\rho}C_\theta \frac{\partial \tilde{T}}{\partial x_j} = -\frac{\bar{\rho} \bar{\Delta}^2 C_{ev} |\tilde{S}|}{Pr_t} \frac{\partial \tilde{T}}{\partial x_j} \quad (53)$$

where $C_\alpha = C_s/Pr_t$. Reynolds and Favre averaging yields the following model terms:

$$q_j = \overline{\rho u_j \phi} - \frac{\overline{\rho u_j \rho \phi}}{\bar{\rho}} \quad (54)$$

The subtest scalar flux now takes the following form:

$$Q_j = \widehat{\overline{\rho u_j \phi}} - \frac{\widehat{\overline{\rho u_j \rho \phi}}}{\widehat{\bar{\rho}}} \quad (55)$$

Through the use of Germano's identity we obtain the scalar Leonards tensor K_{ij} and the Modeling tensor T_j as:

$$K_j = \widehat{\overline{\rho \tilde{u}_j \tilde{\phi}}} - \frac{\widehat{\overline{\rho \tilde{u}_j \rho \tilde{\phi}}}}{\widehat{\bar{\rho}}} \quad (56)$$

$$T_j = \left(\overline{\rho|\tilde{S}|} \frac{\partial \tilde{T}}{\partial x_j} - \left(\frac{\widehat{\Delta}}{\overline{\Delta}} \right)^2 \widehat{\rho|\tilde{S}|} \frac{\partial \hat{T}}{\partial x_j} \right) \overline{\Delta}^{-2} \quad (57)$$

Similarly, to the incompressible version we can solve this over-defined system through the least-squares method for C_θ ,

$$C_\theta(\mathbf{x}, t) = \frac{\langle K_j T_j \rangle_{avg}}{\langle T_j T_j \rangle_{avg}} \quad (58)$$

2.8 Time Advancement

2.8.1 Time advancement and iterative scheme

In cases where the viscous time step may be too restrictive, such as resolving the inner region of a boundary layer, or if the grid is very fine near the wall, it is desirable to make the viscous terms of the momentum and scalar equations implicit. This motivates an explicit/implicit treatment of the Low Mach number transport equations where wall-normal diffusion terms are handled implicitly while the rest of the terms - convection, streamwise and spanwise diffusion - are handled explicitly. An implicit integration scheme developed and published initially by Dr. Charles Pierce [53] is utilized to handle the time advancement of the transport equations. It features an iterative sub-scheme that provides an accurate technique for the coupling of the equations. It is the iterative scheme that is semi-implicit while the time advancement scheme is fully implicit.

Consider the following integration example of a differential equation,

$$\frac{\partial u}{\partial t} = -F_c(u) + F_d(u) = RHS(u)$$

The temporal integration scheme proceeds using an implicit method,

$$\frac{u^{n+1} - u^n}{\Delta t} = \frac{1}{2} [(-F_c(u^n) + F_d(u^n)) + (-F_c(u^{n+1}) + F_d(u^{n+1}))] = RHS(u^{n+\frac{1}{2}})$$

which for a linear RHS, becomes a Crank-Nicholson scheme.

This equation is fully integrated using an iterative scheme, which holds the explicit and implicit terms of the discretized equations. The explicit iterative scheme is written as,

$$\frac{u^{n+1,iter+1} - u^n}{\Delta t} = \frac{1}{2} [(-F_c(u^n) + F_d(u^n)) + (-F_c(u^{n+1,iter}) + F_d(u^{n+1,iter}))]$$

while the implicit iterative scheme is written as,

$$\frac{u^{n+1,iter+1} - u^n}{\Delta t} = \frac{1}{2} \left[(-F_c(u^n) + F_d(u^n)) + (-F_c(u^{n+1,iter+1}) + F_d(u^{n+1,iter+1})) \right]$$

The iterative scheme makes use of a “fractional step” method. The sequence of the projection method consists of first advancing the scalar fields, solving for a predicted intermediate velocity, obtaining a solution of the Poisson equation for the pressure, and applying a correction to the velocity (and pressure fields) to enforce conservation of mass. The discrete form of mass and momentum conservation is presented below for reference where the mass flux vector is defined as $g_j = \rho u_j$ (all quantities are functions of spatial coordinates (i, j and k indices are left out for clarity))

$$\frac{\rho^{n+1} - \rho^n}{\Delta t} + \frac{\partial g_j}{\partial x_j} = 0$$

$$\frac{g_i^{n+1} - g_i^n}{\Delta t} = R_i - \frac{\partial p}{\partial x_i}$$

The staggered discretization methodology consists of evaluating the scalars at full time steps $t(n)$ and velocities at half time steps $t(n + 1/2)$. In the momentum equations, the convective and diffusive terms represented by R_i are evaluated at $t(n + 1/2)$ whereas the pressure term is evaluated at time $t(n + 1)$.

Thus the projection/correction method is presented below.

- Predictor step:

$$\frac{\hat{g}_i - g_i^n}{\Delta t} = R_i^{n+\frac{1}{2},iter} - \frac{\partial}{\partial x_i} (p^{n+1,iter}) \quad (59)$$

- Solution of the Poisson equation: This expression is obtained by taking the divergence of the velocity correction expression. If the pressure satisfies the Poisson equation then conservation of mass is enforced.

$$\frac{\partial^2(\delta p)}{\partial x_i \partial x_i} = \frac{1}{\Delta t} \left[\frac{\rho^{n+1,iter+1} - \rho^n}{\Delta t} + \frac{\partial \hat{g}_j}{\partial x_j} \right] \quad (60)$$

- Correction step: The velocity field is now corrected to enforce conservation of mass as follows (the pressure field is also updated)

$$g_i^{n+1,iter+1} = \hat{g}_i - \Delta t \frac{\partial(\delta p)}{\partial x_i} \quad (61)$$

$$p^{n+1,iter+1} = p^{n+1,iter} + \delta p \quad (62)$$

2.8.2 Discrete Equation

The governing equations are discretized using a 2nd order finite differences approach in a spatio-temporal computational cell as shown in Figure 4. Velocity components are staggered with respect to pressure in both space and time. The density is co-located at the pressure points. Thus, the calculation of the mass flux requires spatial interpolation and is

given the symbol g_i ; where the over-bar averaging operator is defined as: $\bar{u}^{x_i} = \frac{u^n(i)+u^n(i+1)}{2}$ for space and $\bar{u}^t = \frac{u^{n+1}(i)+u^n(i)}{2}$ for time assuming equal spacing. Additionally, mass density is staggered in time, so that effectively the density ρ^n is calculated at time $(n) \Delta t$. Conversion between u_i and g_i is accomplished using the following basic relationships:

$$g_i = \bar{\rho}^{x_i t} u_i, \quad u_i = \frac{g_i}{\bar{\rho}^{x_i t}} \quad (63)$$

Typical to LES non-premixed chemistry models is the use of mixture fraction based combustion models which is helpful in minimizing the number of transported scalars [59]. This is achieved by mapping the details of the multi-component reaction process to a small number of “tracking scalars” that can provide complete chemical state information at a reduced computational expense. In this way, the information obtained from the mixture fraction relates the mixture composition of an inflow and oxidizer stream to the local mixture. Normally a mixture fraction variable is assigned a value of 1 in the fuel stream and zero in the oxidizer stream. The two tracking scalars used in our multi-scalar approach are the mixture fraction and the total enthalpy formulation; it is a robust approach typically used for low Mach number flows. The fully discrete equations are now presented in the following form,

Continuity:

$$\frac{\partial \rho}{\partial t} + \frac{\partial g_j}{\partial x_j} = 0 \quad (64)$$

Multi-scalar Transport: (Mixture fraction and enthalpy as scalar 1 & 2 respectively)

$$\frac{\partial}{\partial t}(\rho Z) + \frac{\partial}{\partial x_j} \left(g_j \overline{Z}^{x_j t} \right) = + \frac{\partial}{\partial x_j} \left[\overline{\rho \alpha}^{x_j t} \frac{\partial}{\partial x_j} (\overline{Z}^t) \right] \quad (65)$$

$$\frac{\partial}{\partial t}(\rho h) + \frac{\partial}{\partial x_j} \left(g_j \overline{h}^{x_j t} \right) = + \frac{\partial}{\partial x_j} \left[\overline{\rho \alpha}^{x_j t} \frac{\partial}{\partial x_j} (\overline{h}^t) \right] \quad (66)$$

Momentum:

$$\frac{\partial}{\partial t}(g_i) + \frac{\partial}{\partial x_j} \left(\overline{g_j}^{x_i t} \overline{u_i}^{x_j t} \right) = - \frac{\partial}{\partial x_i}(p) + \frac{\partial}{\partial x_j}(\tau_{ij}) \quad (67)$$

$$\tau_{ij} = \begin{cases} \overline{\mu}^{x_i x_j} \left[\frac{\partial \overline{u_i}^t}{\partial x_j} + \frac{\partial \overline{u_j}^t}{\partial x_i} \right], & \text{if } i \neq j \\ 2\mu \left[\frac{\partial \overline{u_i}^t}{\partial x_j} - \frac{1}{3} \frac{\partial \overline{u_k}^t}{\partial x_k} \delta_{ij} \right], & \text{if } i = j \end{cases}$$

For clarity the above compact notation can be expanded in more conventional form. For instance, the continuity equation in two dimensions for a staggered cell in time-space would be expanded as,

Continuity:

$$\begin{aligned}
& \frac{\rho_{i,j}^{n+1} - \rho_{i,j}^n}{\Delta t} + \frac{1}{4 \Delta x} [(\rho_{i+1,j}^{n+1} + \rho_{i,j}^{n+1} + \rho_{i+1,j}^n + \rho_{i,j}^n)u_{i,j}^{n+1} \\
& \quad - (\rho_{i,j}^{n+1} + \rho_{i-1,j}^{n+1} + \rho_{i,j}^n + \rho_{i-1,j}^n)u_{i-1,j}^{n+1}] \\
& + \frac{1}{4 \Delta y} [(\rho_{i,j+1}^{n+1} + \rho_{i,j}^{n+1} + \rho_{i,j+1}^n + \rho_{i,j}^n)v_{i,j}^{n+1} - (\rho_{i,j}^{n+1} + \rho_{i,j-1}^{n+1} + \rho_{i,j}^n + \rho_{i,j-1}^n)v_{i,j-1}^{n+1}] \\
& = 0
\end{aligned} \tag{68}$$

Scalar Transport:

This equation is decomposed into two steps (an explicit step for convection, streamwise and spanwise diffusion and an implicit step for cross-stream diffusion) and is discretized as follows (where $f = (\rho\phi)$ is a generic term for each parameter $\phi = \{Z, h\}$):

Explicit step

$$\begin{aligned}
& \frac{f_j^{n+1,iter+*} - f_j^n}{\Delta t} = \\
& - \frac{1}{4(x_j - x_{j-1})} [g_j^{n+1,iter} (\phi_{j+1}^{n+1,iter} + \phi_j^{n+1,iter} + \phi_{j+1}^n + \phi_j^n) - g_{j-1}^{n+1,iter} (\phi_j^{n+1,iter} + \phi_{j-1}^{n+1,iter} + \phi_j^n + \phi_{j-1}^n)] \\
& + \frac{1}{4(x_j - x_{j-1})} \left[\frac{1}{2(xc_{j+1} - xc_j)} ((\rho D_\phi)_{j+1}^{n+1,iter} + (\rho D_\phi)_j^{n+1,iter} + (\rho D_\phi)_{j+1}^n + (\rho D_\phi)_j^n) (\phi_{j+1}^{n+1,iter} + \phi_{j+1}^n - \phi_j^{n+1,iter} - \phi_j^n) \right. \\
& \quad \left. - \frac{1}{2(xc_j - xc_{j-1})} ((\rho D_\phi)_j^{n+1,iter} + (\rho D_\phi)_{j-1}^{n+1,iter} + (\rho D_\phi)_j^n + (\rho D_\phi)_{j-1}^n) (\phi_j^{n+1,iter} + \phi_j^n - \phi_{j-1}^{n+1,iter} - \phi_{j-1}^n) \right]
\end{aligned}$$

where the convective terms are summed over $j = 1, 2$ and 3 , and where the diffusive terms are summed over $j = 1$ and 3 ($j = 2$ is assumed to be the wall normal direction).

Implicit step

$$\begin{aligned} \frac{f_j^{n+1,iter+1} - f_j^{n+1,iter+*}}{\Delta t} = & \\ + \frac{1}{4(x_j - x_{j-1})} & \left[\frac{1}{2(xc_{j+1} - xc_j)} ((\rho D_\phi)_{j+1}^{n+1,iter} + (\rho D_\phi)_j^{n+1,iter} + (\rho D_\phi)_{j+1}^n + (\rho D_\phi)_j^n) (\phi_{j+1}^{n+1,iter+1} + \phi_{j+1}^n - \phi_j^{n+1,iter+1} - \phi_j^n) \right. \\ & \left. - \frac{1}{2(xc_j - xc_{j-1})} ((\rho D_\phi)_j^{n+1,iter} + (\rho D_\phi)_{j-1}^{n+1,iter} + (\rho D_\phi)_j^n + (\rho D_\phi)_{j-1}^n) (\phi_j^{n+1,iter+1} + \phi_j^n - \phi_{j-1}^{n+1,iter+1} - \phi_{j-1}^n) \right] \end{aligned}$$

where $j = 2$ (wall normal direction). Note that the discretization implicitly assumes a uniform grid and that (small) errors will occur when using (slightly) non-uniform grids.

2.9 Iterative Scheme

This section presents the mass density iterative algorithm in seven subsequent steps, a flow chart of this algorithm is presented in Figure 5. The purpose of the iterative loop is to provide a second order accuracy in time integration scheme as well as coupling between the scalar and flow equations. The initial time step is followed by the actual density iteration loop; in this implementation the loop is contained within steps 2 through 7 where a demanding mass density convergence criterion is imposed; once converged the simulation advances to the next sub-step. The staggered spatio-temporal cells for the scalar and momentum equations are also presented at each stage of the description.

The detailed algorithm and its physical description is presented below,

STEP 1: INITIALIZATION (before start of iterative loop)

- Initial guess ($iter = 0$) of mass density:

$$\rho^{n+1, iter=0} = 2\rho^n - \rho^{n-1}$$

$$\text{and } \phi^{n+1, iter=0} = \phi^n ; D_\phi^{n+1, iter=0} = D_\phi^n ; u_j^{n+1, iter=0} = u_j^n ; g_j^{n+1, iter=0} = g_j^n$$

STEP 2: SCALAR EQUATIONS (start of iterative loop, from $iter$ to $iter+1$)

New to the formulation of this scheme is the advancement of the scalar equations prior to the momentum equation. Scalar information is needed at this early stage to calculate a mass-density value that will be used in the momentum equations. Figure 3 shows the location of the mass density, scalar fields and scalar flux in the staggered spatio-temporal cell,

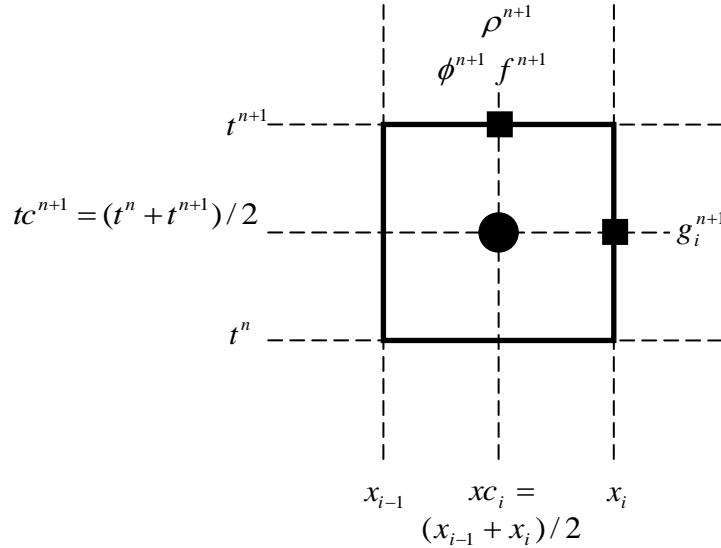


Figure 3. Scalar staggered cell. The right-hand side of the scalar equation is evaluated at the center of the spatio-temporal cell, identified by a black dot.

- Calculate: $g_j^{n+1,iter} = (\overline{\rho^{x_j}})^{n+1/2,iter} \times u_j^{n+1,iter}$, $\phi^{n+1/2,iter} = \overline{\phi}^t$, $(\rho D_\phi)^{n+1/2,iter} = \overline{\rho D_\phi}^t$
- Initialize scalar fields: $f^n = \rho^n \times \phi^n$
- Solve scalar equations: $\partial_t(f) + \partial_{x_j}(g_j \overline{\phi^{x_j}}^t) = \partial_{x_j}(\overline{\rho D_\phi^{x_j}}^t \partial_{x_j}(\overline{\phi}^t))$, where $f = (\rho\phi)$, and provide $f^{n+1,iter+1}$
- Calculate intermediate value $\phi^{n+1,iter+*} = f^{n+1,iter+1} / \rho^{n+1,iter}$ (*iter+** denotes a temporary intermediate value)
- Impose boundary conditions

STEP 3: EQUATION OF STATE (EOS)

Next the thermodynamic equation of state is called to update the density field through the gas molecular weight and provisional results from the scalar advancement as follows,

- Calculate mass density as $\rho^{n+1,iter+1} = M^{n+1,iter+*} / T^{n+1,iter+*}$
- The temperature field is calculated through the enthalpy relationship; where the total enthalpy is defined as, $h = h^o(Z) + \int_{T_0}^T C_p(Z, T') dT'$. A Newton-Rhapson algorithm is used to reconstruct the temperature field.

STEP 4: UPDATE SCALAR FIELDS

Scalar fields are now updated based on the new density field found in STEP 3.

- Calculate $\phi^{n+1,iter+1} = f^{n+1,iter+1} / \rho^{n+1,iter+1}$
- Impose boundary conditions

STEP 5: MOMENTUM EQUATIONS

The intermediate velocity is now calculated and boundary conditions are applied leading to an update of the intermediate momentum field.

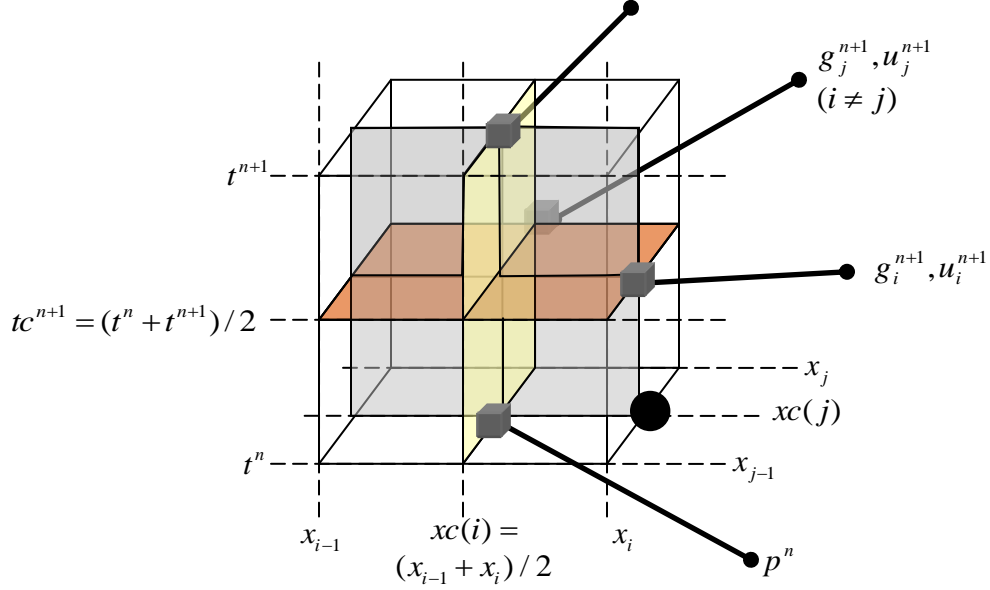


Figure 4. Momentum staggered cell. The right hand side of this equation is evaluated at the bottom right of the spatio-temporal cell, identified by a black dot.

- Calculate: $g_j^{n+1,iter+*} = \overline{(\rho^{x_j})^{n+1/2,iter+1}} \times u_j^{n+1,iter}$, $(g_j)^{n+1/2,iter} = \overline{g_j^t}$, $(u_j)^{n+1/2,iter} = \overline{u_j^t}$
- Initialize momentum field: $g_j^n = \overline{(\rho^{x_j})^n} \times u_j^n$
- Solve momentum equations: $\partial_t(g_i) + \partial_{x_j}(\overline{g_j^{x_i} u_i^{x_j}}) = -\partial_{x_i} p + \partial_{x_j}(\tau_{ij})$, where $\tau_{ij} = 2\rho V[\partial_{x_i}(\overline{u_i^t}) - \partial_{x_k}(\overline{u_k^t})/3]$, if $i = j$, and $\tau_{ij} = \overline{\rho v^{x_i x_j}} [\partial_{x_j}(\overline{u_i^t}) + \partial_{x_i}(\overline{u_j^t})]$, if $i \neq j$, and provide $g_j^{n+1,iter+**}$
- Calculate intermediate velocity $u_j^{n+1,iter+**} = g_j^{n+1,iter+**} / \overline{(\rho^{x_j})^{n+1/2,iter+1}}$

- Impose boundary conditions
- Calculate intermediate momentum field $\hat{g}_j = (\overline{\rho^{x_j}})^{n+1/2, iter+1} \times u_j^{n+1, iter+**}$

STEP 6: PRESSURE EQUATION

This step requires the solution of the Poisson equation to determine the pressure field correction used in the enforcement of the continuity equation. Application of a projection method including the density fields lead to the following Poisson expression:

- Solve pressure equation: $\partial_{x_k} (\partial_{x_k} \delta p) = \frac{1}{\Delta t} \left[\frac{\rho^{n+1, iter+1} - \rho^n}{\Delta t} + \frac{\partial \hat{g}_j}{\partial x_j} \right]$ and provide

$$\delta p = p^{n+1, iter+1} - p^{n+1, iter}$$

Prescription of the Neumann conditions for the Poisson equation requires that the volume integral of the right hand side of the pressure field be equal to zero $\iiint \left[\frac{d\rho}{dt} + \frac{\partial \hat{g}_j}{\partial x_j} \right] = 0$, this is enforced at the outflow Orlandy boundary and is a required compatibility condition.

STEP 7: UPDATE VELOCITY AND PRESSURE (end of iterative loop)

- Calculate:

$$g_j^{n+1, iter+1} = \hat{g}_j - \Delta t \times \partial_{x_j} (\delta p)$$

$$p^{n+1, iter+1} = p^{n+1, iter} + \delta p$$

$$u_j^{n+1, iter+1} = g_j^{n+1, iter+1} / (\overline{\rho^{x_j}})^{n+1/2, iter+1}$$

- Impose boundary conditions

- Check for convergence
- Prepare for next time step

Updating the velocity and pressure fields ensures that the continuity equation is satisfied. Steps 2 through 7 of the present iterative scheme describe a single mass density iteration. Successful convergence of this loop is based on a criterion that checks for small changes of mass density (or pressure variations, or right hand side of momentum equation) from one iteration level to the next. Figure 5 shows the algorithm flow chart.

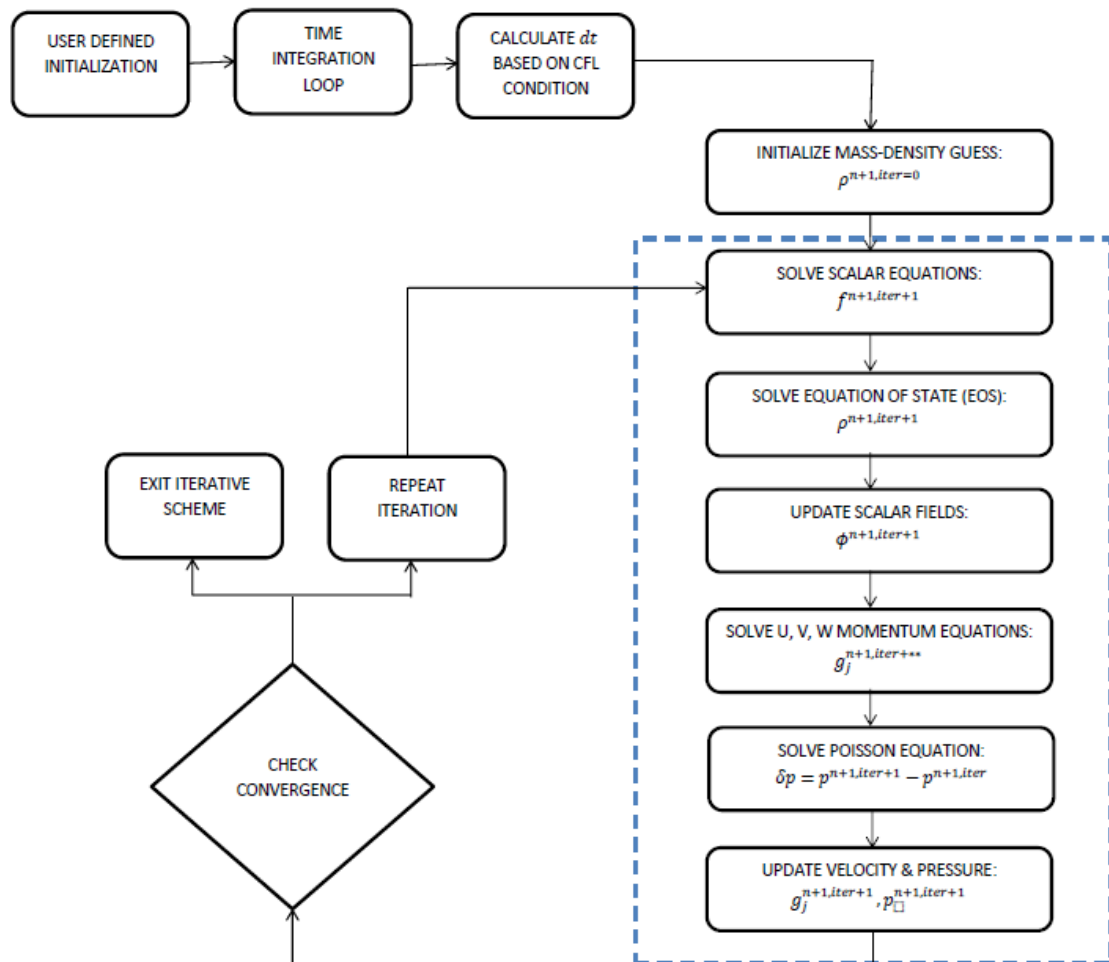


Figure 5. Flow chart showing the mass density iterative scheme and time integration advancement.

2.10 QUICK scheme for scalar transport

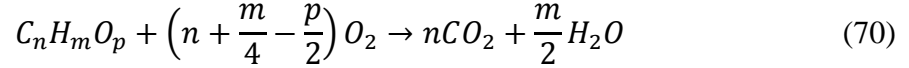
The QUICK scheme (Quadratic Upstream Interpolation for Convective Kinetics) is used in the discretization of the convective terms of the scalar transport equations while retaining the use of central differencing for the diffusion terms. Upwinding schemes introduce numerical dissipation errors, while central differencing schemes are non-dissipative but produce non-physical oscillations in large gradient, high intensity regions. Due to this observation, we have adopted the use of QUICK to improve with the physical bound instability of the scalar transport fields. In its formulation, QUICK considers a three-point upstream weighted quadratic interpolation for the cell phase value by defining a polynomial fitting. The QUICK interpolation on a uniform Cartesian grid is given by

$$\phi_e = \frac{6}{8}\phi_u + \frac{3}{8}\phi_d - \frac{1}{8}\phi_{uu} \quad (69)$$

where D, U, and UU denote the downstream, the first upstream and the second upstream node respectively (E, P and W or P, E, and EE depending on the flow direction) [60].

2.11 Single Step Mixture Fraction Combustion Model

The mixture fraction combustion model is presented below following a classical two variable formulation based on the concept of single step, global combustion equation



where 1 mole of fuel chemically reacts with $\left(n + \frac{m}{4} - \frac{p}{2}\right)$ moles of oxygen from air to form n moles of carbon dioxide and $\left(\frac{m}{2}\right)$ moles of water vapor; Nitrogen from air is implicitly present and is considered an inert species. Conservation of mass for carbon, hydrogen and oxygen gives the following expressions,

$$Y_c = \left(\frac{n\mathcal{M}_c}{\mathcal{M}_{C_nH_mO_p}}\right)Y_{C_nH_mO_p} + \left(\frac{\mathcal{M}_c}{\mathcal{M}_{CO_2}}\right)Y_{CO_2}$$

$$Y_H = \left(\frac{m\mathcal{M}_H}{\mathcal{M}_{C_nH_mO_p}}\right)Y_{C_nH_mO_p} + \left(\frac{2\mathcal{M}_H}{\mathcal{M}_{H_2O}}\right)Y_{H_2O} \quad (71)$$

$$Y_O = \left(\frac{p\mathcal{M}_O}{\mathcal{M}_{C_nH_mO_p}}\right)Y_{C_nH_mO_p} + Y_{O_2} + \left(\frac{\mathcal{M}_O}{\mathcal{M}_{H_2O}}\right)Y_{H_2O} + \left(\frac{2\mathcal{M}_O}{\mathcal{M}_{CO_2}}\right)Y_{CO_2}$$

where Y_k and \mathcal{M}_k represent the mass fraction and molecular weight of atomic/molecular chemical species k . Assuming equal molecular mass diffusivities, Y_c , Y_H , and Y_O can be linearly related to the mixture fraction variable, Z , since they are all chemically conserved variables.

This can be written as,

$$\begin{aligned}
\left(\frac{n\mathcal{M}_c}{\mathcal{M}_{C_nH_mO_p}}\right)Y_{C_nH_mO_p,F}Z &= \left(\frac{n\mathcal{M}_c}{\mathcal{M}_{C_nH_mO_p}}\right)Y_{C_nH_mO_p} + \left(\frac{\mathcal{M}_c}{\mathcal{M}_{CO_2}}\right)Y_{CO_2} \\
\left(\frac{m\mathcal{M}_H}{\mathcal{M}_{C_nH_mO_p}}\right)Y_{C_nH_mO_p,F}Z &= \left(\frac{m\mathcal{M}_H}{\mathcal{M}_{C_nH_mO_p}}\right)Y_{C_nH_mO_p} + \left(\frac{2\mathcal{M}_H}{\mathcal{M}_{H_2O}}\right)Y_{H_2O} \\
\left(\frac{p\mathcal{M}_O}{\mathcal{M}_{C_nH_mO_p}}\right)Y_{C_nH_mO_p,F}Z + Y_{O_2,A}(1-Z) & \\
&= \left(\frac{p\mathcal{M}_O}{\mathcal{M}_{C_nH_mO_p}}\right)Y_{C_nH_mO_p} + Y_{O_2} + \left(\frac{\mathcal{M}_O}{\mathcal{M}_{H_2O}}\right)Y_{H_2O} + \left(\frac{2\mathcal{M}_O}{\mathcal{M}_{CO_2}}\right)Y_{CO_2}
\end{aligned} \tag{72}$$

where the subscripts F and A refer to the fuel and oxygen streams. Thus, the entire reactive mixture composition can be parametrized in terms of the mixture fraction, Z , and a reaction progress variable that can be defined as the fuel mass fraction (the definition is not unique) [8].

2.12 CHEMKIN Thermodynamic Model

The CHEMKIN database is utilized as a set of dynamic look up tables integrated with the present CFD solver. It provides access to thermodynamic properties for the mixture composition as a function of temperature and are stored as two polynomial fits for specific heat, C_p/R , and enthalpy, H^o/RT , (also entropy, S^o/R but not used here) separated at a temperature range of 1000K. The species available are for the gaseous fuel composition, i.e., Ethylene C_2H_4 , Oxygen O_2 , Carbon Dioxide CO_2 , Nitrogen N_2 , and

water vapor H_2O . There are seven coefficients for each of the two temperature ranges, thus for each species there are 14 coefficients. The normalized polynomial fits are presented below for specific heat and enthalpy for the mixture composition where the species mass fractions are evaluated through the mixture fraction and the classical chemical state relationships (subscript k indicates the chemical species),

Specific heat capacity

$$c_{p,mix}^* = \sum_{k=1}^{k=5} [Y_k \times (c_1 + c_2T + c_3T^2 + c_4T^3 + c_5T^4)_k] / c_{p,o} \quad (73)$$

where specific heat is normalized with $c_{p,o} = \frac{\gamma R}{(\gamma-1)} / \mathcal{M}_{air}$,

Enthalpy

$$h_{mix}^* = \sum_{k=1}^{k=5} \left[Y_k \times \left(c_6 + c_1T + \frac{c_2T^2}{2} + \frac{c_3T^3}{3} + \frac{c_4T^4}{4} + \frac{c_5T^5}{5} \right)_k \right] / h_o \quad (74)$$

where enthalpy is normalized with $h_o = (\gamma RT_o / \mathcal{M}_{air}) / (\gamma - 1)$ and R is the universal gas constant, T_o is a reference ambient temperature at 300K, \mathcal{M}_{air} is the molecular weight of air and γ is the ratio of specific heats.

2.13 Inflow Boundary Conditions

2.13.1 Synthetic Turbulent Inflow Generation

The development of inflow generators is an important problem in Computational Fluid Dynamics (CFD) due to its use in investigations of the turbulent fields using LES and DNS methods. These methods require specification of unsteady turbulent fluctuation fields with prescribed statistics at every time step at the inlet of the computational domain. A comprehensive survey of the existing inflow generation methods can be found in Keating et al. [24], and Lund et al. [61]. Classification of different inflow techniques including analysis of their advantages and disadvantages is presented in Keating et al. [62]. Despite its shortcomings the enforcement of artificial turbulent fields with prescribed statistics remains the most popular technique for specification of LES inlet boundary conditions applied solely or in a combination with other methods.

Here we present modern methods for the generation of turbulence fluctuations as inflow conditions for spatially developing (non-periodic) simulations applied to turbulent boundary layers. The synthetic turbulence generation method of Batten et al. [30] has been used to provide the spectral dynamics and turbulence structure as an inflow condition. Although this method represents realistic spectra the phase cannot be recovered and a transitional region is allowed for the turbulence to readjust itself to its target value. To shorten this transitional region a Reynolds shear stress controller developed by Spille-Kohoff et al [31] is utilized at selected planes near the inflow to shorten the redevelopment length and decrease computational time. Previous studies conducted by Keating and co-workers showed that, by using synthetic turbulence at the inflow plane, coupled with controlled forcing, the development length of the turbulent

eddies could be substantially reduced. The forcing method enhances wall-normal velocity fluctuations at several controlled planes downstream of the inflow plane and it is modulated so that a target Reynolds shear stress profile is achieved. In this section we present these methodologies to provide inflow conditions for the turbulent boundary layer test cases in zero pressure gradient environments.

2.13.2 Synthetic Turbulence

We use the synthetic turbulence generation method of Batten [30]. This method requires as input the mean velocity field, information about the Reynolds stress tensor and the specification of a time scale of turbulence τ_b which is calculated from the turbulent kinetic energy and the turbulent dissipation rate ϵ . The method involves the summation of sines and cosines with random amplitudes and phases that yield a velocity field having specified length, time-scales, and energy spectrum. The intermediate velocity is defined as,

$$v_i(x_j, t) = \sqrt{\frac{2}{N}} \sum_{n=1}^N [p_i^n (\cos(\hat{d}_j^n \hat{x}_j^n + \omega^n \hat{t})) + q_i^n (\sin(\hat{d}_j^n \hat{x}_j^n + \omega^n \hat{t}))] \quad (75)$$

where

$$\hat{x}_j = 2\pi x_j / L_b, \quad \hat{t} = 2\pi x_j / \tau_b \quad (76)$$

are the spatial coordinates normalized by the length and time scales of the turbulence. In the above, $\tau_b = k/\epsilon$ and $L_b = \tau_b V_b$ are the turbulence time and length scales, and $V_b = k^{1/2}$ is the velocity scale. The random frequencies $\omega^n = N(1,1)$ are taken from a

normal distribution $N = (\mu, \sigma^2)$ with mean $\mu = 1$ and variance $\sigma^2 = 1$. The amplitudes are given by,

$$p_i^n = \epsilon_{ijk} \zeta_j^n d_k^n, \quad q_i^n = \epsilon_{ijk} \xi_j^n d_k^n \quad (77)$$

where ζ_j^n and $\xi_j^n = N(0,1)$ and

$$\widehat{d}_j^n = d_j^n \frac{V}{c^n} \quad (78)$$

are modified wavenumbers obtained by multiplying the wavenumbers, d_i^n , by the ratio of the velocity scale $V_b = L_b/\tau_b$ to c^n , given by

$$c^n = \sqrt{\frac{3}{2} \langle u'_l u'_m \rangle \frac{d_l^n d_m^n}{d_k^n d_k^n}} \quad (79)$$

The wave numbers $d_i^n = N(0, \frac{1}{2})$ are chosen from the random distribution with variance $1/2$, resulting in a three dimensional spectrum that behaves like $d^4 = \exp(-d^2)$. Although the wave numbers d_i^n are distributed isotropically in a sphere, dividing them by c^n tends to elongate those wavenumbers that are most closely aligned with the largest component of the Reynolds stress tensors, and contract those aligned with the smaller ones. This results in a more physically realistic spectrum of turbulence, with eddies that are more elongated in x near the wall, and tend to be more spherical away from the wall [63].

The synthetic turbulent fluctuation field is finally reconstructed by a tensor scaling:

$$u'_i = a_{ik} v_k \quad (80)$$

where a_{ik} is the Cholesky decomposition of the Reynolds stress tensor.

The simulation presented here uses 200 random modes; this number was required to ensure that the resulting statistics were independent of the number of modes used. Further details of the method can be found in Batten [30], [63].

2.13.3 Reynolds Stress Controller

Spille-Kohoff et al [31] have developed the software for inflow generation method based on the introduction of a forcing term in the wall normal momentum equation. This has the effect of amplifying the velocity fluctuations in that direction to match a desired profile of Reynolds shear stress, thus enhancing the production term in the shear stress budget. A controller is used to determine the forcing amplitude based on the error in the Reynolds shear-stress:

$$e(y, t) = \langle u'v' \rangle(x_o, y) - \langle u'v' \rangle^{z,t}(x_o, y, t) \quad (81)$$

where $\langle u'v' \rangle(x_o, y)$ is the target Reynolds stress tensor at the control plane at $x = x_o$, and $\langle u'v' \rangle^{z,t}(x_o, y, t)$ is the current Reynolds shear stress, averaged over the homogenous (spanwise) direction and time using an exponential window. The forcing aims at the enhancement of (or damping) of local flow events that contribute to the Reynolds shear stress. This is achieved by setting the force magnitude to

$$f(x_o, y, z, t) = r(y, t)[u(x_o, y, z, t) - \langle u \rangle^{z,t}(x_o, y)] \quad (82)$$

where f is related to the error by

$$r(y, t) = \alpha e(y, t) + \beta \int_0^t e(y, t') dt \quad (83)$$

In this study we used $\alpha = 1$ and $\beta = 5$ with a time averaging window of $T_{avg} = 10$ as these were found to be optimal values for a wide variety of turbulent flows (including accelerating/decelerating boundary layers) [63].

2.14 Outflow Boundary Conditions

2.14.1 Orlansky conditions

Outflow conditions are now presented for non-periodic numerical simulations of spatially developing flow such as boundary layers or inflow/outflow channels. At the outflow, the standard Orlansky[64] type boundary condition for momentum driven flows is applied to convect flow out without generating significant waves into the upstream region. The Orlansky condition specifies a hyperbolic convection equation at the outflow for each velocity component

$$\frac{dU_i}{dt} + \langle U_c \rangle \frac{dU_i}{dx_i} = 0 \quad (84)$$

and enforces mass conservation by prescribing a correction term to the outflow velocities.

A convective velocity, U_c , is defined as having either a bulk value $U_c = \iint u_{out}(j, k) dy dz$ or a maximum plane value, $U_c = \max(u_{out}(j, k))$. Its hyperbolic nature (Equation 78) makes it more suitable for momentum driven flow as is evident from the Blasius type results that have been presented in Chapter 2.

2.14.2 Freestream boundary conditions

Following the method of Lund et al [61], a freestream boundary condition is used for boundary layer flows based on continuity arguments that treats the amount of mass leaving the top boundary through linear regression of the displacement thickness, as this behavior is seen for flat plate turbulent boundary layers, the condition can be derived as,

$$\frac{du}{dy} = \frac{dw}{dy} = 0, v_{\infty} = U_{\infty} \frac{d\delta^*}{dx} \quad (85)$$

Where δ^* represents the displacement thickness of the boundary layer and the derivative $\frac{d\delta^*}{dx}$ is calculated through the linear regression and has a constant value for turbulent flows.

2.15 Summary

The fundamental physical submodels and numerical techniques used in modeling turbulent flows have been presented. The time advancement method, including an implicit iterative treatment for the wall-normal diffusion components is described. The implicit iterative treatment removes the time step restriction associated with solving for diffusion in grids that are refined in the wall normal direction. In addition, a coupled equation numerical method for variable density flows, developed by Charles Pierce, has been presented and discussed in detail[53]. This section also includes a description of the physical submodels for combustion and the CHEMKIM database for thermodynamic properties. Lastly, boundary conditions for spatially developing problems have been presented for the complicated problem of inflow turbulent generating techniques (to bypass modeling the entire transition region in turbulent flows), and the Orlansky and outflow boundary conditions.

Chapter 3: Verification

The increasing demand of CFD numerical codes in various scientific and engineering fields calls for methods to establish the accuracy of the numerical scheme. With increases in computational power, CFD practitioners often focus on solving more complex and difficult problems rather than demonstrating the accuracy of their current problems which can lead to a decrease in the quality of their simulations. Previous works on verification and validation in the CFD community [65][66][67][68] define verification as demonstrating the mathematical correctness of the numerical simulation. This usually means that if the observed discretization error decreases to zero as the mesh increments decrease to zero, then the equations are “solved correctly”. In other words, code verification is a procedure to demonstrate that the governing equations, as implemented in the code, are solved correctly.

Verification of CFD codes has been the subject of many studies in recent years. Abanto et al. [68] demonstrated an approach to test the accuracy of some of the most widespread commercial codes. They presented grid convergence studies on atypical CFD cases using some commercial CFD packages. Their verification test cases include an incompressible laminar Poiseuille flow, a manufactured incompressible laminar boundary layer flow, an incompressible re-circulating flow and an incompressible annular flow. Different types of structured and unstructured meshes were used during the study. They observed non-monotonic grid convergence for all their test cases. Iterative convergence of the discrete equations to machine zero did not guaranty accurate flow field predications which meant that the codes converged to wrong solutions. From their study,

they recommended that users perform the verification of commercial CFD codes and be cautious when using the commercial codes on industrial problems.

Kleb and Wood [69] pointed out that the computational simulation community is not routinely publishing independently verifiable tests to accompany new models or algorithms. They mentioned the importance of conducting component-level verification tests before attempting system-level verification and also publishing them when introducing a new component algorithm. They proposed a protocol for the introduction of new methods and physical models that would provide the computational community with a credible history of documented, repeatable verification tests that would enable independent replication.

Roache [65] [66] discussed the verification of codes and calculations along with some definitions and descriptions related to confidence building in computational fluid dynamics. Verification was described as solving the equations right and validation as solving the right equations. Different aspects discussed in the paper include the distinction between code verification and validation, grid convergence and iterative convergence, truncation error and discretization error. Also discussed were verification of calculations, error taxonomies, code verification via systematic grid convergence testing, the Grid Convergence Index (GCI) and sensitivity of grid convergence testing. According to the author, verification does not include all aspects of code quality assurance like the important concerns of version control or archiving of input data. In the book by Roache et al [65], the authors comprehensively discussed code verification, the Method of Manufactured Solutions (MMS) used to obtain exact solutions for code verification purposes, and order of accuracy verification. A more recent study of code verification

conducted by Shunn et al [70] demonstrates the MMS verification technique as applied to variable density solvers. In this study, verification was used to investigate the effects of tabulated state-equations and temporal iteration errors on the convergence and accuracy of the code. The two problems constructed were diffusive mixing of species, and convection of density fronts which reflect basic physical phenomena found in combustion problems. The grid refinement studies that were performed confirm that the spatial convergence rate of the solver to be second order when an analytical equation of state (EOS) is used. Convergence of the flow variables to the exact solution were found to be impaired when the EOS was linearly interpolated in space. It was also found that EOS interpolation errors introduce spurious numerical fluctuations in the flow variables, with velocity and pressure being particularly vulnerable. This particular variable density algorithm showed first order temporal evolution of the flow when a single outer density iteration was applied. Temporal errors were generally not dominant when multiple outer density iterations were performed, making it difficult to confirm the temporal accuracy of the method with multiple outer iterations.

3.1 Verification procedure

The intent of this chapter is to present a suitable verification framework that can be applied to our own in-house solver, LES-BLAC. The procedure can be used to provide a pass-fail acceptance criterion commonly used in the community to establish the validity of CFD solvers [70]. This same procedure is found to be very helpful in detecting coding mistakes (bugs) that are associated with spatial or temporal discretization of the transport equations. The need for verification in this project arises due to the introduction of

numerical schemes and models to account for variable density low Mach number physics. Numerical schemes and model developments were presented in Chapter 2.

Currently, our verification procedure consists of comparing our computational solution to an exact analytical solution representative of the physics involved in low-mach number problems. Comparing to an exact solution is called MES, or method of exact solutions, and is a powerful verification technique when one can develop an analytical solution for a test case. Comparing to an exact solution brings up the notion of discretization errors which are inherent to any solver that discretizes a set of governing PDEs into a finite dimensional subspace which approximates the continuum solution. The difference between the two is the discretization error. Discretization methods are *consistent* if the error goes to zero as the representative cell size, h , decreases to zero (for mesh size h , then a consistent method will result in error that is proportional to h^p). The rate at which the error decreases to zero is called the order of accuracy. A discretization method is said to be second order accurate in space if the discretization error goes to zero as h^2 . According to the community the most rigorous acceptance criterion is verification of order of accuracy, in which one not only seeks to verify that the method is consistent, but also establishes the value of p and is then compared to the theoretical order of the discretization method. This is our established procedure.

The following sections present spatial and temporal order of accuracy test cases that have been developed with variable density transport equations in mind. The first part presents cases related to the spatial and temporal order of accuracy where we seek to establish the second order accuracy of our discretization and integration scheme through a one dimensional isothermal binary mixing case where large density ratios are present. We

then present a second spatial accuracy test for a laminar channel flow with variable property heat transfer, where this configuration corresponds to a canonical test case representative of many wall-bounded flows of interest. Lastly, a classical test case corresponding to momentum driven laminar boundary layers with and without heat transfer is presented. Streamwise velocity, temperature and near wall property comparisons are made with the analytical Blasius similarity solutions. It is shown that the use of our numerical schemes and boundary conditions resolve the boundary and all of its properties very well yielding excellent agreement.

3.2 One-Dimensional Case Study: Order of Accuracy Analysis

3.2.1 Isothermal Binary Mixing

The following verification case tests the ability of the solver to handle flows with large density ratios similar to those found in fires or in combustion systems. An exact solution to the one dimensional mixing of two fluids with different molecular weights is presented. The mixing occurs at constant temperature and pressure conditions. The configuration corresponds to a stratified fluid with a layer of light fluid near a solid wall mixing with a heavier fluid in the ambient. Note that the configuration has zero gravity and is one-dimensional; it is depicted in Figure 6. The computational domain is assumed to be very large in width and depth consistent with using periodic conditions in streamwise and spanwise directions. The restriction of no-slip boundary flow is imposed at the wall while also specifying vanishing gradient conditions for total enthalpy and mixture fraction at the same location. The configuration is presented,

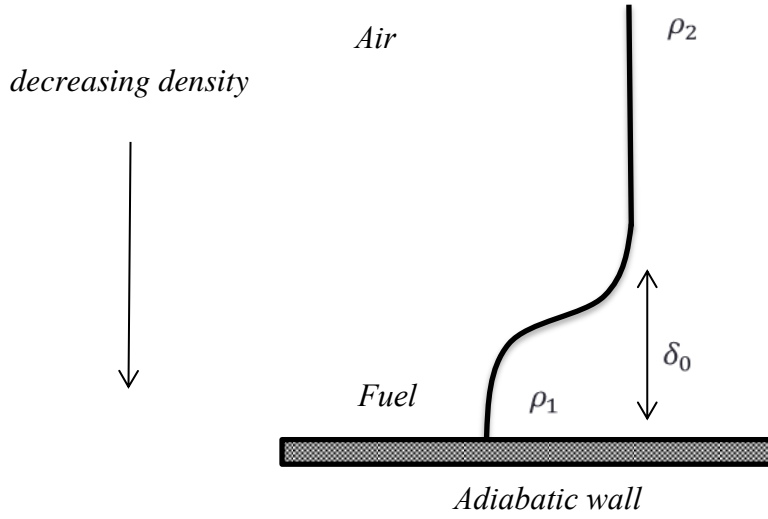


Figure 6. Schematic of the one-dimensional mixing problem. As depicted in the figure, the problem is set up such that a thin layer of light fluid (i.e., fuel) mixes with a heavier column of fluid (i.e., air) due to molecular diffusion.

3.2.2 Analytical Solution

An exact solution for the binary mixing problem is found for the mass density field which directly couples the mixture fraction and velocity. The solution has the characteristic of being a transient mass density diffusion equation satisfying, $\frac{\partial \rho}{\partial t} = D \frac{\partial^2 \rho}{\partial y^2}$.

The mass density field solution has the following form:

$$\rho(y, t) = \rho_2 + (\rho_1 - \rho_2) \frac{\delta_0}{\sqrt{4\pi D(t + t_0)}} e^{\frac{-y^2}{4D(t+t_0)}} \quad (1)$$

where the reference value of densities ρ_1 and ρ_2 are calculated through use of a thermodynamic equation of state (EOS) by using the molecular weights of heavy and light fluids (MW_1, MW_2) The characteristic initial mixing length-scale is denoted by δ_0 .

The mixture fraction field is now defined as,

$$Z(y, t) = \frac{\frac{1}{\rho(y, t)} - \frac{1}{\rho_2}}{\frac{1}{\rho_1} - \frac{1}{\rho_2}} \quad (2)$$

Using the one-dimensional continuity equation gives the wall-normal component of velocity as,

$$v(y, t) = \frac{(\rho_1 - \rho_2)}{\rho(y, t)} \frac{\delta_0}{\sqrt{4\pi D(t + t_0)}} \left(\frac{y}{2(t + t_0)} \right) e^{\frac{-y^2}{4D(t+t_0)}} \quad (3)$$

It should be noted that all the above expressions have a singularity at time ($t = 0$), thus an offset time, t_0 , is added based on diffusion time scales to avoid the singularity. The analysis of this problem begins at $t_0=10$. Also note that the reference density fields corresponding to isothermal light and heavy fluid mixing in air (ρ_1, ρ_2) are defined through the use of the equation of state (Table 1). The species fraction of oxygen and nitrogen in air are: $Y_{O_{2air}} = 0.233$ and $Y_{N_{2air}} = 1 - Y_{O_{2air}}$, they are used calculate the molecular weight of the mixture composition,

$$\rho_2 = \rho_{air} \text{ and } MW_2 = MW_{air}$$

$$\rho_1 = \rho_2 \frac{MW_1}{MW_{air}}$$

The verification task begins by initializing the code with the above equations at an offset time, $t_0=10$. The domain is selected as $(Lx, Ly, Lz) = (10, 30, 5)$ with periodic conditions in x and z . Grid design procedures are followed in order to resolve the characteristic mixing layer which has a minimum length-scale of 2 cm and increases to 20 cm by the end of the simulation. Adequate resolution will ensure to have at least 30-40 points inside

the mixing layer thickness set by the initial conditions. The running time is selected based on an analysis of the time evolution of the minimum value of mass density (Figure 7) which shows that the peak mass density decreases exponentially to nearly 1 at an approximate time of 400 time units.

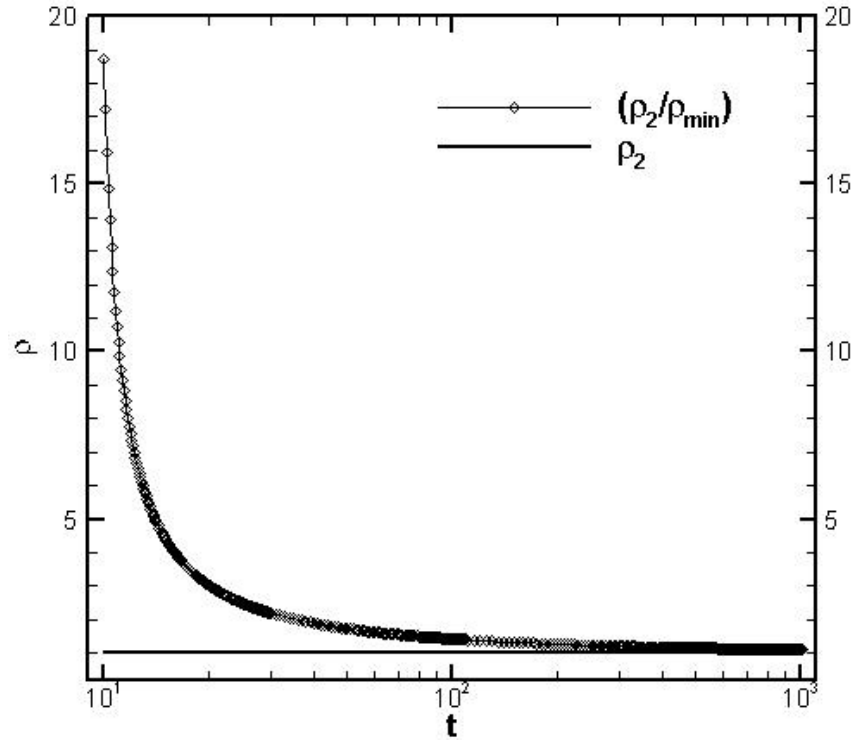


Figure 7. Temporal variations of peak mass-density ratio (ratio of light over heavier fluid) in the system, compared to the freestream mass-density.

Re_{ref}	Pr	ρ_1^*	ρ_2^*
50	0.75	$\rho_{air} \frac{MW_1}{MW_{air}}$ = 0.0097	$\rho_{air} = 1$
v_{ref}	δ_0 (characteristic lengthscale)	ν	$T_{ref}(K)$
$5 \frac{cm}{s}$	2 cm	$2 \times 10^{-5} \frac{m^2}{s}$	300

Table 1. Physical parameter table for 1-dimensional mixing problem.

$(L_x L_y L_z)^*$	$(n_x n_y n_z)$	grid stretching
(10,30,5)	(10,1200,4) $\Delta y = 0.025$	Uniform grid x, z, y
Initial Conditions	Specific Enthalpy model	Farfield boundary
$\mathbf{u}_{init} = \mathbf{0}, \mathbf{w}_{init} = \mathbf{0}$	Chemkin coefficient data base	$u_{farfield} = 0$
$\mathbf{v}_{init} = \mathbf{v}_{exact}(\mathbf{t} = \mathbf{t}_0)$	w/ enthalpy polynomial:	$\frac{dv}{dy} = 0, \frac{dw}{dy} = 0$
$\mathbf{Z}_{init} = \mathbf{Z}_{exact}(\mathbf{t} = \mathbf{t}_0)$	$h^* = a_6 + a_1 T + \frac{c_2 T^2}{2} + \frac{c_3 T^3}{3}$	$\frac{dh}{dy} = 0, \frac{dZ}{dy} = 0$
$\mathbf{h}_{init} = \mathbf{h}^*(\mathbf{Z}_{init}, T_{inf})$	$+ \frac{c_4 T^4}{4} + \frac{c_5 T^5}{5}$	
wall boundary	Scalar Discretization Optic	Periodicity
$\mathbf{u} = \mathbf{v} = \mathbf{w} = \mathbf{0}$	QUICK	Spanwise, Streamwise
$T_{wall} = T_{inf}$		

Table 2. Computational parameter table for 1-dimensional mixing problem. The table presents initial conditions, boundary conditions, and thermodynamic models.

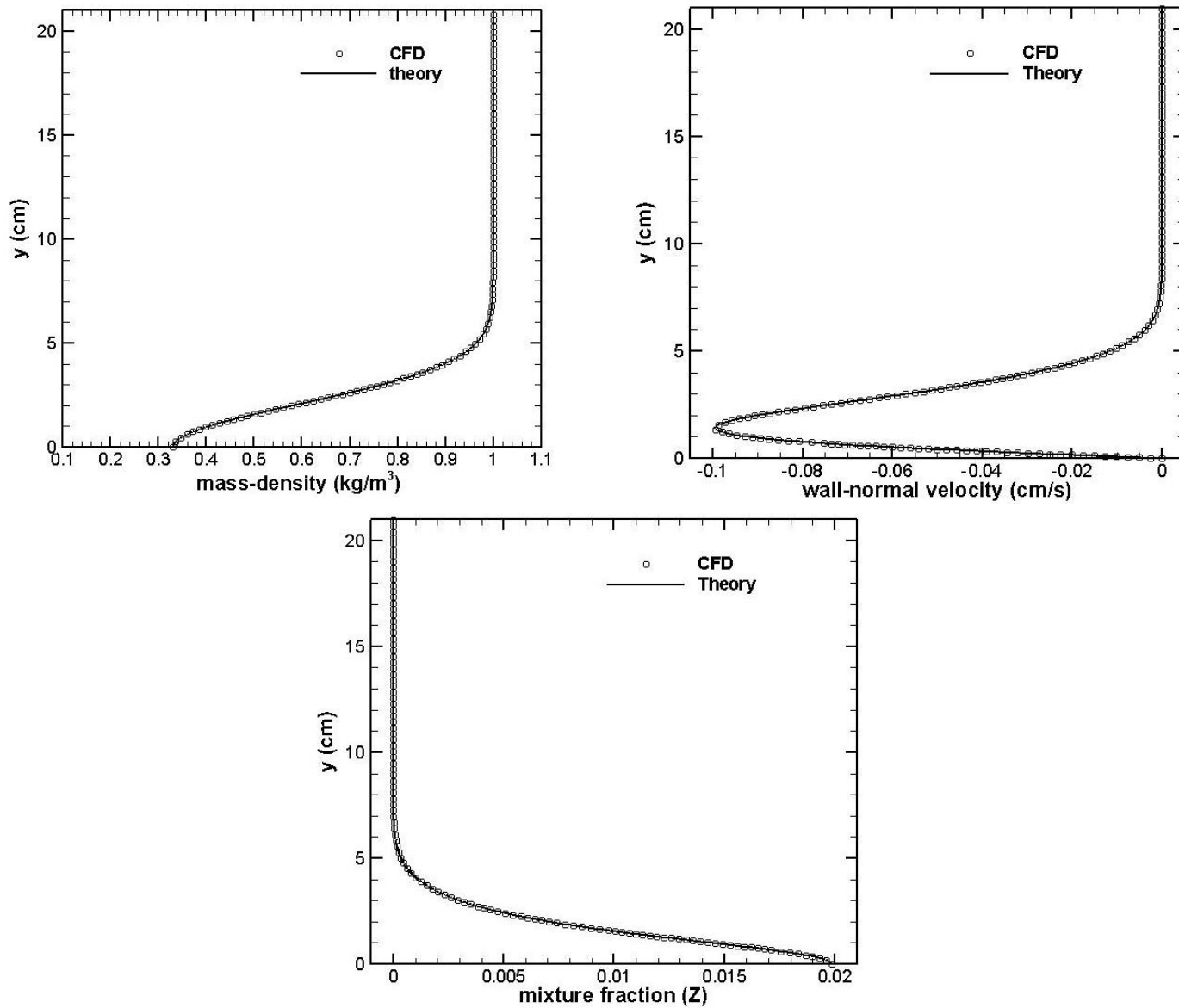


Figure 8. Comparison of 1-dimensional mixing problem between numerical solution obtained with LES-BLAC and analytical model (Solid line represents the theoretical solution); comparisons are made for: mass density, wall-normal velocity, and mixture fraction at twenty time units .

This case study was setup with the physical parameters presented in Table 1, which specify the reference Reynolds number, $Re = 50$, initial mass density values, characteristic length ($\delta_o = 2 \text{ cm}$) and velocity scales ($v_{ref} = 5 \frac{\text{cm}}{\text{s}}$) are also presented. The length and velocity scales are selected based on the mixing length thickness at the initial time ($t_o = 10$) and the magnitude of the bulk value of wall normal velocity respectively. The computational configuration, including domain size and resolution are presented specifying the wall-normal grid-spacing value of $\Delta y = 0.025$. Initial conditions are prescribed from the analytical solution at a prescribed offset time while also enforcing the boundary conditions. Figure 8 shows instantaneous profiles of mass density, y-velocity and mixture fraction at a time of $t = 20$. As was stated earlier, this problem corresponds to isothermal mixing between two fluids of different molecular weights. This can be observed from the mass density profile in Figure 8a showing a clear density mixing layer. The negative y-velocity component indicates the direction of the fluid motion and has maximum values at locations with peak density gradients. All profiles presented in Figure 8 compare very well to the analytical solution.

Figure 9a shows a spatial order of accuracy analysis for profiles of mass density, y-velocity and mixture fraction. The analysis is performed by choosing a fixed time step of $dt = 10^{-3}$ and refining the grid in the y-direction. Note that the time step, dt , has to be small enough to provide an analysis that is not contaminated by temporal discretization errors. The number of points used in the refinement studies are: $n_j = 75, 150, 300, 600, 1200$ and the global $||L_2||$ error, $L_2 = \sqrt{\frac{1}{N} \sum_{j=1}^N (u_j - U_j)^2}$, is used to show the observed order of accuracy of the finite differencing scheme (where u_j

is the exact solution and U_j is the discrete solution and N is the number of grid points). As indicated by Figure 9 the second-order accuracy of the code is retrieved in the presence of flows with strong density gradients. Similarly, Figure 9b shows results from the temporal order of accuracy analysis making refinements with the simulation time step while maintaining the computational grid constant ($\Delta y = 2 \times 10^{-3}$, with $dt = 0.025, 0.05, 0.10, 0.20, 0.40, 0.80$). Since the global solution will be dominated by errors both in space and time, only a finely resolved grid will help hinder the spatial errors allowing analysis of the temporal errors.

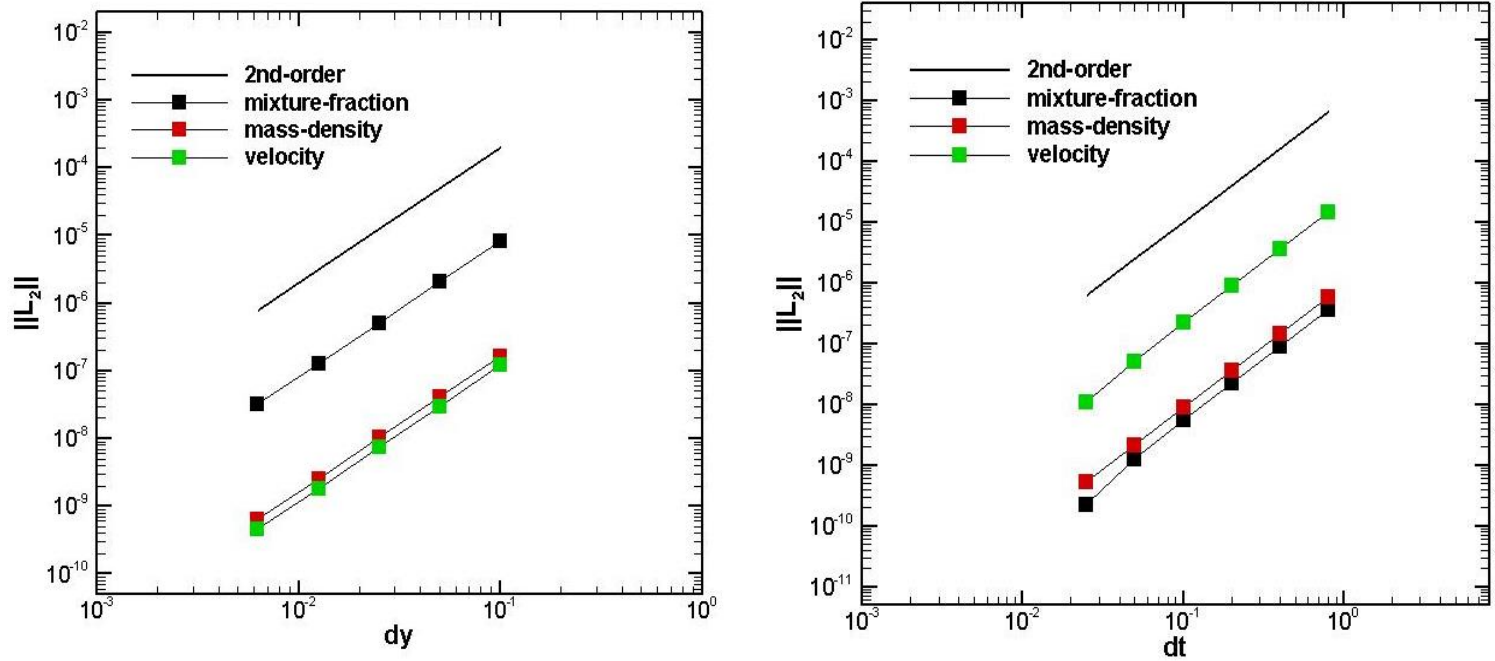


Figure 9. Order of accuracy analysis for mixing variables: mixture fraction, mass density and velocity (a) grid refinements demonstrate the second order accuracy of the spatial scheme (b) time-step refinements demonstrate the 2nd order accuracy of the time integration scheme.

3.3 Two-Dimensional Case Study: Order of Accuracy Analysis

3.3.1 Poiseuille Flow with heat transfer

Laminar flow in a planar channel with heat transfer is studied due to its canonical nature in relation to many engineering flows. Introducing simplifications in the theoretical formulation allows us to obtain an analytical solution for the case where mass density is not constant. This enables us to use this problem for code verification purposes in a two dimensional framework. The analytical solution is then implemented in our CFD model by prescribing a periodic boundary condition in the streamwise direction while adjusting the pressure gradient to keep the mass flux in the channel constant. The heat transfer is prescribed by specifying isothermal wall boundaries where the upper wall is selected as the hot boundary (900K) and the lower is kept at an ambient temperature (300K), $T_2 > T_1$; Figure 10. The Reynolds number ($Re = 50$) is defined based on the channel half-height $\delta = 1 \text{ cm}$, a streamwise velocity of $u_{ref} = 10 \frac{\text{cm}}{\text{s}}$, and a reference viscosity $\mu_{ref} = 2 * 10^{-5} \frac{\text{kg}}{\text{m-s}}$. The steady state analytical solution for the streamwise velocity and enthalpy are presented as follows:

$$u(y) = \frac{2}{3} \left(-\frac{dp}{dx} \right) \left(\frac{1}{\mu_1} + \frac{2}{\mu_2} \right) y \frac{\left(\frac{1}{\mu_1} + \left(\frac{1}{\mu_2} - \frac{1}{\mu_1} \right) \frac{y}{4} \right)}{\left(\frac{1}{\mu_1} + \frac{1}{\mu_2} \right)} - \left(-\frac{dp}{dx} \right) y^2 \left(\frac{1/2}{\mu_1} + \left(\frac{1}{\mu_2} - \frac{1}{\mu_1} \right) \frac{y}{6} \right) \quad (4)$$

and

$$h(y) = h_{w1} + (h_{w2} - h_{w1}) y \times \frac{\left(\frac{1}{\mu_1} + \left(\frac{1}{\mu_2} - \frac{1}{\mu_1} \right) \frac{y}{4} \right)}{\left(\frac{1}{\mu_1} + \frac{1}{\mu_2} \right)} \quad (5)$$

Defining the reference viscosity at the boundaries as,

$$\mu_1 = 1/Re ; \mu_2 = 5/Re$$

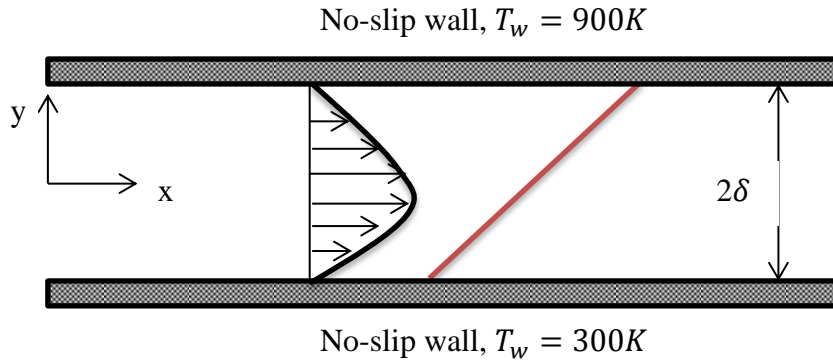


Figure 10. Schematic of weakly compressible Poiseuille type canonical flow with heat-transfer. Heating is introduced through a hot isothermal wall on top at 900K.

$(L_x L_y L_z)^*$	$(n_x n_y n_z)$	<i>grid stretching</i>
(4 cm, 2 cm, 2 cm)	(8,320,4) $\Delta y = 0.00625 \text{ cm}$	Uniform grid in x, z, y
Initial Conditions	Specific Enthalpy model	Wall boundaries
$\mathbf{u}_{init} = 1, \mathbf{v}_{init} = 0$	Chemkin coefficient data base w/ enthalpy polynomial: $h^* = a_6 + a_1 T + \frac{c_2 T^2}{2} + \frac{c_3 T^3}{3} + \frac{c_4 T^4}{4} + \frac{c_5 T^5}{5}$	$u = v = w = 0$
$\mathbf{Z}_{init} = \mathbf{Z}_{exact}(t = t_0)$		$h_1 = \frac{his(z = 0, 300l)}{h_{ref}}$
$\mathbf{h}_{init} = \mathbf{h}^*(\mathbf{Z} = \mathbf{0}, T_{inf}) / h_{ref}$		$h_2 = \frac{his(z = 0, 900l)}{h_{ref}}$
<i>viscosity</i>	<i>Scalar Discretization Option</i>	<i>Periodicity</i>
$\mu_1 = 1/Re$	QUICK	Spanwise, Streamwise
$\mu_2 = 5/Re$		

Table 3. Computational parameter table for Poiseuille flow with heat-transfer.

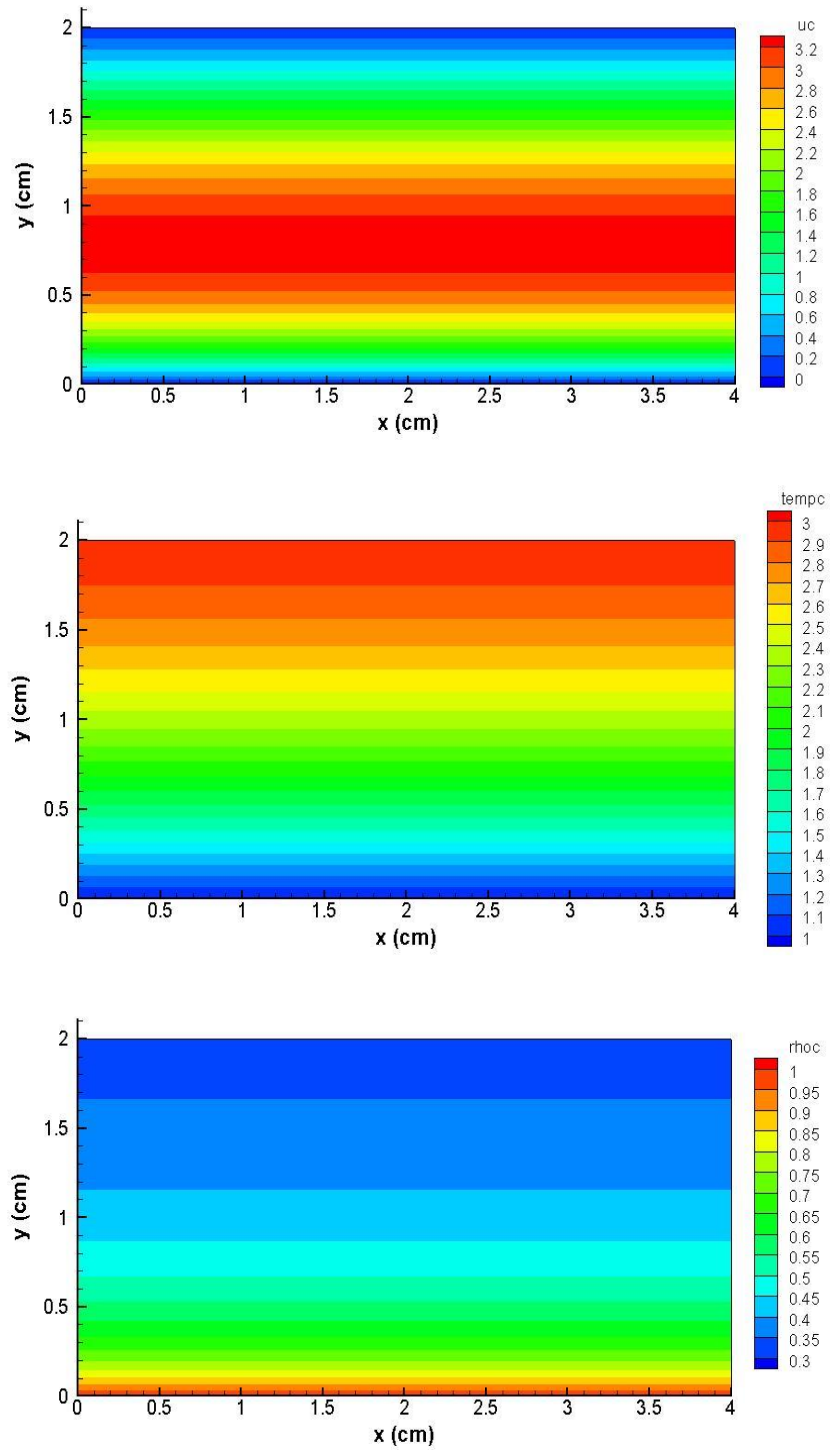


Figure 11. Iso-contours of flow variables: streamwise velocity, temperature, and mass-density for Poiseuille flow with heat transfer.

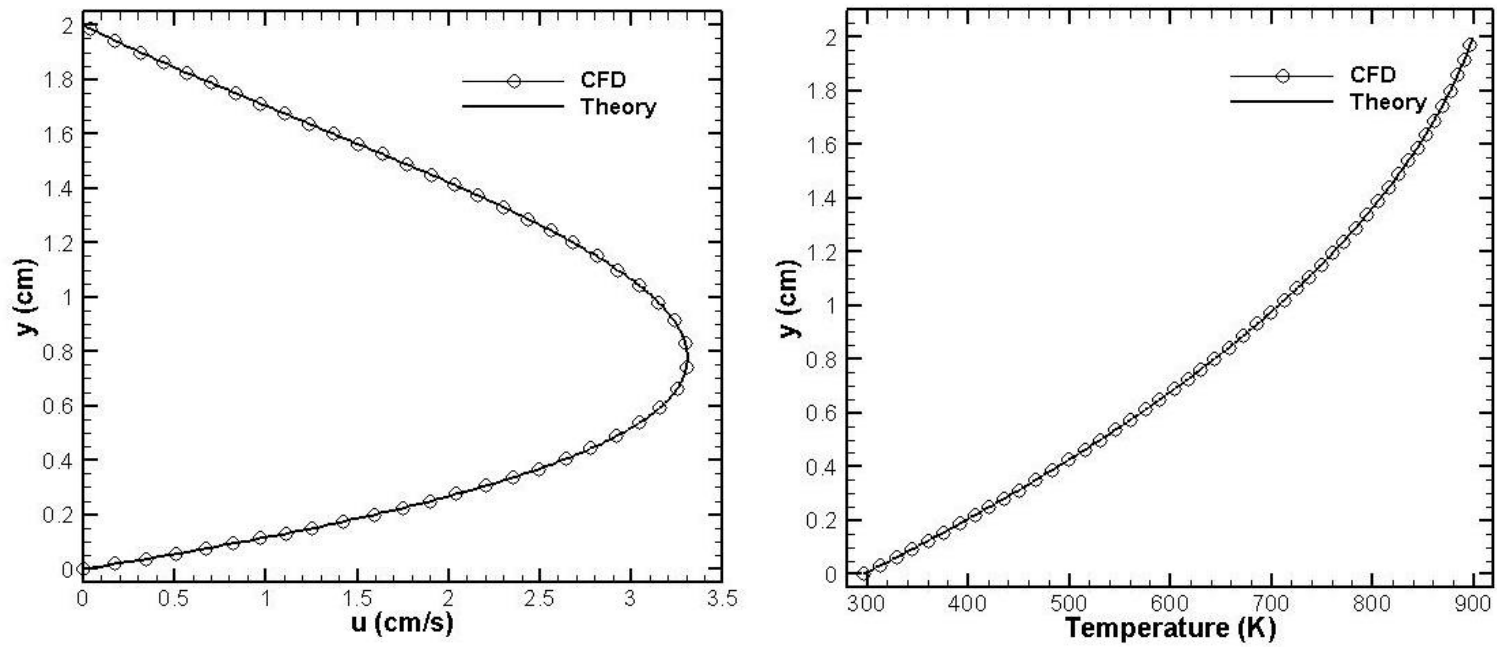


Figure 12. Profiles of streamwise velocity and temperature (Kelvin) for Poiseuille flow with heat transfer. Comparison is made with the analytical solution.

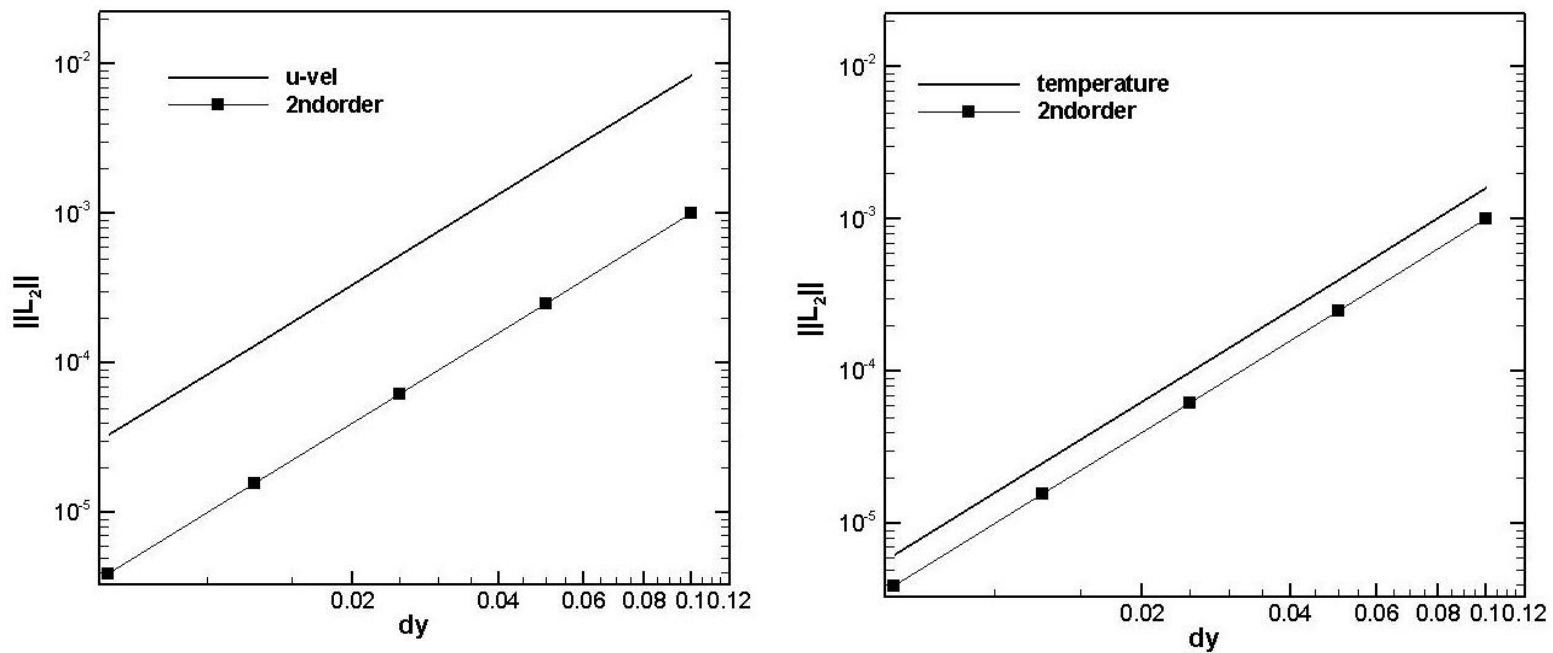


Figure 13. Order of accuracy analysis for Poiseuille channel flow variables: streamwise velocity and temperature: grid refinements demonstrate the second order accuracy of the spatial scheme.

3.4 Classical Boundary Layer Flow

3.4.1 Blasius Flow

We now focus on modeling a Blasius boundary layer flow configuration with and without heat transfer. Physically this is an important test case since it captures some of the salient features (i.e, wall shear stress, heat flux) found in momentum-driven boundary layers. Numerically this is also a challenging flow since it requires the implementation of inflow and outflow conditions to capture the spatially developing nature of the problem. The parameters necessary to implement this run are presented in Table 1 and results are shown for representative cases. The physical parameters for the Blasius test case are presented in Table 4. The Reynolds number is the critical non-dimensional number controlling the physical properties and state of the flow. It is defined with a displacement thickness, $\delta^* = \int_0^\delta \left(1 - \frac{\rho u}{\rho u_{inf}}\right) dy = 1 \text{ cm}$, as the reference length-scale and a free-stream velocity of $u_\infty = 10 \frac{\text{cm}}{\text{s}}$ as the velocity-scale so that the Reynolds number can be defined as $Re = \frac{\delta u_{ref}}{\nu}$. The Prandtl number is specified according to its reference value in air. The simulation is performed on a computational domain of $(Lx, Ly, Lz) = (200 \text{ cm}, 60 \text{ cm}, 5 \text{ cm})$ with the first off-wall grid point located at $\Delta y_{min} = 0.028 \text{ cm}$ and the spacing of the outer points scaling with the boundary layer thickness, $\Delta y_{max} = 1.73 \text{ cm}$, such that $\Delta x \sim \Delta y_{max}$ (The total number of grid cells is 50,000). Standard grid design procedures are followed ensuring that 30-40 points are used to resolve the boundary layer viscous region. This is achieved through grid stretching by means of a hyperbolic tangent function which clusters the grid nodes near the wall. This capability allows us to be more efficient in resolving the boundary layer thickness, δ .

Re	Re_x	$Pr = c_p\mu/k$	T_{wall}, T_{inf}
50	842-10,000	0.71	450, 300K
$L_0 - L_z$	Reference values	$\delta^*(x = L_0)$	$\delta(x = L_0)$
16.84 - 200 cm	$u_{ref} = 10 \text{ cm/s}$ $L_{ref} = 1 \text{ cm}$ $v_{ref} = 2 \times 10^{-5} \text{ m}^2/\text{s}$	1 cm	3 cm

Table 4. Physical parameter table for Blasius boundary layer flow.

$(L_x L_y L_z)^*$	$(n_x n_y n_z)$	<i>grid stretching</i>	
(200,60,4)cm	(128,96,4) $\Delta y_{min} = 0.028 \text{ cm}$ $\Delta y_{max} = 1.73 \text{ cm}$	Wall –normal hyperbolic ($\alpha = 2.75$) Uniform grid x, z	
<i>Inflow boundary</i>	<i>outflow boundary</i>	<i>freestream boundary</i>	
$\mathbf{u} = \mathbf{u}_{blasius},$ $\mathbf{v} = \mathbf{v}_{blasius},$ $\mathbf{w} = \mathbf{0}$ $T = T_{wall}$	<i>Orlansky</i> [64] $\frac{\partial \rho u_i}{\partial t} + U_c \frac{\partial \rho u_i}{\partial x_i} = 0$ $\frac{\partial \rho h}{\partial t} + U_c \frac{\partial \rho h}{\partial x_i} = 0$	$\frac{du}{dy} = 0$ $\frac{dv}{dy} = 0$ $\frac{dw}{dy} = 0$ $\frac{dh}{dy} = 0$	(Option) $\frac{du}{dy} = 0, \frac{dw}{dy}$ $= 0$ $v = v_{blasius}$ $\frac{dh}{dy} = 0$
<i>wall boundary</i>	<i>Specific Enthalpy Model</i>	<i>Heat Capacity Model</i>	
$\mathbf{u} = \mathbf{v} = \mathbf{w} = \mathbf{0}$ $T_{wall} = 450K$	CHEMKIN coefficient data base for enthalpy polynomial: $h^* = a_6 + a_1 T + \frac{c_2 T^2}{2} + \frac{c_3 T^3}{3} + \frac{c_4 T^4}{4} + \frac{c_5 T^5}{5}$	CHEMKIN coefficient data base for heat capacity polynomial: $c_p^* = c_1 + c_2 T + c_3 T^2 + c_4 T^3 + c_5 T^4$	

Table 5. Computational parameter table for Blasius boundary layer flow with heat transfer. The table presents initial conditions, boundary conditions, and thermodynamic models.

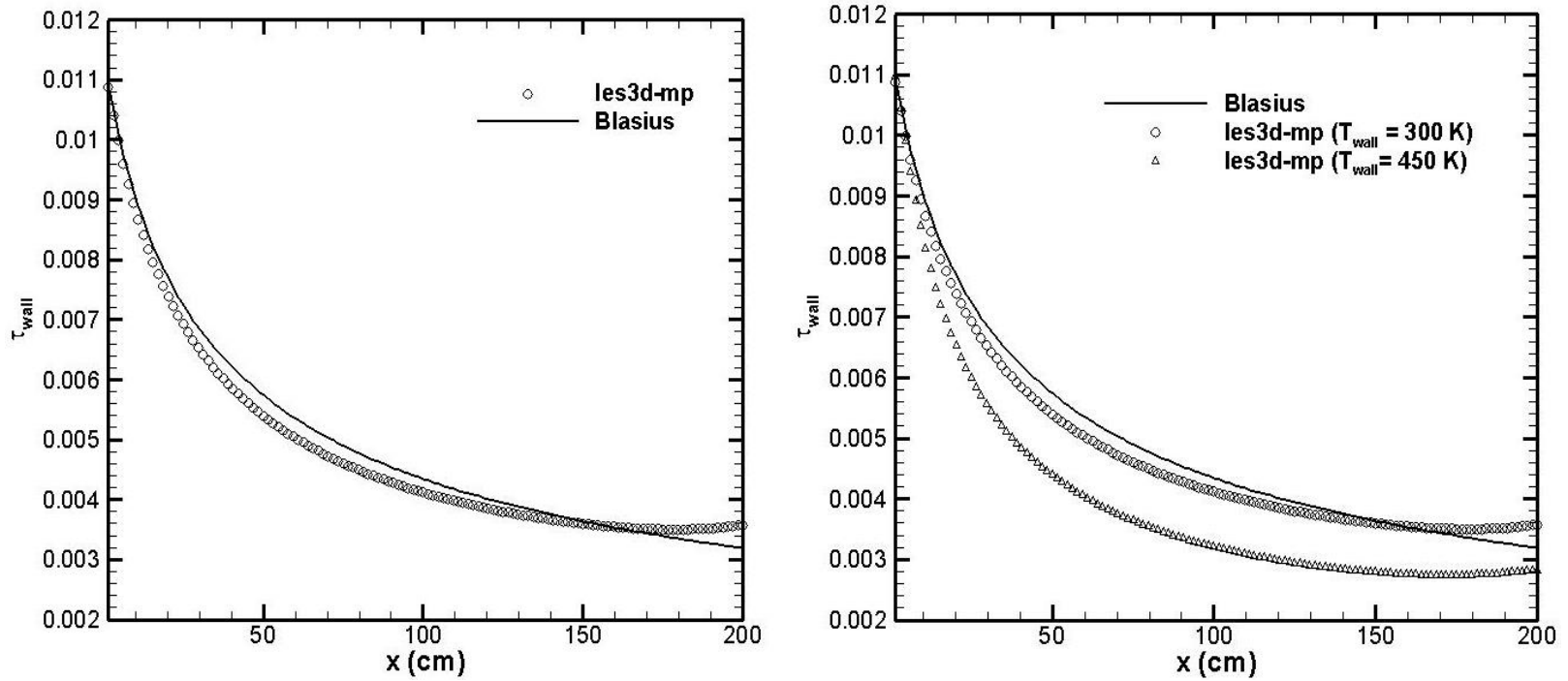


Figure 14. Spatial variations of wall-shear stress profiles for Blasius boundary layer type flow; comparison to analytical solution and demonstration of the effect of the wall-heating on the shear-stress distribution.

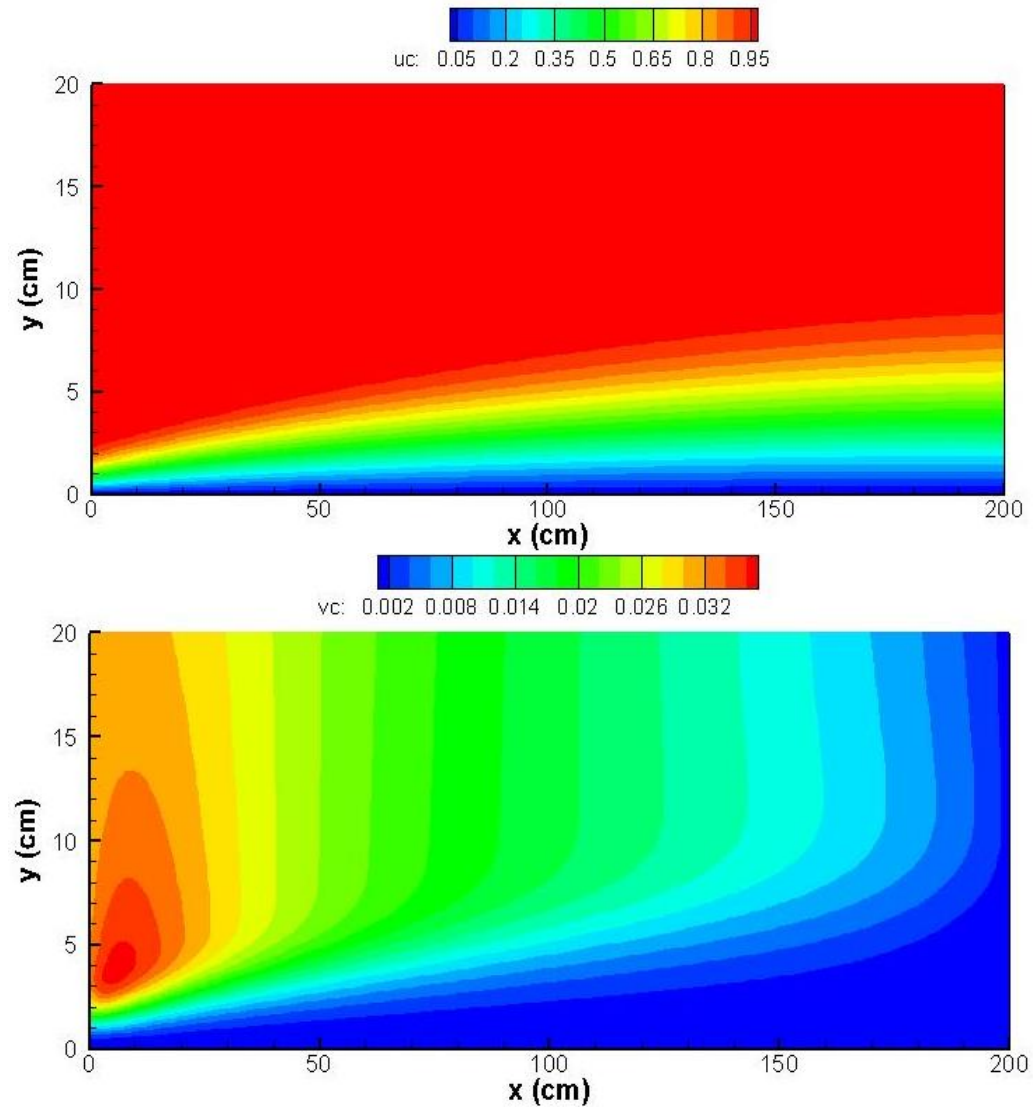


Figure 15. Iso-contours of streamwise and wall-normal velocity in Blasius boundary layer type flow with an isothermal heated wall at $T_{wall} = 450K$.

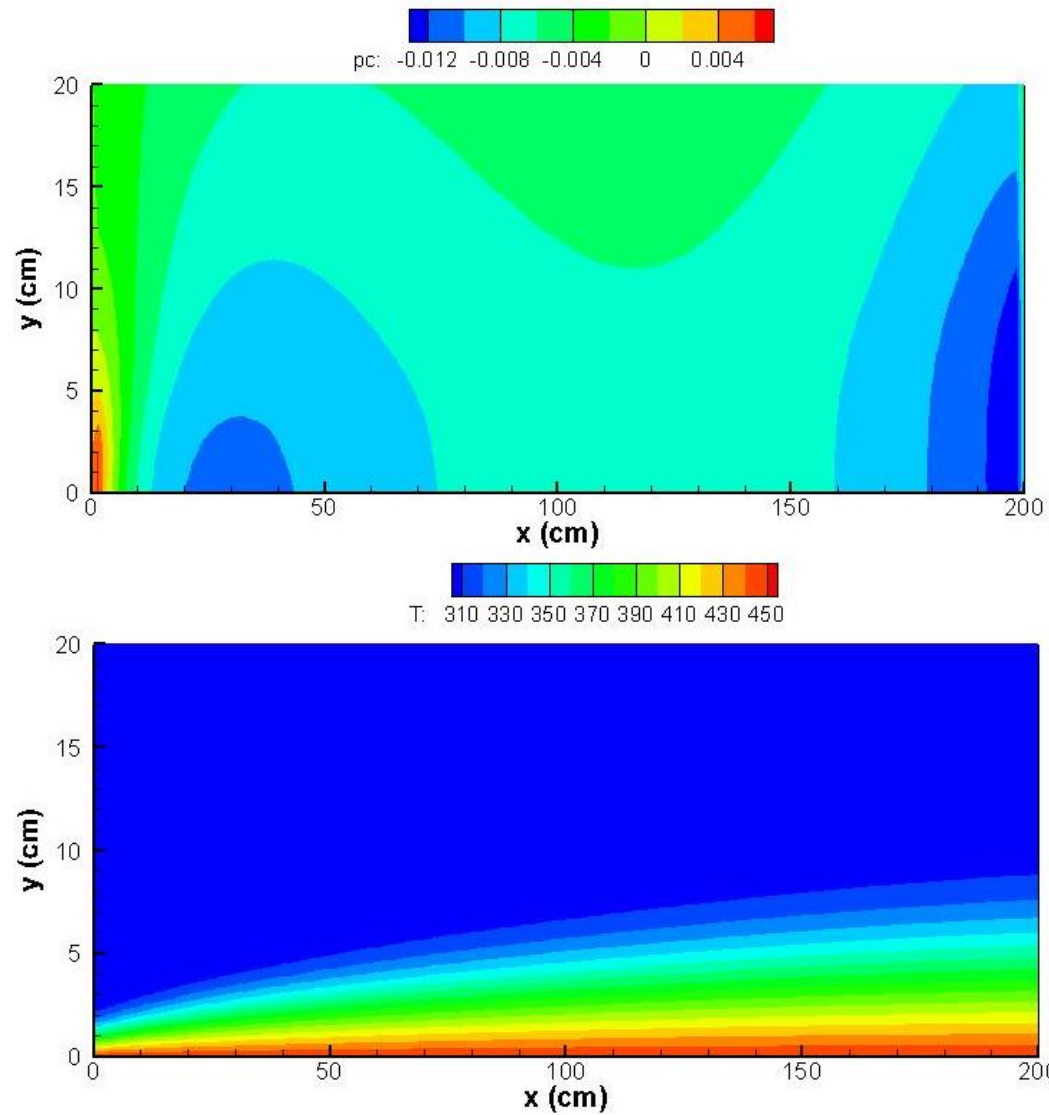


Figure 16. Iso-contours of pressure and temperature in Blasius boundary layer type flow with an isothermal heated wall at $T_{wall} = 450K$.

The specification of the inflow profile for the constant density boundary layer case is specified through the use of a Blasius profile as is shown in Table 5. Blasius u and v velocity profiles to be used as inflow conditions can be prescribed by specifying the reference viscosity ν and the displacement thickness δ^* into a simple auxiliary program that is called inside the inflow module. A more elaborate inflow condition is specified for the case with heat transfer. This makes use of the similarities between the momentum and total enthalpy transport equation in Blasius type flows where the effect of pressure gradient is negligible, $\frac{dP}{dx} \sim 0$. Using this concept one can write the following description for the enthalpy inflow condition as $h^* = u^*(h_{inf}^* - h_{wall}^*) + h_{wall}^*$ where the values for enthalpy at the free-stream and at the wall are defined using the corresponding temperature (and mixture fraction, $Z = 0$, for air cases).

Figure 14 shows the spatial evolution of the wall-shear stress. The left figure shows good agreement of the wall shear stress with the Blasius exact solution. Comparisons of the wall-shear stress to the analytical expressions have to account for distance from the leading edge distance which is a virtual origin and is not shown in the computational domain and is implicitly defined in the inflow profiles. Thus, the reconstruction of the wall-shear stress profiles are calculated through the modified analytical expressions, $\tau_{wall} = \frac{0.332}{\sqrt{\left(Re_x + \left(\frac{0.332}{\tau_{wall_0}}\right)^2\right)}}$ where the inflow Reynolds number

contribution is accounted for by the expression, $Re_x = \left(\frac{0.332}{\tau_{wall_0}}\right)^2$ (and the leading edge distance is, $x_0 = \frac{\nu}{u_{ref}} \left(\frac{0.332}{\tau_{wall_0}}\right)^2$). An additional figure is shown in Figure 9 corresponding

to a case with heat transfer. The effect of heat transfer is seen to reduce the magnitude of the wall velocity gradients, this in turn decreases the wall-shear stress.

Figure 15 shows contours of streamwise and wall-normal velocity for the case with heat transfer at a wall temperature of $T_{wall} = 450K$. As is typically observed for momentum driven flows the growth of the boundary layer scales like $\delta \sim x/\sqrt{Re_x}$ (or $\delta \sim x^{\frac{1}{2}}$). This behavior can be directly observed from the velocity and temperature profiles as the Re_x increases (or distance along the plate). Figure 16 shows temperature and pressure contours in the flow. Although not severely adverse, errors associated with the approximate boundary conditions at the outflow can be seen through the magnitude of the y-velocity at that location (to obtain a better result the outflow boundary should include wall-normal diffusion terms which are inherent to Blasius-type flows). At the inflow an incorrect initial region with peak y-velocity magnitudes arises due to the approximate specification of a Blasius profile, which is restricted to a constant density framework. Similar to the observations made for the y-velocity plot, the pressure contours show peak disturbances near the inflow and the outflow. Aside from the pressure disturbances, the pressure variations remain bounded at two to three orders of magnitudes lower than $\rho_{\infty} u_{\infty}^2 \sim 1$; $\Delta p \ll \rho_{\infty} u_{\infty}^2$ demonstrating the good quality of the solution.

3.5 *Summary*

This chapter presents fundamental studies of the order of accuracy of our in-house solver, les3d-mp. It includes a suite of verification tests that is essential to code developers in retrieving errors and establishing confidence in the code. The configurations presented are (i) wall-bounded isothermal mixing layer case and (ii) laminar planar channel flow with heat transfer and variable properties. The former case challenges the solver by introducing strong mass density variations in a binary mixture of light and heavy fluids for a decaying mixing layer; both spatial and temporal analysis successfully demonstrate the 2nd order accuracy of the schemes. The laminar planar channel case with heat transfer is also studied to present a configuration similar to the capabilities of the solver, that is, momentum driven wall bounded flows with heat transfer. Computing the errors with respect to streamwise velocity and temperature variations clearly revealed the second order accuracy of the spatial scheme. Lastly, classical momentum driven laminar boundary layer flows have been computed and compared to the semi-analytical Blasius solution. The results show good development of the flow variables, wall shear stress and good control of the pressure field, revealing a correct implementation of the numerical methods and also of the boundary conditions.

Chapter 4: Validation

The simulation of turbulent wall-bounded flows is a major challenge for any CFD code. The validation of this problem using experimental or DNS as benchmarks is an important step in determining the ability of the turbulence model to handle this type of flow. Large-eddy simulations of two canonical channel test cases, and a momentum driven boundary layer test case are presented in this chapter for validation purposes. In the channel cases presented, high-fidelity turbulent DNS results are used as the “gold” standard for measuring the accuracy of our models. DNS is recognized in the community as providing the highest level of turbulent description due to its model-free approach and resolution of the entire spectrum of scales of motion. Thus, DNS is a reliable computational tool which complements the time trusted methodology of experimental research. Turbulence modeling is applied using implicit grid filtering, dynamic Smagorinsky LES (described in detail in Chapter 2) for momentum and scalar transfer.

The first test case corresponds to the classical incompressible turbulent channel configuration. This flow corresponds to a planar, fully developed flow where turbulence develops and sustains itself to form wall-bounded turbulent structures. This configuration has been studied by various researchers for fundamental turbulent validation studies, visualization and modeling purposes and results are compared to the Kim, Moin and Moser test case [71]. The second test case corresponds to a similar configuration but with the new complexity of strong temperature gradients at the wall. This adds to the richness of the turbulent physics since it brings in non-passive scalar transport equations in a variable density framework. Results are compared to the DNS data from Nicoud et al

[72]. Lastly, turbulent inflow conditions are presented, reviewed and applied to the momentum driven boundary layer studied by Spalart [25] with the modification of adding uniform transpiration through a section of the surface. This is an important test case since it demonstrates the CFD modeling capabilities in flows that are inhomogeneous in the streamwise direction, the use of turbulent inflow condition, and provides a canonical configuration similar to the pyrolysis transpiration that occurs in wall flame problems. Turbulent characteristics like a turbulent redevelopment length (due to inflow conditions) are demonstrated and self-similarity profiles are recovered for the non-blowing region.

In general, the systematic process of validation has been described as using the right models for a particular study. Validation examines if the conceptual models, computational models as implemented into the CFD code and computational simulation agree with real world observations. The most rigorous strategy is to identify and quantify error and uncertainty through comparison of simulation results with benchmark experimental data; note that we limit ourselves to DNS data here. The experimental data sets themselves will contain bias errors and random errors which must be properly quantified and documented as part of the data set. The accuracy required in the validation activities is dependent on the application, and so, the validation should be flexible to allow various levels of accuracy. According to Coleman et al [73], sources of errors and uncertainties in results from simulations can be divided into two distinct sources: modeling and numerical. Modeling errors and uncertainties are due to assumptions and approximations in the mathematical representation of the physical problem (such as mathematical equations, boundary conditions, turbulence models, etc.) and incorporation of previous data (such as fluid properties) into the model. Numerical errors and

uncertainties are due to the limitations of the numerical solution of the mathematical equations (such as discretization, artificial dissipation, lack of conservation of mass, momentum, and energy, computer round-off, etc.). Detailed approaches to estimating experimental uncertainties are presented and discussed by Coleman and Stern [73]. Similar systematic validation reports have been studied for major CFD software developed in industry (Boeing, General Electric, General Motors) and federal national laboratories such as Sandia National Laboratories, NIST, etc. Our focus in this section of the thesis is to validate our simulation results with DNS benchmark data and ensure that the physical trends and major physical aspects of the flow are accurate. Although, this is not as rigorous as industry based V&V (verification and validation) studies; it does provide a serious level of confidence in the initial state of development of the code.

4.1 Turbulence in Adiabatic Channel Flows

A classical turbulent benchmark case used to study the mechanics of wall-bounded turbulent flows is the Moser et al. configuration originally presented in a landmark paper [71] and extensively referred to in this thesis. The referred work presents a direct numerical simulation of plane turbulent channel flow where all essential scales of motion are resolved. This provides a valuable database for quantitative and qualitative studies of turbulent structure in wall bounded flows and for validation of turbulence closure models.

4.1.1 Wall bounded Terminology and Resolution Requirements

In near wall turbulent flows the viscosity and the wall shear stress are important parameters. Normally a model for the turbulent structure is proposed which consists of two distinct regions, a viscous layer and an outer region (log region). The difference in the regions lies in their contributions to the total shear stress profile $\frac{\tau}{\rho} = (\nu + \nu_t)\partial u/\partial y$ where for the viscous sublayer $\nu > \nu_t$ and for the outer region $\nu < \nu_t$. Viscous scales are normally defined based on these quantities for appropriate velocity-scales and length-scales close to the wall. The friction velocity, $u_\tau = \sqrt{\tau_{wall}/\rho}$, and the viscous length scale $\delta_\nu = \nu/u_\tau$ are used to define the friction Reynolds number as $Re_\tau = \frac{u_\tau \delta}{\nu} = \frac{\delta}{\delta_\nu}$ where δ is the channel half-height, $\delta = 1$. The distance from the wall in viscous units is defined by $y^+ = \frac{u_\tau y}{\nu}$, also called wall-units, where by inspection we can see that the role of wall-units is similar to a measure of the local Reynolds number. Wall-normal velocity and pressure can also be defined in wall units, in summary:

$$u^+ = \frac{u}{u_\tau} = \frac{u}{\sqrt{\frac{\tau_{wall}}{\rho}}} = \frac{\frac{u}{u_{inf}}}{\sqrt{\frac{C_f}{2}}}, \quad y^+ = \frac{y u_\tau}{\nu} = \frac{y \sqrt{\frac{\tau_{wall}}{\rho}}}{\nu} = \frac{y u_{inf} \sqrt{\frac{C_f}{2}}}{\nu}$$

$$v^+ = \frac{v}{u_\tau} = \frac{v}{\sqrt{\frac{\tau_{wall}}{\rho}}} = \frac{\frac{v}{u_{inf}}}{\sqrt{\frac{C_f}{2}}}, \quad p^+ = \frac{p-p_\infty}{\rho u_\tau^2}$$

In principle the above normalizations are used to obtain a universal law of the wall for the viscous blayer and the outer region (log-region). This is done through integration of the normalized total shear profiles and invoking the classical Prandtl

mixing length hypothesis. The results are the law of the wall valid for turbulent boundary layers and channel flows for the case of a negligible streamwise pressure gradient.

The law of the wall which states that in the viscous sublayer region ($y^+ < 5$)

$$u^+ = y^+$$

And in the log-law region ($y^+ > 30$)

$$u^+ = \frac{1}{K} \ln(y^+) + B$$

where $K = 0.41$ is the Von Karman constant and $B = 5.2$ is a turbulent constant. Note that the region between the viscous layer ($y^+ < 5$) and the log-law region ($y^+ > 30$) is called the buffer layer. It is the transition region between the viscosity dominated and the turbulence dominated parts of the flow.

Wall bounded large-eddy simulations have stringent resolution requirements, similar to DNS, near the wall. This is necessary in order to capture the wall-layer structures that arise when a solid boundary is present. This type of technique is called a “wall-resolved” large-eddy simulation. When designing a turbulent grid for this configuration, one of the objectives will be to spatially resolve the viscous region, log region and the inner layer eddies. In the outer layer, the important eddies will scale with the boundary layer thickness or characteristic length-scale, like the channel half-height δ , and its resolution should be of order δ . The resolution of the inner-layer is much more demanding since its dynamics are dominated by sweeping and ejecting processes that are generated by the presence (and destruction) of quasi-streamwise vortices. The dimensions of these vortices are constant when normalized in wall-units. Therefore to

resolve the sublayer, constant grid spacing in wall units must be used [21]. For channel flows this requirement results in streamwise and spanwise grid sizes of: $\Delta x^+ \cong 100, \Delta z^+ \cong 20$ for spectral methods and $\Delta x^+ \cong 50, \Delta z^+ \cong 15$ for second order finite difference solvers with both enforcing $y_{min}^+ \leq 1$ as suggested by Piomelli[74] . Effective grid design is achieved through hyperbolic stretching in the wall-normal direction, clustering the grids in the inner region and using coarser resolution in the outer region.

4.1.2 Computational Domain

Fully developed plane channel flow is homogeneous in the streamwise (x) and spanwise directions (z) and periodic boundary conditions can be used in these directions. The use of periodicity in the homogenous direction is valid as long as the relevant computational dimension is chosen to include the largest eddy in the flow. The periodic domain sizes were originally selected by Moser et al [71], so that the two point correlations in x and z would be near zero at half the domain size. The pressure gradient that drives the flow is adjusted at every time step to impose a constant mass flux through the channel. This is based on the following conservation equation,

$$\left(\frac{dP}{dx}\right)^{n+1} = \left(\frac{dP}{dx}\right)^n - 2\left(\frac{\dot{m}^{*n} - \dot{m}}{\Delta t}\right) - \left(\frac{\dot{m}^{*n-1} - \dot{m}}{\Delta t}\right)$$

where \dot{m}^{*n} is the calculated mass flux at the current time level and \dot{m} is the required mass flux ($\dot{m}^{*n} = \rho u$). The computation is performed using the LES Dynamic Eddy Viscosity model with approximately 200,00 grid points (48, 65, 64 in x, y, z) with a frictional Reynolds number of $Re_\tau = 395$, based on the frictional velocity and channel half-height. A classical dynamic model, as presented in Chapter 2, is utilized to provide

the relationship between the Smagorinsky dynamic coefficient and the shear stress. The minimization technique of Lilly (discussed in chapter 2) is used to solve for the dynamic coefficient as presented in Table 6. The streamwise and spanwise computational lengths are chosen to be 2π and π respectively with the channel half-height defined as $\delta = 1$; see Figure 17. With this computational domain, the grid spacing in the streamwise and spanwise directions are respectively $\Delta x^+ = 50$ and $\Delta z^+ = 15$ in wall units (where $x_i^+ = x_i u_\tau / \nu$), a non-uniform mesh is used in the wall-normal direction where the first point away from the wall is at a distance $y^+ \cong 1$ and the maximum spacing at the center of the channel is $y^+ \cong 15$.

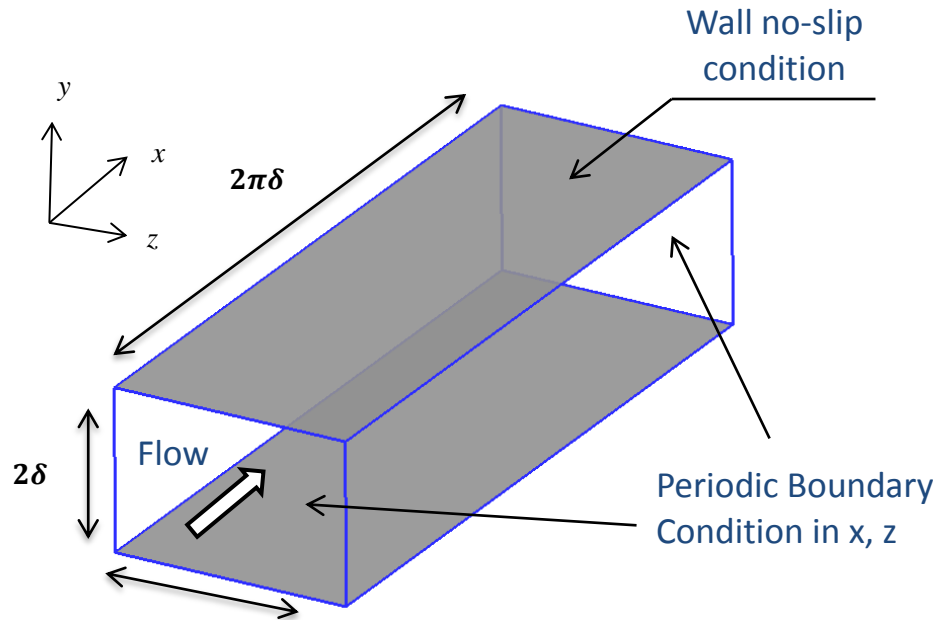


Figure 17. Schematic of the channel configuration showing spatial coordinates and domain size.

$(L_x L_y L_z)^*$	$(n_x n_y n_z)$	<i>grid stretching</i>
$(2\pi\delta, 2\delta, \pi)$	$(48, 65, 64)$	Wall –normal hyperbolic ($\alpha = 2.75$) Uniform grid in x, z
<i>Resolution criteria</i> (finite differences)	<i>Turbulence model</i>	<i>Turbulent coefficient</i> <i>Minimization technique</i> (Lily, et al)
$\Delta x^+ \cong 51$ $\Delta z^+ \cong 19$ $y^+ \cong 0.8$	LES Dynamic eddy viscosity (Smagorinsky type model)	$C_{ev}(x, y, z, t)$ $= -\frac{1 \langle L_{ij} M_{ij} \rangle_{avg}}{2 \langle M_{ij} M_{ij} \rangle_{avg}}$
$Re_{bulk} = 6900$ $Re_{\tau} = 395$	$\tau_{ij}^r = -2\nu_t \bar{S}_{ij}$ $= -2C_{ev} \Delta^2 \bar{S}_{ij} \bar{S}_{ij}$	Averaging type: Lagrangian Planar (option) Line (option)
<i>wall boundary</i>	<i>Mass flux option</i>	<i>Periodicity</i>
$u = v = w = 0$ $T_{wall} = 300K$	Adjust pressure gradient to maintain constant mass flux	Streamwise, Spanwise

Table 6. Physical parameter table for the turbulent channel flow configuration. The table presents initial conditions, boundary conditions, and turbulence models.

4.1.3 Results

The computational study is performed following the parameter table presented in the previous section in Table 6. Initial conditions in the channel are specified with random noise having a magnitude of 40% serving as a kick-start for channel flow instabilities. The flow field variables are integrated forward in time until the flow reaches a statistically steady state. The steady state can be identified by a linear profile of the total shear stress $-\overline{u'v'} + \nu\partial\bar{u}/\partial y$ and by a stationary total kinetic energy. The fluctuations of turbulent kinetic energy serve as a good monitor for the total energy variations in the channel. Thus, the simulation total run time has to include the development of a stationary turbulent kinetic energy history plus several time scales designated large-eddy turn over time (LETOT), $LETOT \sim \frac{\delta}{u_{rms}}$. A total of 10 LETOTS were used in this study with 5 measurements taken per time-scale. Thus, the post-processing of the random fields $U_i(x, t)$ is done by performing a temporal average and a spatial average over horizontal planes in the homogeneous directions to obtain the various statistical correlations.

The profiles of the mean streamwise velocity, non-dimensionalized by the friction velocity, is shown in Figure 18a. Also shown in the figure is the mean velocity profile from the DNS results from Moser et al [71]. The dashed lines represent the law of the wall and the log law. Within the viscous sublayer, $y^+ < 5$, both results follow the linear law of the wall. Similarly in the log-layer, $y^+ > 10$ simulation results show good comparison to the log-law and to the DNS data except for the wake region ($y^+ > 200$) where the differences are less than 2 percent.

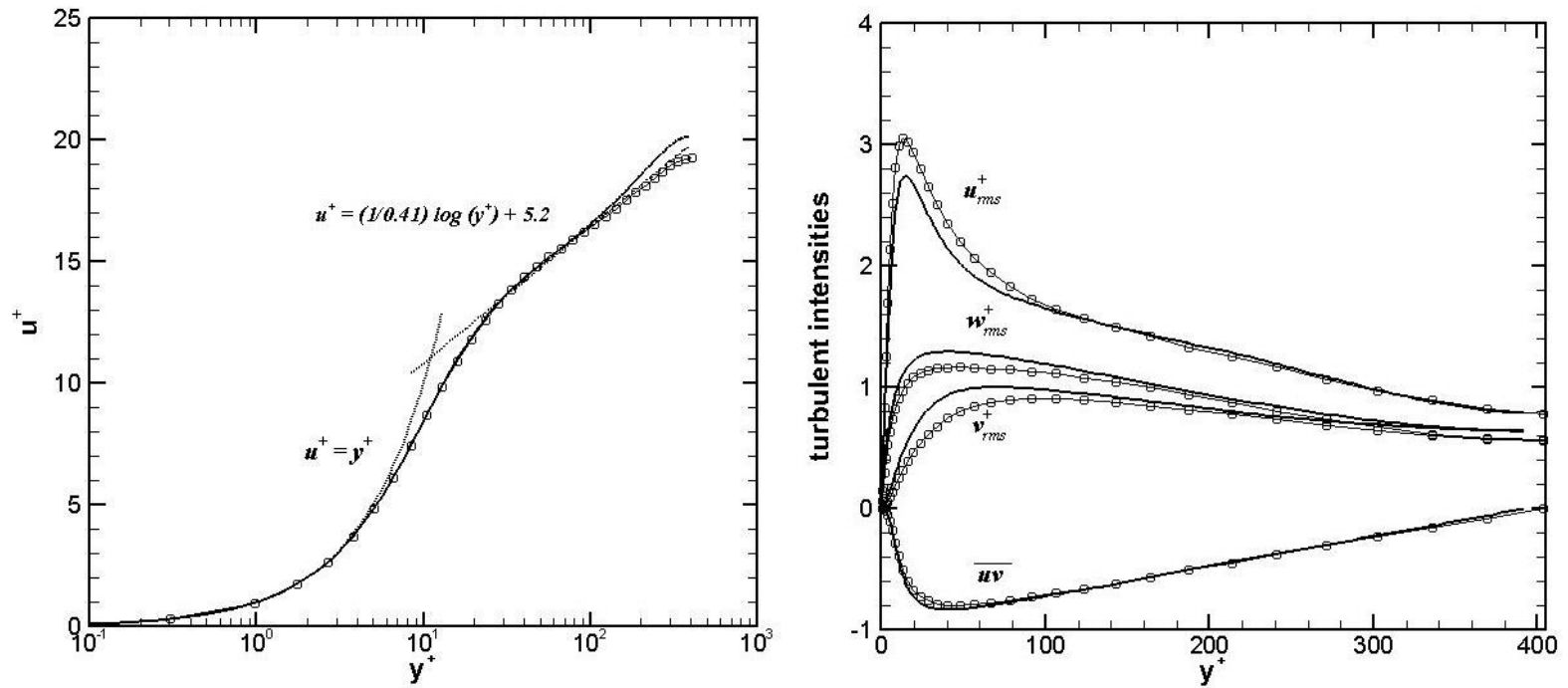


Figure 18. Statistical presentation of a turbulent channel flow results for $Re_\tau = 400$. Top left figure shows the mean velocity profiles in wall-units, the right figure shows the turbulent intensity profiles; Symbols (\odot) are current LES simulations and the solid black line (-) is the reference DNS.

Turbulent intensities normalized by the frictional velocities are shown in Figure 18b and they are compared with DNS results at Reynolds number $Re_\tau = 400$. This is shown up to the centerline of the channel since the profiles are symmetrical. The symmetry of the profiles also shows the adequacy of the sample taken for the average. Although the shape of the profiles agree very well in the wake and log-region, one can still see differences below $y^+ \sim 150$ and in particular below the viscous wall region $y^+ < 50$. The modeling of the viscous region is a complex task since it contains the most vigorous turbulent activity. The production, dissipation, turbulent kinetic energy and anisotropy all achieve their peak values at $y^+ < 20$ for flows at high Reynolds numbers [5]. It is due to these phenomena that the modeling errors are most evident in this region. Also shown in Figure 18b are comparisons of the Reynolds stress, \overline{uv} . Similar to the intensity profiles, the wake and outer region provides the best comparison to the actual turbulence physics. The Reynolds shear stress and its constituents are plotted in Figure 19. Due to conservation of mechanical energy and statistical convergence we should expect the total shear stress to be linear across the channel. The behavior of the total shear stress in the vicinity of a wall for a fully developed channel flow can be deduced from the following equation,

$$-\frac{\langle \overline{uv} \rangle}{u_\tau^2} + \frac{\langle 2vt_{sgs}S_{12} \rangle}{u_\tau^2} + \left\langle \frac{du^+}{dy^+} \right\rangle = 1 - \frac{y^+}{\delta^+}$$

where the components are: the resolved turbulent stress, the modeled subgrid scale stress and the viscous stress, respectively. The linearity of the conservation property will hold true once we add the total shear constituents. One subtlety encountered in this analysis is

that post-processing must include the product of the subgrid-scale eddy viscosity and rate of strain inside the averaging operator due to its spatial and temporal variations in the flow.

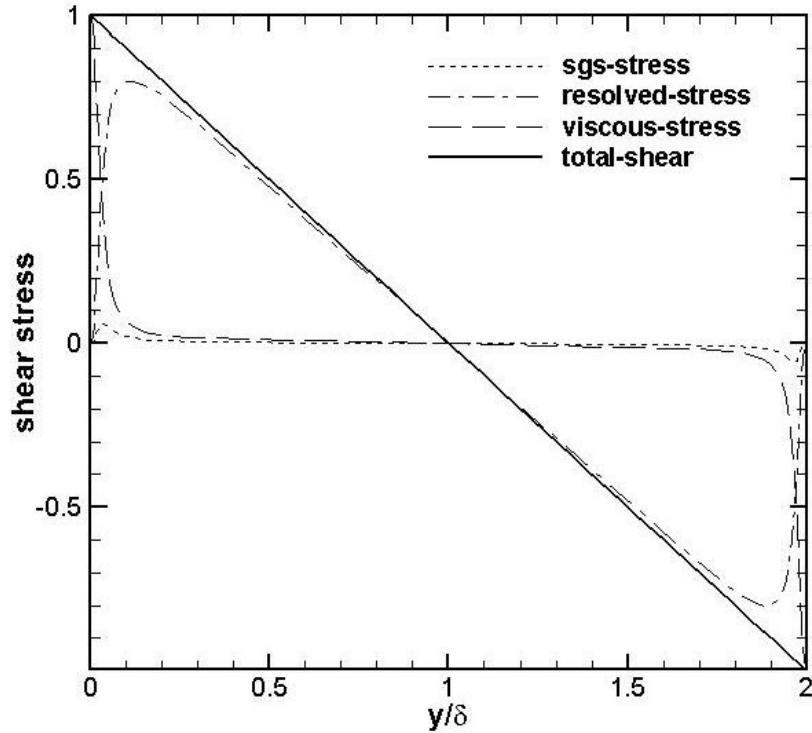


Figure 19. Reynolds shear stress normalized by friction velocity, $Re = 400$; The solid black line represents the total shear stress (summation of each component) across the channel.

Visualization of the flow field is shown on Figures 20(a)-(b). Figure 20 presents three dimensional contours of the velocity field showing an instantaneous representation of the turbulent field. To obtain a better representation of the turbulent structure, visualization methods have been developed and formulated in terms of the invariants of the velocity gradient tensor $\partial u_i / \partial x_j$ (where the decomposition of velocity gradient can be made into

isotropic, symmetric-deviatoric, and antisymmetric parts: $\frac{\partial U_i}{\partial x_j} = \frac{1}{3}(\delta_{ij} + S_{ij} + \Omega_{ij})$. The

Q criterion locates regions where rotation dominates over strain in the flow. Letting S_{ij}

and Ω_{ij} denote the symmetric and anti-symmetric parts of $\frac{\partial U_i}{\partial x_j}$, one defines Q as the

second invariant of $\frac{\partial U_i}{\partial x_j}$, given as,

$$Q = \frac{1}{2}(\Omega_{ij}\Omega_{ij} - S_{ij}S_{ij})$$

Where S_{ij} is the rate of strain tensor defined as $S_{ij} = \frac{1}{2}\left(\frac{\partial u_i}{\partial x_j} + \frac{\partial u_j}{\partial x_i}\right)$ and $\Omega_{ij} =$

$\frac{1}{2}\left(\frac{\partial u_i}{\partial x_j} - \frac{\partial u_j}{\partial x_i}\right)$ is the rate of rotation tensor. A coherent vortex is defined as a region where

$Q > 0$.

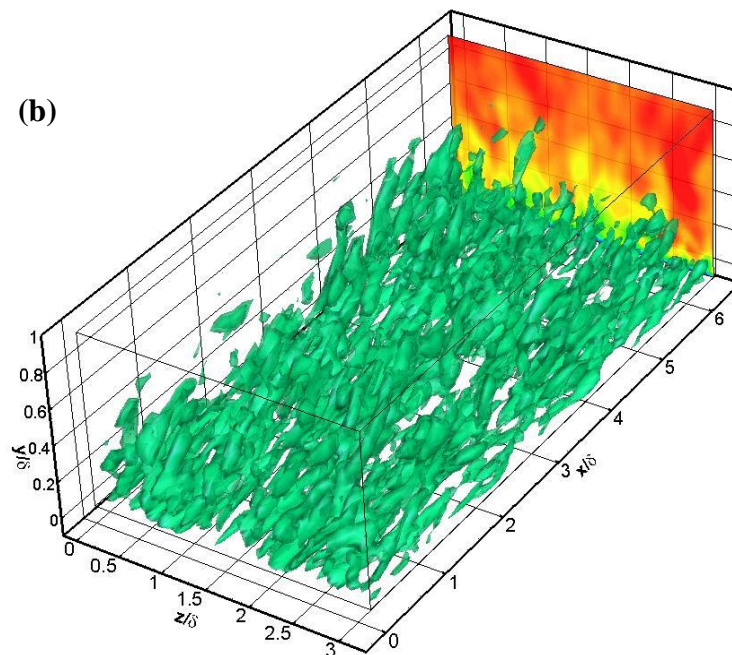
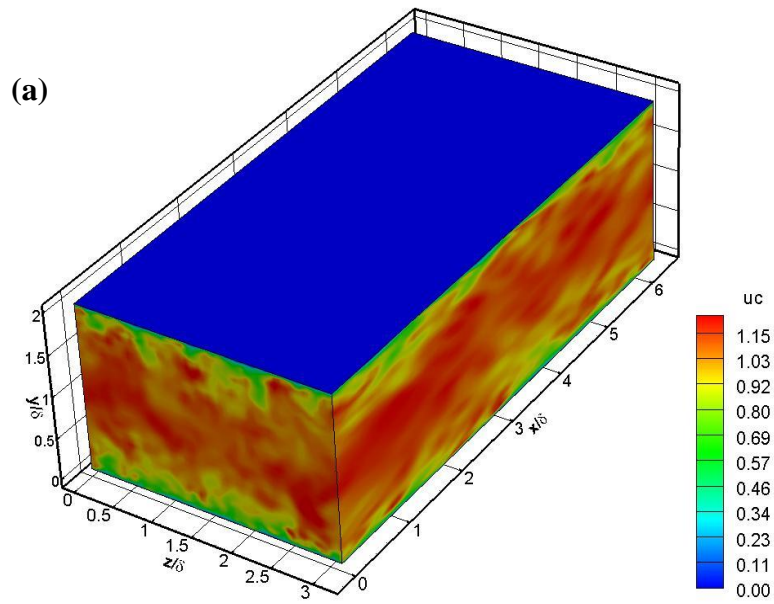


Figure 20. (a) Instantaneous three dimensional velocity iso-contours (b) Turbulent eddy structure presented using the Q-criterion ($Q=3$) visualization technique – the back plane shows u -velocity iso-contours.

4.2 Turbulence in Channel Flow with Variable Property

The objective of this section is to validate a turbulence study for the case where thermo-physical properties vary due to strong temperature gradients. This corresponds to a low-Mach number regime where compressibility effects can be neglected ($M < 0.3$) and the effects of variable density based solely on temperature can be studied. Also, of interest is the performance of the large-eddy simulation models in complex cases where large variations in temperature, density and turbulence are coupled.

4.2.1 Wall-Bounded Terminology and Resolution Requirements

The configuration used in this section corresponds to a planar channel with isothermal walls at different temperatures; see Figure 21. In this case the lower wall (designated cold wall) is isothermal at $T_1 = 300 K$ and the upper wall (designated hot wall) is also isothermal at $T_2 = 600 K$. A classical Suntherland's law for viscosity is used where $\nu \propto f(T)$ is used based on the reference temperature at the cold wall. In this way,

the bulk Reynolds number is defined as $Re_{bulk} = \frac{u_{bulk}\rho_{cold}\delta}{\mu_{cold}}$ where the bulk velocity is

$u_{bulk} = \frac{\int \rho(y)u(y)dy}{\int \rho(y)dy}$ (and is also a measure of the channel mass flux) and the values of

density and dynamic viscosity correspond to cold wall values. A skin friction coefficient,

$C_{f_i} = \frac{\tau_{wall_i}}{2\rho_i U^2}$, is also used to characterize the flow at each wall where it is defined based

on the mean density in the channel and maximum velocity. We define non-dimensional quantities based on the viscosity, wall shear stress and heat flux. The opposing signs of temperature gradients at each wall indicate that the normalization of dependent variables in viscous units will be anti-symmetrical. The “thermal” viscous units for this case are

defined based on the frictional velocity $u_{\tau_i} = \sqrt{\frac{\mu}{\rho_i} \frac{du}{dy} \Big|_i}$ and heat flux parameter

$B_{q_i} = \frac{-k_{wall} \frac{dT}{dy}|_i}{\rho_i C_p u_{\tau_i} T_{wall_i}}$ where the index $i = 1, 2$ indicates the cold and hot wall, respectively.

Thus the viscous wall units are described by use of the superscript $^+$ and defined as,

$$y_i^+ = \frac{y \rho_i \delta}{\mu_i}, \quad u_{\tau_i}^+ = \frac{u}{u_{\tau_i}}, \quad T_i^+ = \frac{(T_{wall_i} - T)}{B_{q_i} T_{wall_i}}$$

4.2.2 Computational Domain

The simulation is performed with periodic conditions applied in the homogenous directions, namely the streamwise (x) and spanwise (z) coordinates. Isothermal walls are specified through the use of Dirichlet boundary conditions prescribing the hot and cold wall boundaries and no-slip conditions specify the non-permeable kinematic wall condition. The pressure gradient is adjusted at every time step to impose a constant mass flux through the channel. The variable density turbulence models developed and implemented are the LES Dynamic Eddy Viscosity and Dynamic Eddy Diffusivity models with classical Smagorinsky type arguments used to describe the relationship between dynamic coefficients, shear stress and heat flux. An extension of the turbulent coefficient minimization scheme is used for the temperature scalars where a Lagrangian averaging option suitable for complex (non-homogenous) flows is utilized. The computational periods and grid details were selected following the suggestion of Nicoud et al [72] where the grid spacing in the streamwise and spanwise directions are respectively $\Delta x^+ = 30 - 50$ and $\Delta z^+ = 8 - 15$ in wall units.

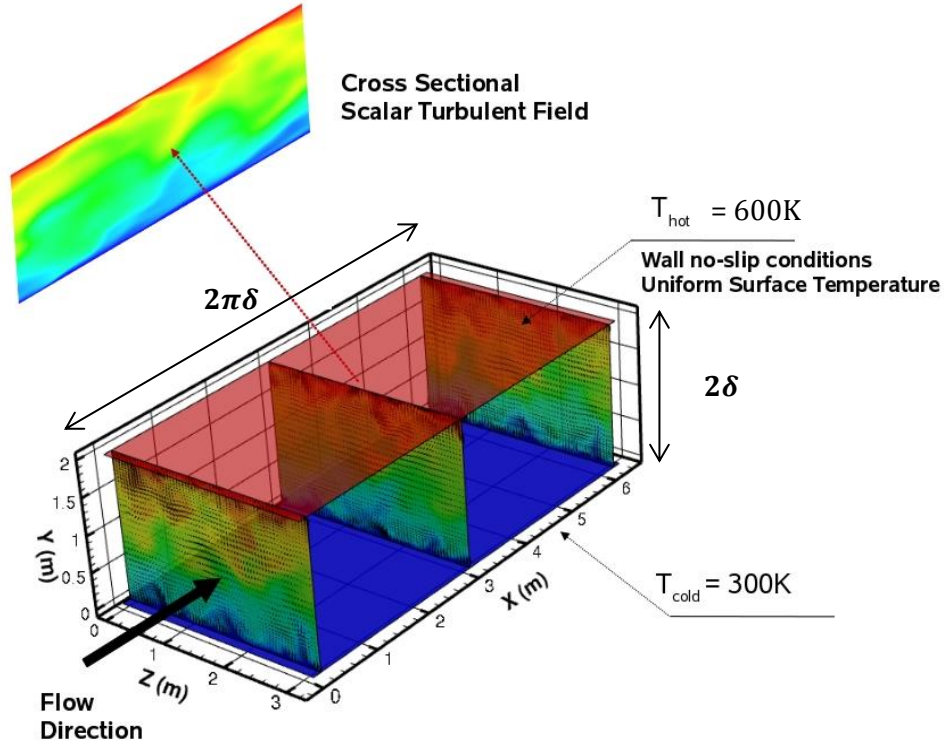


Figure 21. Schematic of the heated channel configuration showing spatial coordinates and isothermal boundary conditions.

$(L_x L_y L_z)^*$	$(n_x n_y n_z)$	<i>grid stretching</i>
$(2\pi\delta, 2\delta, \pi\delta)$	(48,65,64)	Wall-normal hyperbolic ($\alpha = 2.75$) Uniform grid in x, z
<i>Resolution criteria</i> (finite differences)	<i>Turbulence model</i>	<i>Turbulent coefficient</i> <i>Minimization technique</i> (Lily et al.)
$\Delta x^+ \cong 30 - 50$ $\Delta z^+ \cong 8 - 15$ $y^+ \cong 1$	LES Dynamic eddy viscosity (Smagorinsky type model) $\tau_{ij}^r = -2\nu_t \bar{\delta}_{ij} = -2C_{ev} \Delta^2 \bar{\delta}_{ij} \bar{\delta}_{ij}$	$C_{ev}(x, y, z, t)$ $= -\frac{1 < L_{ij} M_{ij} >_{avg}}{2 < M_{ij} M_{ij} >_{avg}}$
$Re_{bulk} = 2700$	LES Dynamic eddy diffusivity $q_j = -\bar{\rho} C_\theta \frac{\partial \tilde{T}}{\partial x_j}$	$C_\theta(x, y, z, t)$ $= \frac{< K_j T_j >_{avg}}{< T_j T_j >_{avg}}$ Averaging type: Lagrangian Planar (option) Line (option)
<i>wall boundary</i>	<i>Mass flux option</i>	<i>Periodicity</i>
$u = v = w = 0$ $T_{cold} = 300K$ $T_{hot} = 600K$	Adjust pressure gradient to maintain constant mass flux	Streamwise, Spanwise

Table 7. Physical parameter table for the turbulent channel flow configuration. The table presents initial conditions, boundary conditions, and turbulence models.

4.2.3 Results

The results presented in this section are generated through a configuration file that follows the parameters presented in Table 7. A kick-start condition of random noise having a magnitude of 40% is applied to provide unsteady flow instabilities. The fluctuations of turbulent kinetic energy are closely monitored seeking to obtain a stationary state. The added complexity in this case is the inherent coupling between the scalar and momentum equations and the mixing time scales provided through heat flux from the isothermal walls. The heat flux introduces a thermally diffusive component to the heat transfer process that scales in time like $t \sim \delta^2/D$ and is considerably slower (one order of magnitude larger) than the convective time scales, $t \sim \frac{U}{L}$. This makes the simulation run time substantially longer to obtain a steady profile of kinetic energy. Once this profile is reached a total of ten large-eddy turn over times are used as a total sampling time interval, where five data intervals are recorded per LETOT. Statistical post-processing of the flow-variables is done by performing a temporal average and a spatial average over horizontal planes in the homogeneous directions to obtain the various statistical correlations.

Figures 22(a-b) show that our mean velocity and temperature profiles are in good agreement with the DNS results obtained by Nicoud [72]. The non-dimensional velocity profile, Figure 22a, is presented in terms of $\frac{u}{u_{max}}$ along with a dimensional temperature profile shown in Figure 22b. Figure 22(a-b) also shows that the velocity and temperature gradients are larger near the cold wall (at $y = 0$) through further observation this indicates the asymmetry in the profile. Note however that through Sundtherland's law, the magnitudes of the heat flux through both walls are approximately the same.

Figures 23 (a-b) show the mean velocity and temperature profiles in viscous thermal wall-units. The results are presented in-terms of the cold and hot wall, where the results show distinct behavior for each wall profile in the buffer and log layer region, and a similarity condition is observed as y^+ approaches zero. The variation between the hot and cold wall profiles are due to the local values of thermo-physical properties, i.e., u_τ, B_q , and the definitions of the viscous parameters for this configuration.

Turbulent intensities are shown in Figures 24 (a-b) for streamwise velocity and temperature. Velocity intensities show peak regions of turbulent activity below $y^+ < 50$ for both cold and hot wall. The cold wall shows a larger contribution to both velocity and temperature peak intensities possibly due to presence of larger temperature and velocity gradients seen near the cold surface ($y=0$) driving the shear mechanism and enhancing turbulent activity.

Wall-normal and spanwise velocity intensities are presented in Figure 25 (a-b). In contrast to Figure 24, the regions of peak turbulent activity have shifted out to $y^+ \sim 60$ and remain fairly constant beyond this point. Note however that the cold wall peak predominance remains and it is observed that the effect of heat transfer is to mitigate the turbulence due to the enhanced viscosity relaminarizing the flow field.

Visualization of velocity and temperature flow variables is shown in Figure 26 (a-b). The pictures present three dimensional contours showing an instantaneous representation of the turbulent field. Close inspection of the temperature iso-contours near the hot wall reveals significantly larger turbulent structures demonstrating the relaminarization process coupled with scalar diffusive mixing across the channel.

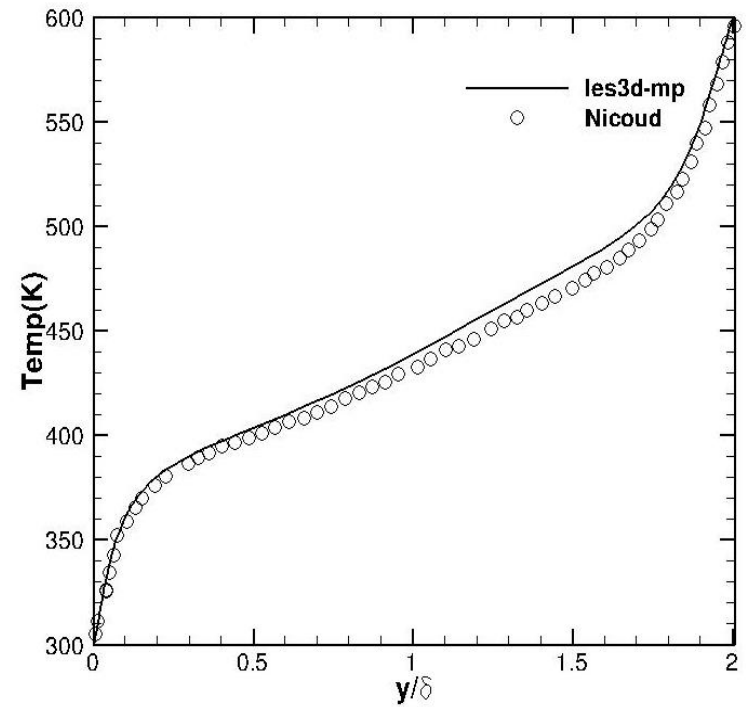
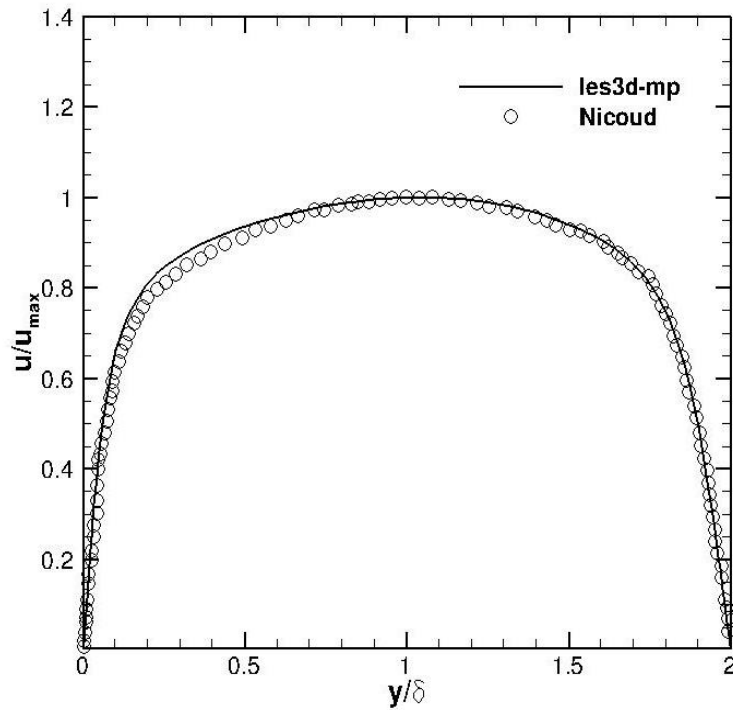


Figure 22. First order statistical analysis: (a) Mean velocity and (b) mean temperature profiles across the channel in line-units; for both cold and hot walls.

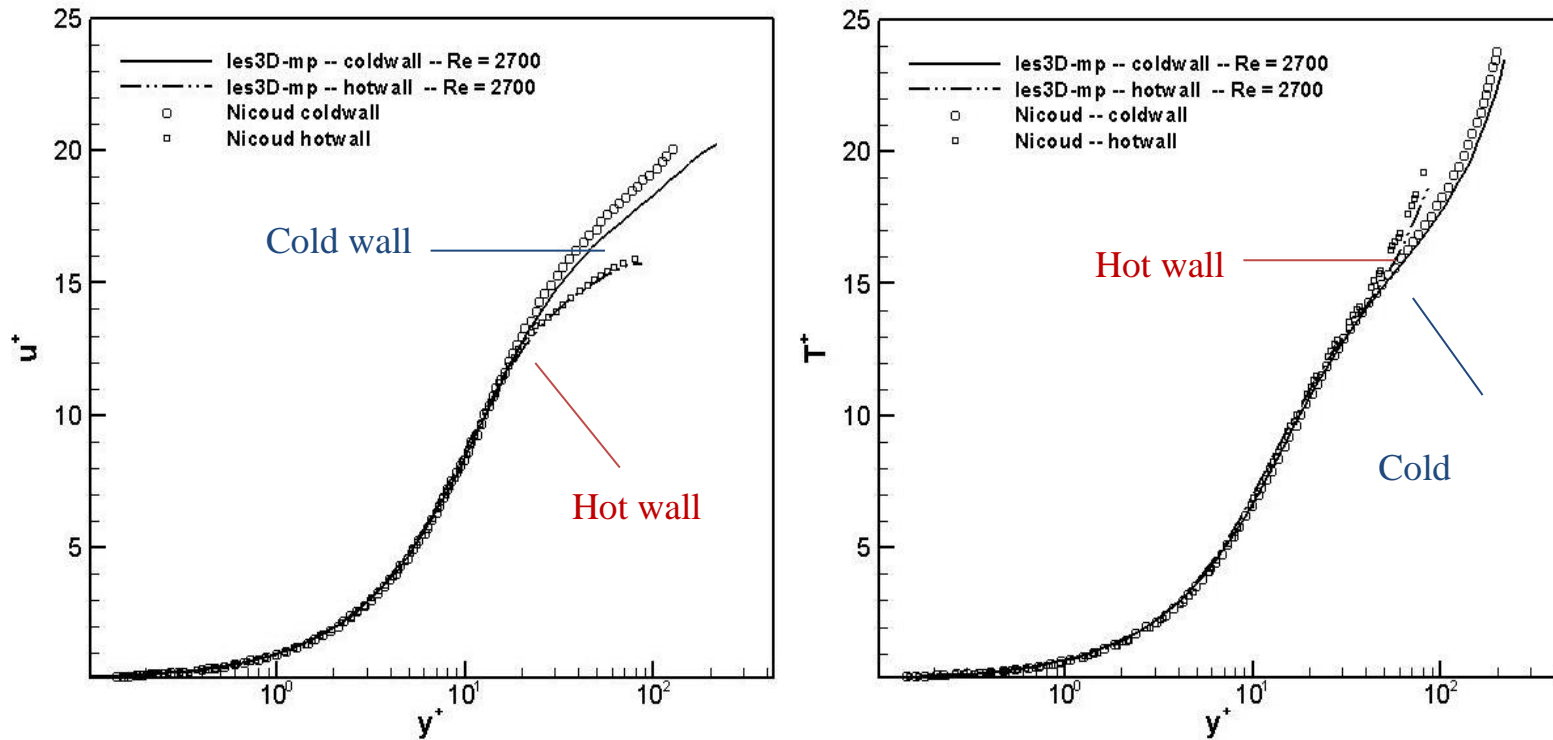


Figure 23. First order statistical analysis: (a) Mean velocity and (b) mean temperature profiles across the channel in thermal viscous units; for both cold and hot walls.

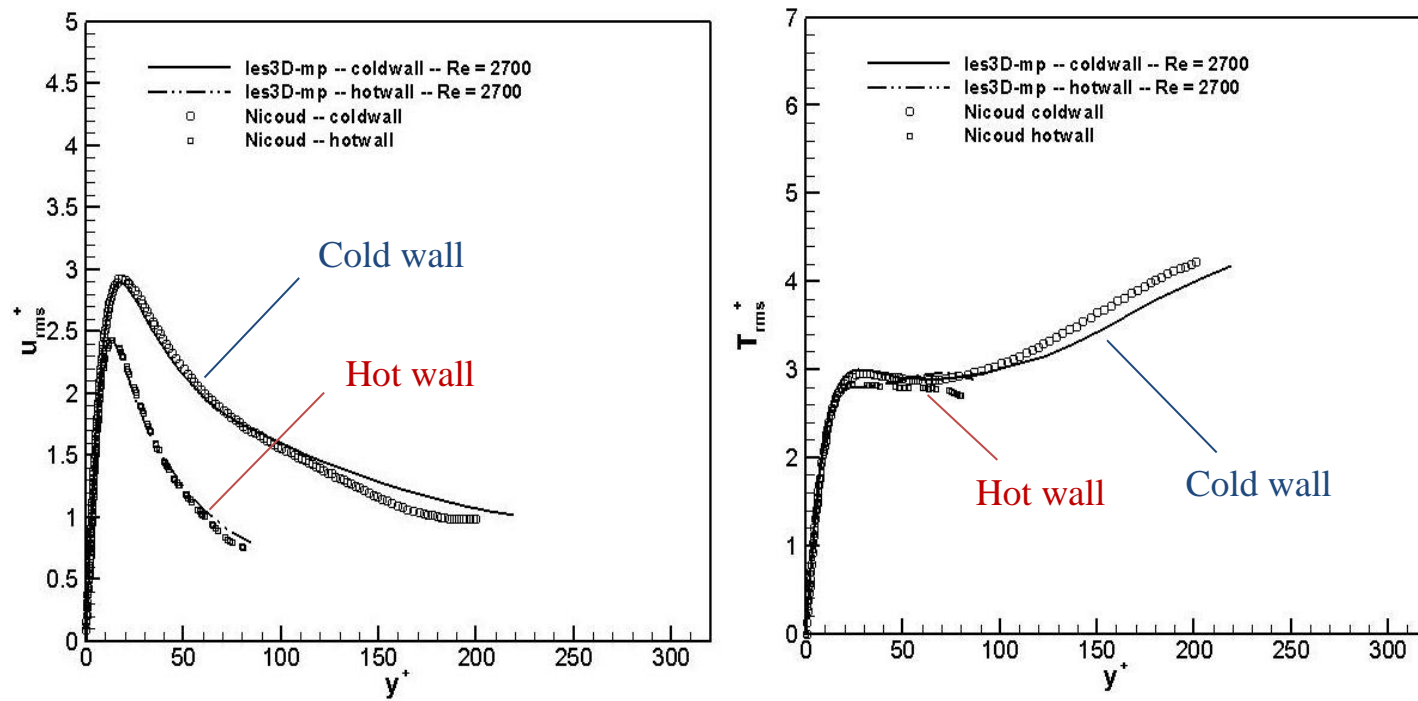


Figure 24. Second order statistical analysis: (a) velocity turbulent intensity profiles and (b) temperature intensity profiles; for both cold and hot walls.

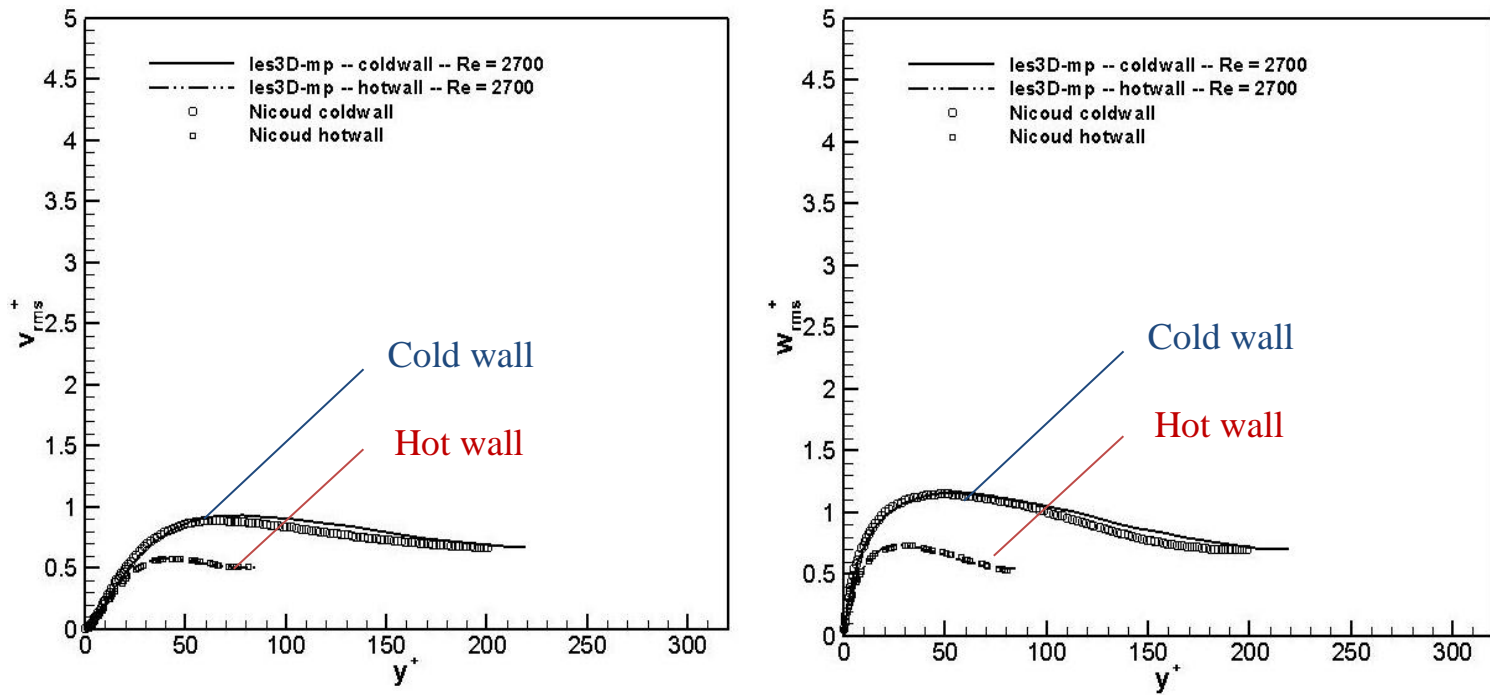


Figure 25. Second order statistical analysis: (a) wall-normal velocity turbulent intensity profiles and (b) spanwise velocity turbulent intensity profiles; for both cold and hot walls.

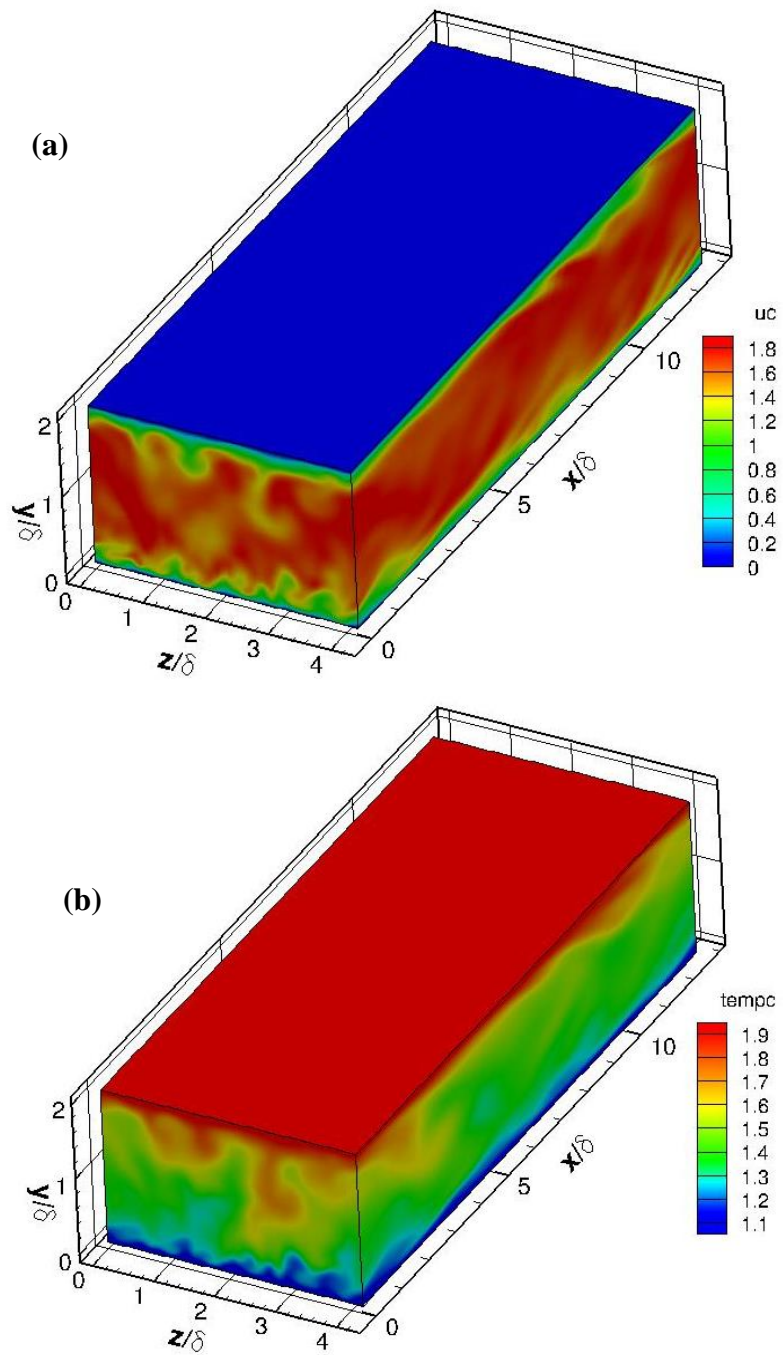


Figure 26. Instantaneous three dimensional iso-contours of (a) streamwise velocity and (b) normalized temperature in the channel.

Additionally, properties at both the cold and hot wall were calculated and compared to the values provided by Nicoud [72]. The results are shown in the following table,

	T_2/T_1	$\frac{u_{\tau_1}}{u_\tau}$	$\frac{u_{\tau_2}}{u_\tau}$	C_{f_1} (10^3)	C_{f_2} (10^3)	B_{q_1}	B_{q_2}	Re_{τ_1}	Re_{τ_2}
Current	2	0.87	1.12	7.04	5.88	-0.019	0.014	225	89
Nicoud	2	0.87	1.13	6.5	5.6	-0.018	0.014	200	82

Table 8. Turbulent heated channel with variable properties; comparison of wall properties between les3D-mp results and reference DNS simulations of Nicoud et al [72].

Table 8 shows good agreement for wall friction velocity and heat flux properties.

Nicoud's DNS frictional velocity, $u_{\tau_i} = \sqrt{\frac{\mu}{\rho_i} \frac{du}{dy} \Big|_i}$, is in very close agreement with the results obtained with our current LES approach. Similarly, wall heat flux defined as $B_q = \frac{q_w}{\rho_w c_p u_\tau T_w}$ also shows good agreement between both cases. The overall statistical results for mean, turbulent intensities and wall-properties are within reasonable agreement with Nicoud's DNS data. The main discrepancy comes from the intensity profiles whose differences can be attributed to the expected LES modeling errors.

4.3 Validation of Synthetic Turbulent Inflow Generation

The adiabatic turbulent channel flow case presented in Section 4.1 is extended by applying inflow/outflow conditions in the streamwise direction and assessing the performance of synthetic turbulent inflow with the controlled forcing planes presented in Chapter 2, Section 2.13. The use of synthetic turbulent generating techniques introduces a recovery region associated with a streamwise length scale necessary for the turbulent structure to fully redevelop. This redevelopment length is closely monitored through the skin friction coefficient, C_f , as an indicator of the mixedness of the flow. In addition, two more recovery indicators are defined to measure the redevelopment of the Reynolds stresses. The three indicators are given below,

*Skin friction
Indicator:*

$$C_f = \frac{\tau_w}{1/2 \rho U_b^2}$$

*Resolved q^2
Error*

$$e_{q^2} = \int_{-\delta}^{+\delta} |q_*^2(y) - q^2(x, y)| dy \bigg/ \int_{-\delta}^{+\delta} |q_*^2(y)| dy$$

*Reynolds shear
stress Error:*

$$e_{uv} = \frac{1}{2\delta} \int_{-\delta}^{+\delta} |\langle u'v' \rangle_*(y) - \langle u'v' \rangle(x, y)| dy \bigg/ \max(|\langle u'v' \rangle_*|)$$

where $q_*^2(y)$ is calculated from a baseline periodic adiabatic turbulent channel calculation and $q^2(x, y)$ is obtained from the spatially developing simulation. Similarly in the

Reynolds shear stress error $\langle u'v' \rangle_*(y)$ is the baseline periodic solution and $\langle u'v' \rangle(x, y)$ is the spatially developing contribution.

The baseline computational study was carried out with an adiabatic turbulent channel configuration with periodic streamwise boundary conditions in a domain of $2\pi\delta, 2\delta, \pi\delta$ in $x, y, \text{ and } z$ at a Reynolds number of $Re_\tau = 400$ with the same resolution as in Section 4.1.2 ($48 \times 65 \times 64$). Spatially developing tests were then performed in a channel length of $10\pi\delta, 2\delta, \pi\delta$ with the controller weights of $\alpha = 1$ and $\beta = 50$ with $240 \times 65 \times 64$ grid cells thus keeping the same resolution as in the periodic case $\Delta x^+, y_1^+, \Delta z^+$ of 51, 0.8, 19. These tests featured the use of Batten inflow condition with no controlled forcing, and Batten inflow with controlled forcing with prescribed planes at $x/\delta = 1.3, 2.6, 3.9, 5.2$.

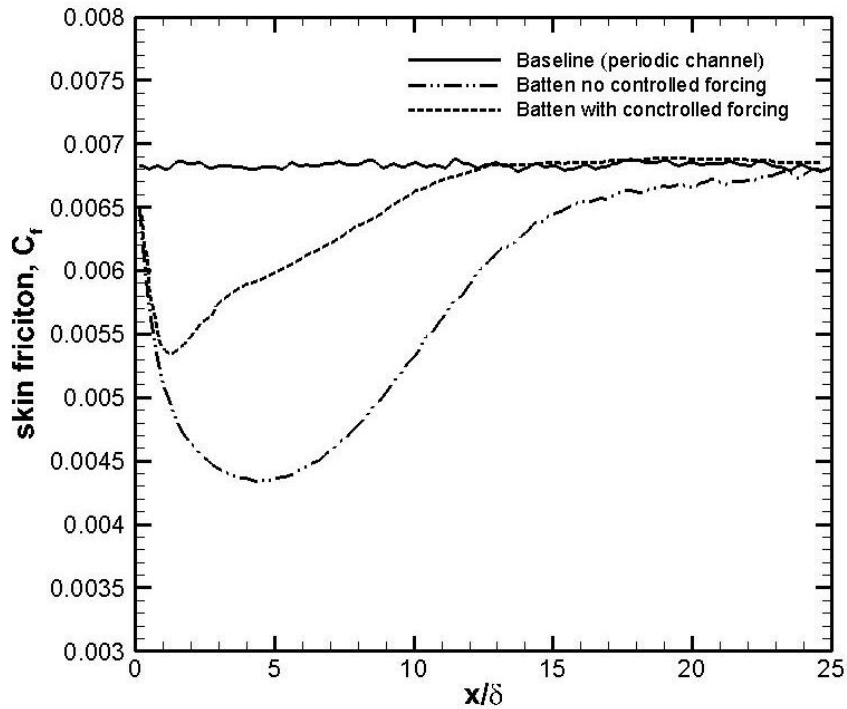


Figure 27. Streamwise development of skin friction coefficient for baseline periodic case, compared to Batten inflow case with no forcing and, Batten inflow with controlled forcing planes.

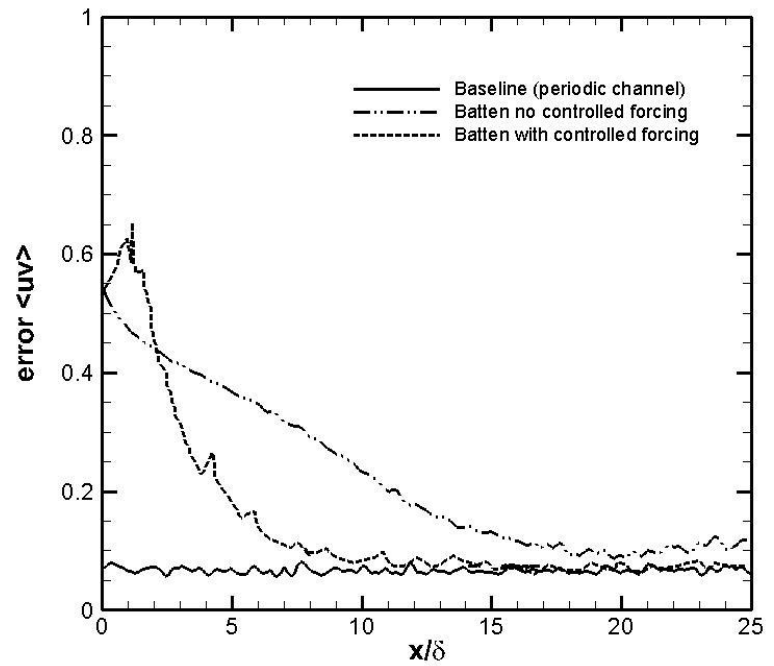
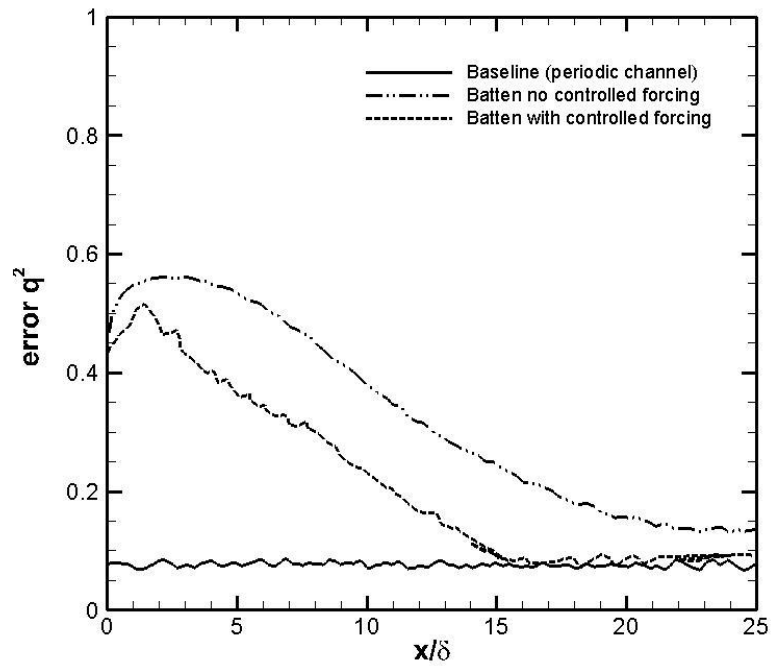


Figure 28. Streamwise development of the integrated errors in (a) resolved turbulent kinetic energy and (b) the Reynolds shear stress conducted for baseline periodic case, Batten inflow case with no forcing ng, and Batten inflow with controlled forcing planes.

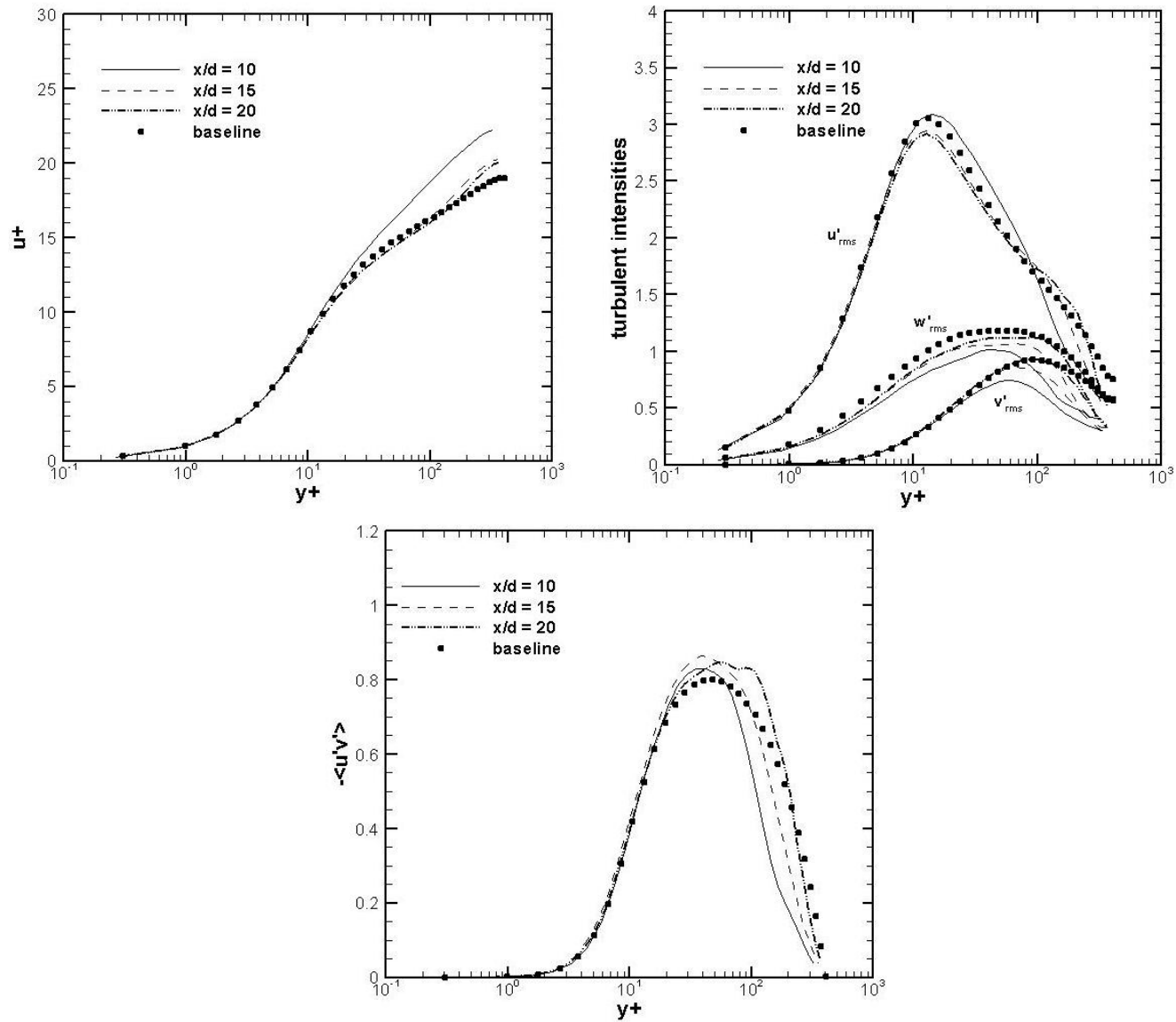


Figure 29. Streamwise development of (a) mean velocity profiles, (b) turbulent intensity profiles, and (c) Reynolds shear stress profiles across the channel at $x/\delta = 10, 15, 20$ with **no controlled forcing**.

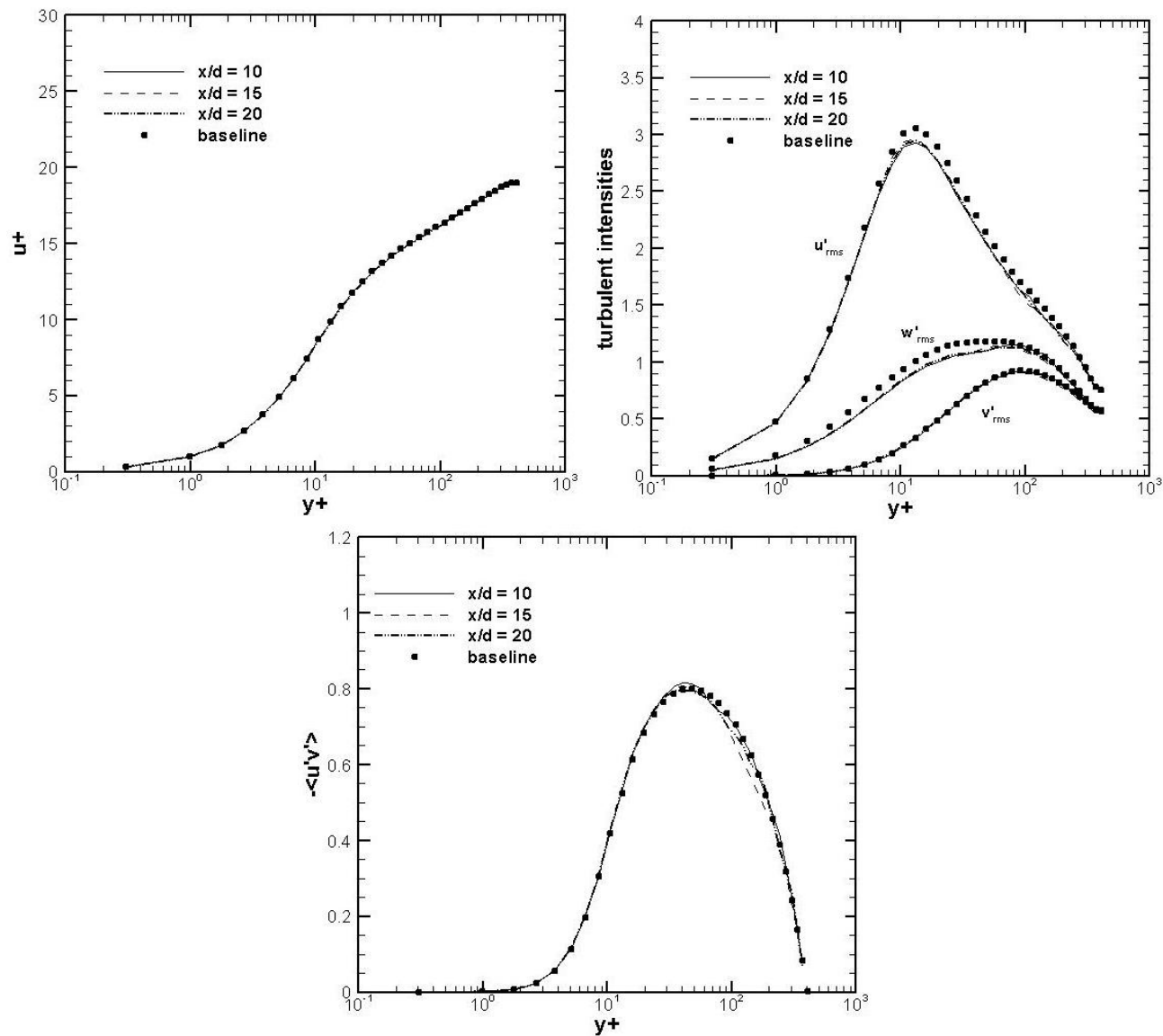


Figure 30. Streamwise development of (a) mean velocity profiles, (b) turbulent intensity profiles, and (c) Reynolds shear stress profiles across the channel at three different stations at $x/\delta = 10, 15, 20$ with **activated controlled forcing planes**

Figure 27 shows the downstream development of the skin friction indicator compared to the results using Batten and controlled forcing at three stations ($x/\delta = 10,15,20$) with the baseline periodic channel case. The use of the controlled forcing planes in addition to the Batten inflow is seen to clearly improve the solution by marking a shorter recovery length of $x/\delta \sim 15$ with controlled forcing, compared to a $x/\delta \sim 25$ recovery length with no controlled forcing. This demonstrates the need to use controlled forcing planes in addition to the Batten inflow when working with turbulent generation techniques since the improvement of the recovery region also marks an improvement in the simulation's computational cost. Figure 28 shows the integrated results for the resolved turbulent kinetic energy and the Reynolds shear stress compared with the baseline showing similar characteristics to Figure 27, that is a shortened recovery region of $x/\delta \sim 15$ when using controlled forcing planes with synthetic inflow conditions.

In Figure 29-30 we show the mean velocity, turbulent intensity and Reynolds shear stress profiles across the channel at three stations in the downstream region (marked as $x/\delta = 10,15,20$). Figure 29 shows the use of synthetic inflow without controlled forcing planes, it shows the discrepancies of the turbulent profiles at the first station and improvements in the solution as the recovery region is approached. Figure 30 features the use of synthetic inflow with controlled forcing planes, comparison with the baseline shows excellent agreement with the baseline case at all the stations. The improved results clearly emphasize the use of controlled forcing with synthetic turbulence inflow techniques for the calculations in spatially developing flows. This premise is demonstrated in Section 4.4 by presenting a boundary layer case.

4.4 Zero Pressure Gradient Turbulent Boundary Layer

Research in turbulent boundary layers is an important topic due to its technological importance and relevance across several fields. Of the turbulent boundary layer flows, the canonical zero-pressure-gradient (ZPG) case, on a flat plate with constant free-stream velocity, has received the most attention (see Figure 27). Recent reviews on these flows (Marusic et al [75], Klewicki et al [76]) discuss the recent findings with respect to scaling, Reynolds numbers effects, and the role of coherent structures and very-large-scale motions in these flows. Compared to a fully developed channel flow with a mean pressure gradient, the difference lies with the inhomogeneity in the streamwise direction which leads to boundary layer thickness increasing with x , $\delta(x)$, as well as the wall shear stress not being known a priori, $\tau_w(x)$. Statistics vary primarily in the y direction, and are independent of z . Unlike channel flows, however, the boundary layer continually develops, so that statistics depend both upon x and y . At the free stream the pressure is linked to the velocity through the Bernoulli's equation $p_\infty(x) + \frac{1}{2}\rho U_0 \frac{dU_\infty}{dx} = \text{constant}$ so that the pressure gradient is: $-\frac{dp_\infty}{dx} = \rho U_\infty \frac{dU_\infty}{dx}$

By inspection we can see that accelerating flows $\left(\frac{dU_\infty}{dx} > 0\right)$ correspond to a negative (favorable) pressure gradient. In turn, decelerating flow yields a positive (adverse) pressure gradient, so called because it can lead to separation of the boundary layers from the surface. In this section we focus our attention on the zero-pressure gradient case, corresponding to $U_\infty(x)$ being constant. Then we study the effect of injecting low momentum flow through a porous boundary and its effect on the turbulent structure, since this is a key step on the route to the turbulent fire spread configurations.

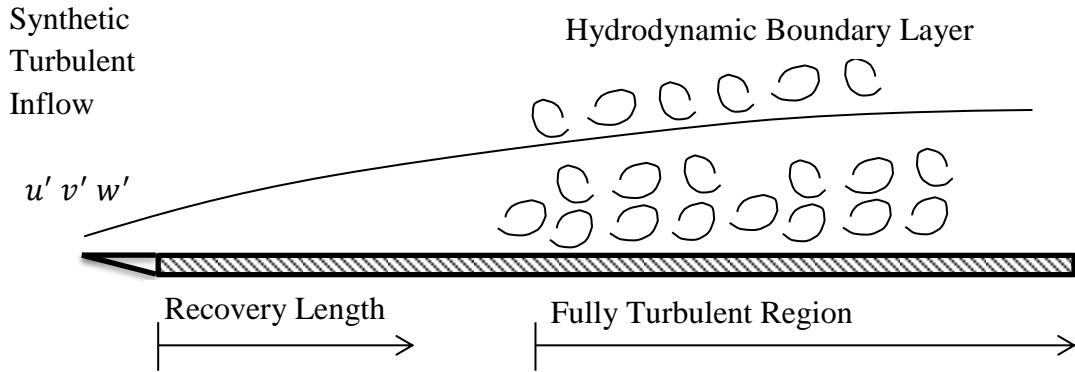


Figure 31. Schematic of turbulent boundary layer configuration showing synthetic turbulent inflow generation and its recovery length preceding a fully turbulent region.

$(L_x L_y L_z)$	$(n_x n_y n_z)$	<i>grid stretching</i>
(600, 25, 25)	(768, 64, 64)	Wall –normal hyperbolic ($\alpha = 2.75$)
<i>Resolution criteria</i> (finite differences)	<i>Turbulence model</i>	<i>Turbulent coefficient</i> <i>Minimization technique</i> (Lily, et al)
$\Delta x^+ \cong 50$ $\Delta z^+ \cong 22$ $y^+ \cong 1$	LES Dynamic eddy viscosity (Smagorinsky type model) $\tau_{ij}^r = -2\nu_t \bar{S}_{ij}$ $= -2C_{ev} \Delta^2 \bar{S}_{ij} \bar{S}_{ij}$	$C_{ev}(x, y, z, t)$ $= -\frac{1 \langle L_{ij} M_{ij} \rangle}{2 \langle M_{ij} M_{ij} \rangle}$ $C_\theta(x, y, z, t)$ $= \frac{\langle K_j T_j \rangle_{avg}}{\langle T_j T_j \rangle_{avg}}$
$Re_{\delta^*} = 1000$	LES Dynamic eddy diffusivity $q_j = -\bar{\rho} C_\theta \frac{\partial \tilde{T}}{\partial x_j}$	Averaging type: Lagrangian
<i>Inflow Boundary</i>	<i>wall boundaries</i>	<i>Periodicity</i>
(Synthetic turbulence) Controlled forcing planes: $\frac{x}{\delta} = (5, 10, 15, 20)$ $\alpha = 1 \beta = 5$ $T_{avg} = 10$	$u_{wall} = v_{wall} = w_{wall} = 0$ $\frac{du_\infty}{dy} = \frac{dw_\infty}{dy} = 0,$ $v_\infty = U_\infty \frac{d\delta^*}{dy}$	Spanwise

Table 9. Physical parameter table for turbulent boundary layer flow configuration. The table presents initial conditions, boundary conditions, controller and turbulence models.

4.3.1 Turbulent Recovery Length

A turbulent simulation was carried out employing the synthetic turbulent inflow technique of Batten to investigate the boundary layer of interest. The computational domain selected has length units of 600, 25, 25 in the streamwise, wall normal and spanwise directions with viscous resolution of $\Delta x^+ \sim 50$, $\Delta z^+ \sim 20$, and $y^+ \sim 1$ at the wall to ensure that the range of turbulent scales are correctly represented by the grid. Similar to turbulent channel flow problems, a dynamic Smagorinsky Large-eddy simulation (LES) technique was utilized as the turbulence model with Lagrangian averaging of the dynamic coefficient. Due to the introduction of spatial development along the streamwise direction, the flow is now considered homogenous only in the spanwise directions. Thus, the periodicity condition is now only applied in the spanwise direction and inflow/outflow conditions must be accurately modeled (for details on synthetic turbulent inflow and Oralsnky outflow resfer t o Chapter 2 section 2.11).

The reference scales utilized correspond to a Reynolds number constructed with the displacement thickness, δ equal 1 cm, $\delta = \int \left(1 - \frac{\rho u}{\rho_\infty u_\infty}\right) dy$ as a length-scale, free stream velocity $U_\infty = 1 \frac{m}{s}$ as a velocity scale, with reference viscosity $\nu_{ref} = 10^{-5} \frac{m^2}{s}$, yielding $Re_\delta = \frac{U_\infty \delta}{\nu_{ref}} = 1000$. The simulation is run for a total of 10 flow-through times and sampling of the turbulent fields begins after the initial transients are removed. The sampling frequency used for statistics is 10 per *LETOT*, computed based on the large-eddy turnover time as the relevant convective time scale $LETOT \sim \delta/u_\tau$.

The turbulent recovery length is captured by monitoring the skin friction coefficient as is commonly suggested in the literature [ref]. Skin friction, $C_f = \frac{\tau_w}{\frac{1}{2}\rho_\infty U_\infty}$, is a good indicator of mixing development, together with iso-contours of Q it can be used to measure when the turbulence reaches its natural state. Figure 28 and 29 show that the recovery length is $\sim 100\delta$.

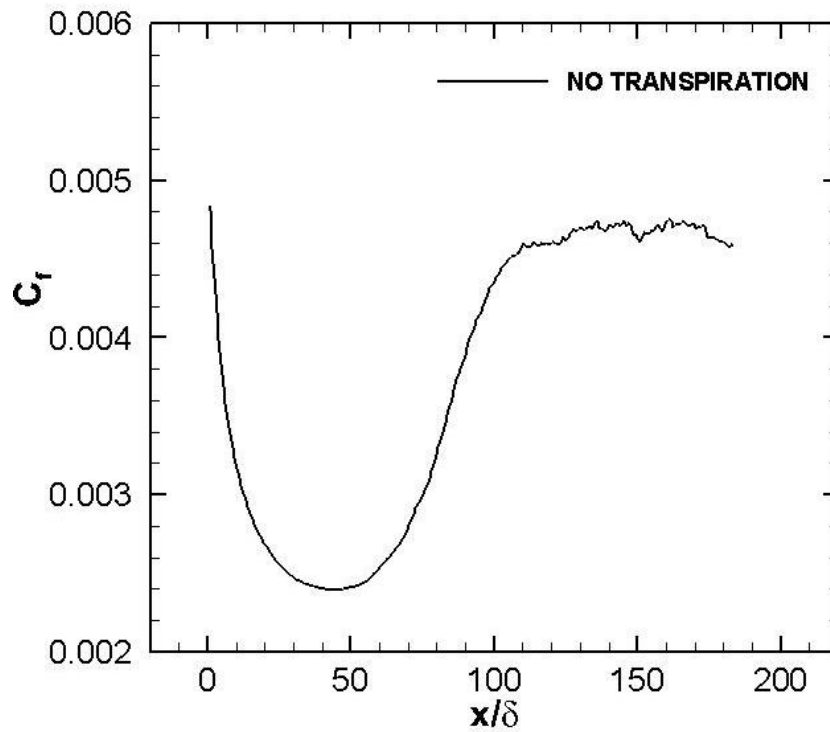


Figure 32. Spatial development of mean skin-friction coefficient to evaluate the recovery length; simulation performed for a reference case with no transpiration.

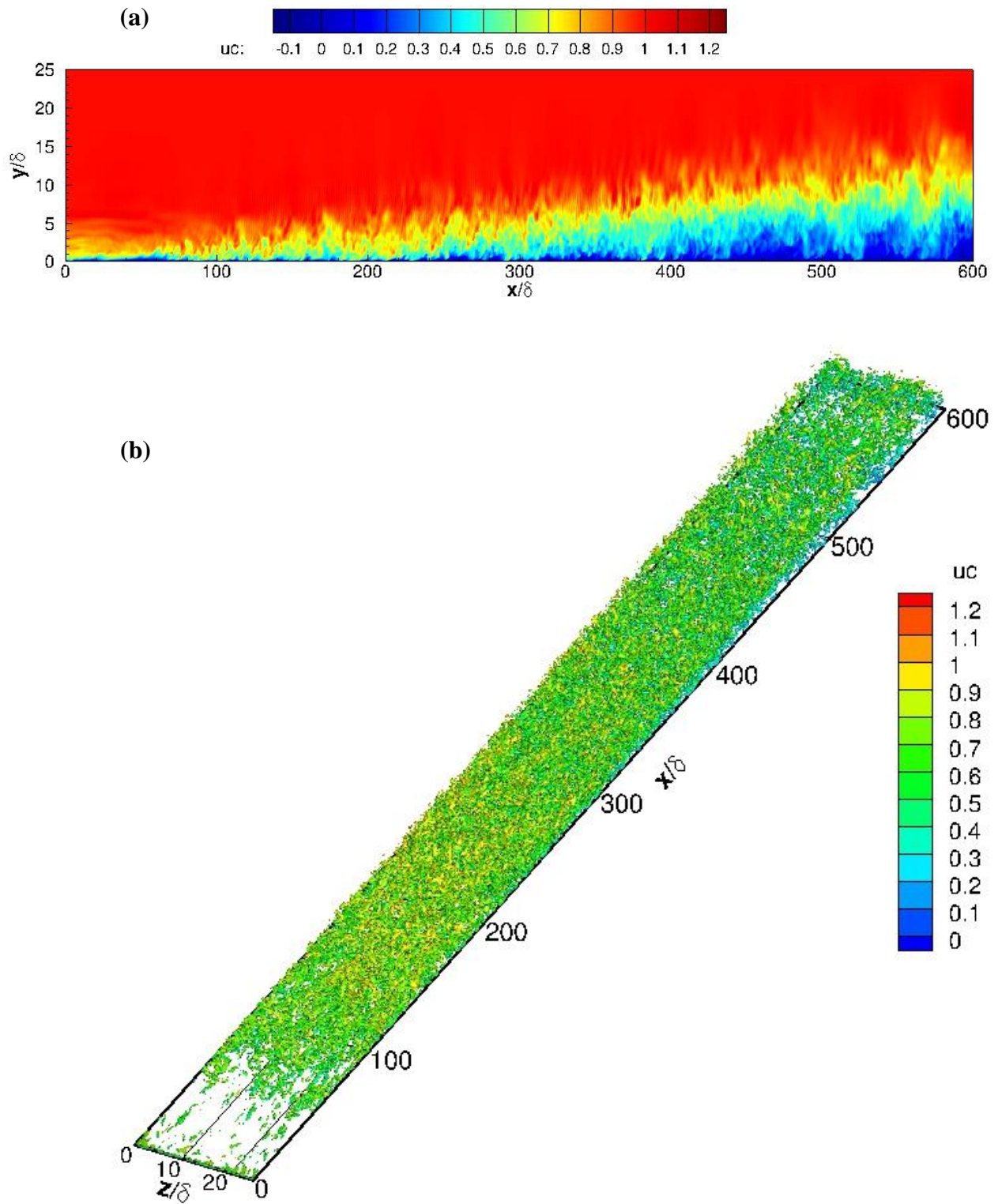


Figure 33. Instantaneous visualization of turbulent structures via (a) iso-contours of velocity and (b) iso-contour of Q colored by streamwise velocity.

4.4 The Effect of Transpiration through a Porous Surface

In this section, we are interested in practical issues such as wall transpiration for cooling or fuel injection purposes, and we want to evaluate the ability of the code to handling this complex configuration. We consider the effects of transpiration from the particular point of view of its effect on the turbulence structure and focus on the interaction of turbulence with transpiration. As was shown in the previous section, the turbulent redevelopment length was found to be 100δ from the synthetic inflow. This is the minimum length required for redevelopment and it is closely tied to computational time. Thus to ensure proper redevelopment of the flow to its natural state, the injection zone region was selected as $200 < \frac{x}{\delta} < 550$ (adding an additional 100δ buffer zone) with a blowing magnitude of 1% of the freestream velocity, U_∞ (Figure 30a). The same conditions as the previous boundary layer test case is used ($Re_\delta = 1000$) with the same computation domain and resolution criteria.

As shown in Figure 30b the low momentum injection of air through porous boundary significantly affects the boundary layer downstream of the injection point as is demonstrated though mean skin-friction profiles. This sharp decrease is due to the change in shear stress distribution rising from increased thickness of the sublayer and its strong effect on the velocity profiles. The effect of uniform blowing on the spatial development of the flow is to thicken the boundary layer (while suction would thin it), and the magnitude of this effect depends on the amplitude of the blowing. Also shown in Figure 30 is a comparison to the case without transpiration and to integral analysis theory derived for this type of case by Kays et al [77]. The equation is written as a function of a

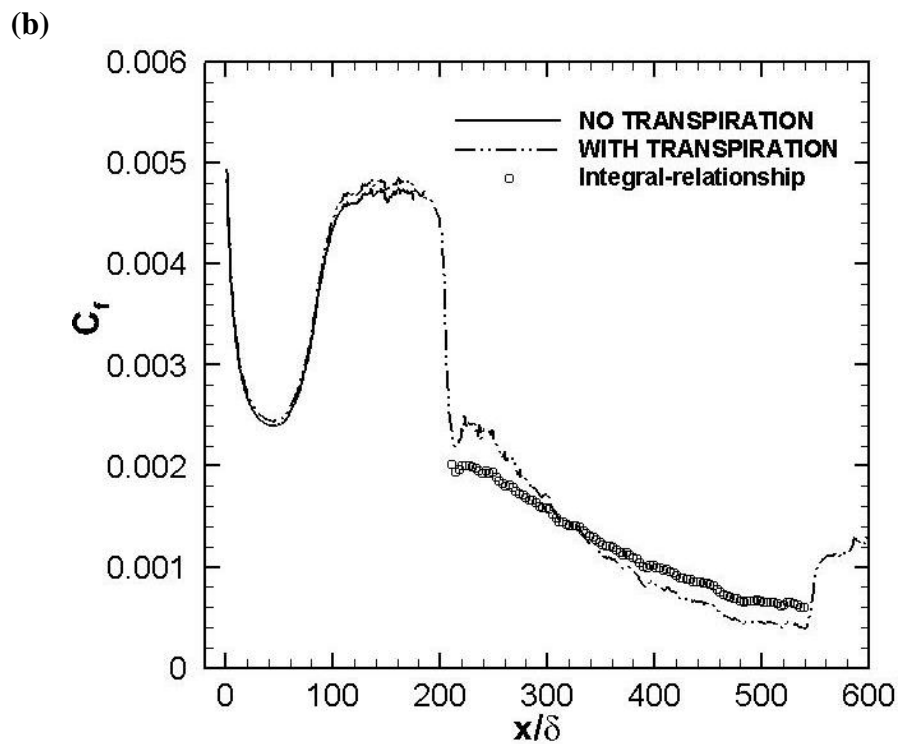
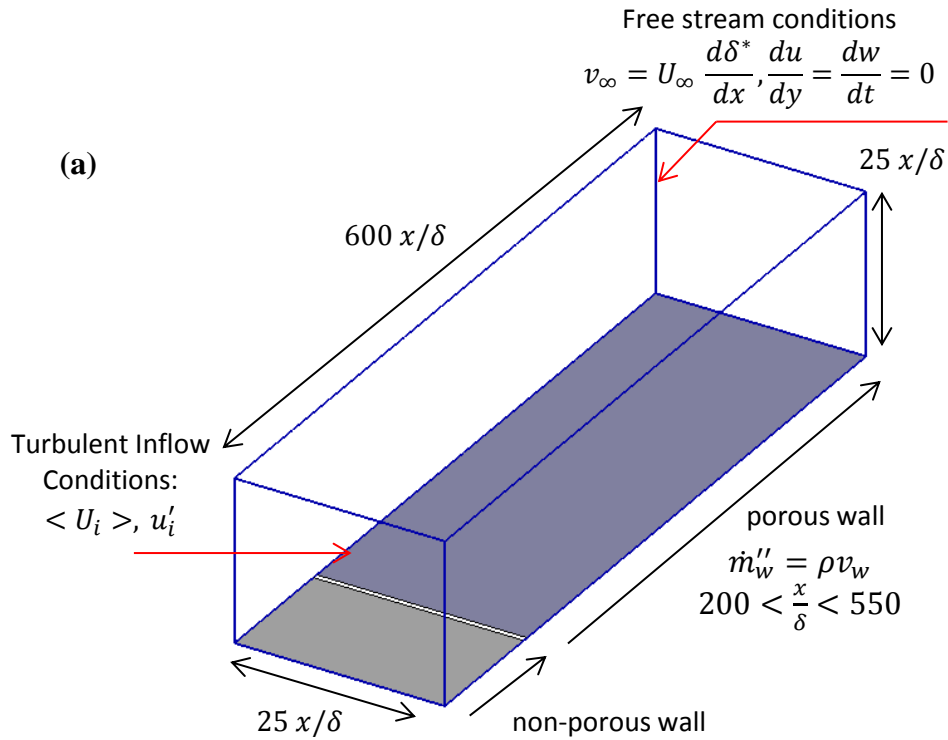


Figure 34. Transpired turbulent boundary layer (a) schematic , (b) Spatial development of mean skin-friction coefficient to evaluate the recovery length; compared to a full-scale configuration where blowing is specified through the wall beginning at $x=200$; comparison to an integral relationship.

blowing parameter $B_f = \frac{v_{wall}u_{\infty}\rho}{\tau_{wall}} = \frac{v_{wall}/u_{\infty}}{C_f/2}$ and shows good agreement with our present results. The equations for the non-transpired and transpired cases derived are as follows:

$$\left(\frac{C_f}{2}\right) = 0.0287Re_x^{-0.2} \quad (86)$$

$$\left(\frac{C_f}{2}\right) = 0.0287 \frac{\ln[1 + B_f]}{B_f} Re_x^{-0.2} \quad (87)$$

Mean profiles of streamwise velocity are compared at several locations downstream (corresponding to Re_{δ}) and compared to the case with an impermeable wall. One important feature of turbulent boundary layers with no blowing is the collapse of the velocity and intensity profiles along the streamwise direction when normalized and plotted in viscous units. This is called the self-similarity condition which is successfully retrieved and demonstrated in Figure 31-32. A prominent feature of the transpired boundary layer can be seen from the mean velocity profiles in Figure 31 (a), the self-similarity now holds only in the inner layer and the velocity magnitude in the outer layer increases with downstream location.

The increase in velocity magnitude in the outer layer is a direct effect of the behavior of the skin friction coefficient in the transpired region, see Figure 30 and Figure 31. Also shown in Figure 31 is the dependence of the freestream mean velocity value on the streamwise direction, that is due to the local non-dimensionalization. Furthermore, an increase in turbulence intensity (magnitude) is directly observed for all kinematic components, as well as a shift in turbulent structure to the outer layer. This shift occurs as a result of the low momentum fluid injected through the wall pushing away the fluctuations which ultimately affects all boundary layer properties such as δ , θ and H .

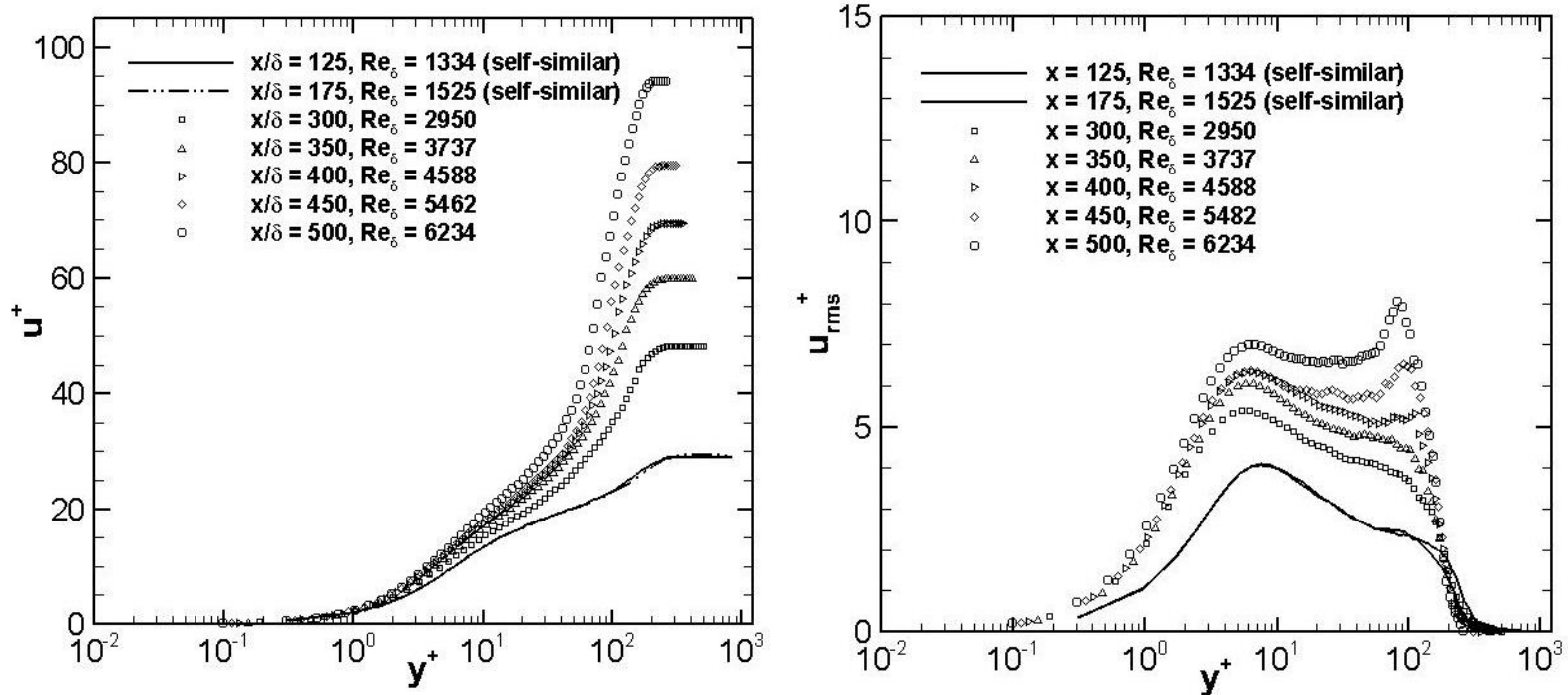


Figure 35. First and second order statistical analysis: Effect of mass-transfer -- gas-injection -- in (a) normalized mean velocity profiles and (b) u -turbulence intensity profiles ; normalization in viscous wall-units.

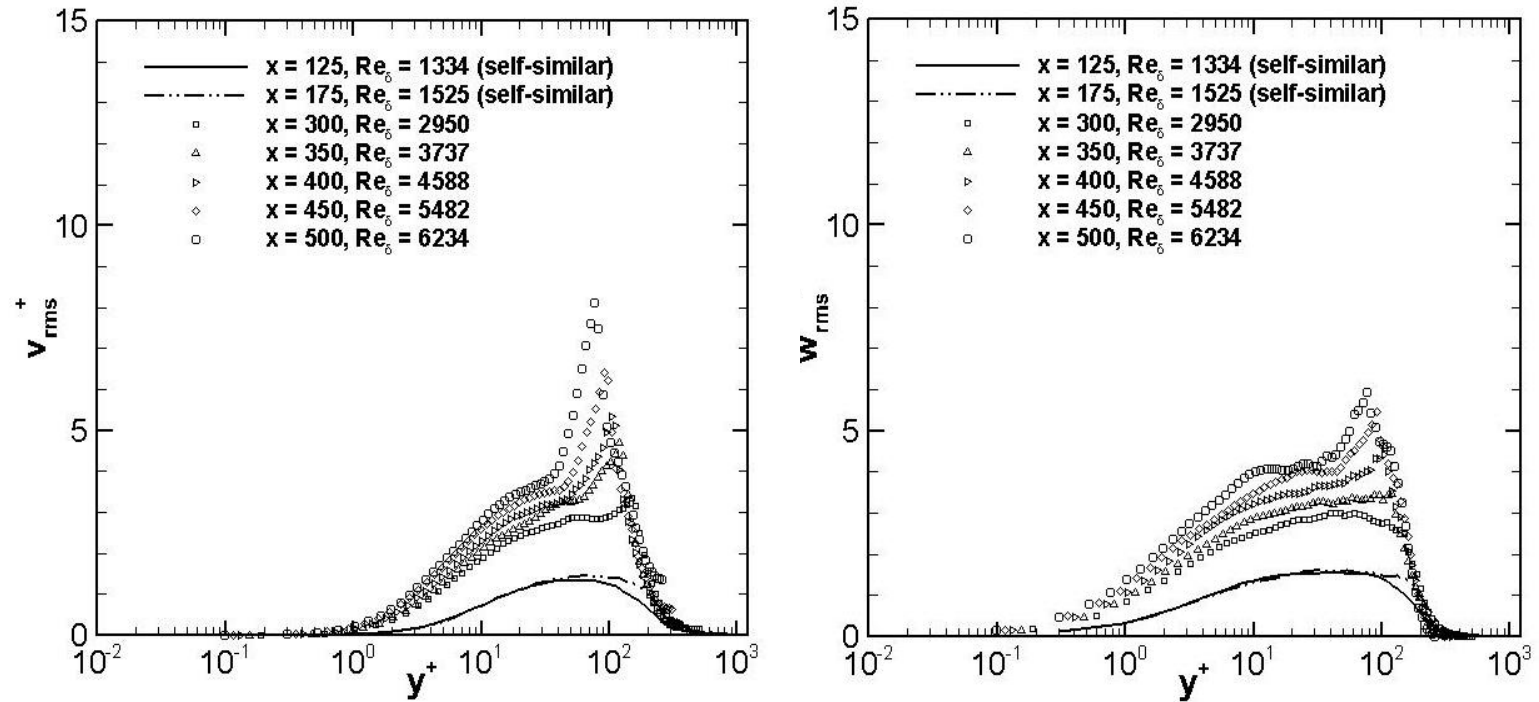


Figure 36. Second order statistical analysis: Effect of mass-transfer -- gas-injection -- in (a) wall-normal turbulence intensity profiles and (b) spanwise turbulence intensity profiles ; normalization in viscous wall-units.

4.4 *Summary*

This Chapter has been devoted to validating the solver for several challenging configurations that are relevant to problems in turbulence, heat transfer, and mass transfer. These are important components that come together when modeling flame combustion dynamics as in the case of turbulent flame spread. Turbulence benchmarking has been made with reference DNS results found in the literature of turbulent channel flow configurations using wall-resolved large eddy simulation model. The results are in good qualitative and quantitative agreement with the benchmark data and provide confidence in the ability of our modeling technique. Results from the turbulent boundary layer with surface transpiration compares well with analytical integral relationships for the skin friction coefficient. Furthermore, when normalizing the turbulent data with inner wall variables the profile collapse smoothly in the non-blowing region showing correct behavior of the flow. The effect of mass-transfer (surface transpiration) is seen to increase the mean velocity and intensity profiles in wall-units as a result of the decreased wall velocity gradients (skin friction) in the blowing region.

Chapter 5: Turbulent Wall-fires

The ability to accurately predict fire spread is an important topic in the area of fire-safety and building code development since it controls the rate of heat release rate and fire growth. In 2011 there has been a total of 1,390,00 reported fire incidents, with home structures accounting for 27% of the reported fires causing the majority 84% of all civilian deaths [78]. Although the history of reported incident/losses has been steadily decreasing it is still a major concern for property loss, human injury and death. The total cost of fire in the United States is estimated to be at \$331 billion dollars or 2.3% of the US gross domestic product for 2009 [79]. This cost estimate includes human losses (lives lost, medical treatment, pain and suffering) and economic losses (property damage, business interruption); and the cost of provision to prevent or mitigate the cost of fire (insurance, fire protection equipment and construction). Thus the motivation for continued research in fire will continue to grow in the community with a strong emphasis on CFD based fire-modeling to handle the range of challenging problems from forensic fire investigation to key fundamental research.

Previous studies have focused on upward flame spread over flammable surfaces. Much attention has been devoted to solid polymeric materials such as polymethyl methacrylate (PMMA) due to its wide use in residential homes and buildings. For small laminar flames, the spread rate from theory and experiment for thermally thick solids follow a $x_p \sim t^2$ power law. However as the size of the fire increases and the flow transitions to turbulence, x_p increases exponentially with time [80]. The spread velocity is generally described by V_p proportional to $(x_p - x_b)^n$ where n is reported to vary from 0.5-0.7 for turbulent conditions over textile materials, and for thick PMMA under

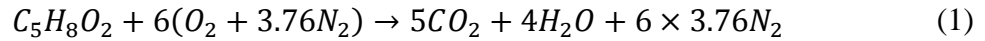
turbulent conditions n is approximately equal to 1. In moderate sized vertical fires ($x_f < 1.4$) the flame heat flux ahead of the pyrolysis region has been found to be $q_f'' = 25 \text{ kW/m}^2$ and approximately independent of the material [81]. A related configuration of practical interest is the horizontal flame spread subject to external flow conditions. A turbulent flow study by Zhou *et al.* [49], [51], [82] has been conducted for ceiling and floor mounted PMMA (0.3 m in length) with a range of flow speed from 0.25 to 4.5 m/s with turbulent intensities 1 percent to 15 percent. It was found that the spread rate is steady at a given flow, but soon increases with flow speed. At larger scales, such as the case studied by Apte *et al.* [83] radiation and buoyancy effects become more important, especially for floor spreading rates. Fire spread measurements were conducted over horizontal PMMA surfaces exposed to air flows ranging from 1 to 2.1 m/s in a 2.4 by 5.4 m wind-tunnel. A simple flame length correlation of $x_f = 1.25 x_p$ is found to be a good fit over the entire range of the burning characteristics [83].

Numerical modeling (CFD) efforts in the burning behavior and fire spread characteristics of PMMA have included the works of by Consalvi *et al.* [84] and Xie *et al.* [85]. Consalvi's configuration studied pyrolysis heights up to 0.6 m and looked at the details of the heating process in upward flame spread over thick solids. His model results agreed well with the data on the pyrolysis front trajectory and heat release rate per unit width, \dot{Q}' , as a function of x_p . Xie *et al.* developed a reaction progress variable based embedded flame model to efficiently compute flame heat flux to the surface in his simulation obtaining excellent agreement with experiments for the prediction of flame spread rate and pyrolysis front. The principal focus for much of the work will be to highlight and demonstrate the ability of les3d-mp to handle the challenging wall-flame

problem addressed by various researchers. Comparisons will be made to the horizontal flame spread case studied experimentally by Zhou *et al.* [49], [51], [82] in terms of the flame-length under several flow conditions as part of a validation study.

5.1 Gas-Phase Combustion Model (PMMA)

The combustion model uses a global combustion equation with polymethyl methacrylate (PMMA) as the fuel:



The mixture composition is described in terms of MMA, oxygen, carbon dioxide, water vapor and nitrogen. Assuming infinitely fast chemistry, and using the classical Burke-Schumann state relationships, the mixture composition is a function of mixture fraction. Thermodynamic properties (i.e., enthalpy of formation and heat capacities at different temperatures) of oxygen, carbon dioxide, water vapor and nitrogen are obtained from CHEMKIN databases. Thermodynamic properties of PMMA are not known with accuracy and a simplified model is adopted: the heat capacity of PMMA is assumed constant and equal to $c_p = 1.26 \text{ kJ/kg/K}$; the enthalpy of formation of PMMA is then calibrated so that the heat of combustion of PMMA is $\Delta H_c = 25 \text{ MJ/kg}$ (the adiabatic flame temperature for PMMA-air combustion is then $T_{ad} = 2442 \text{ K}$); we use $\Delta H_f = -4.34 \text{ MJ/kg}$. Figure 32 presents calibration results using the mixture fraction combustion model and its comparison with the Burke-Schumann model; it also depicts the effect of variable specific heats in the model. Lastly, species mass fractions are reconstructed using chemical state relationships showing the mixture composition.

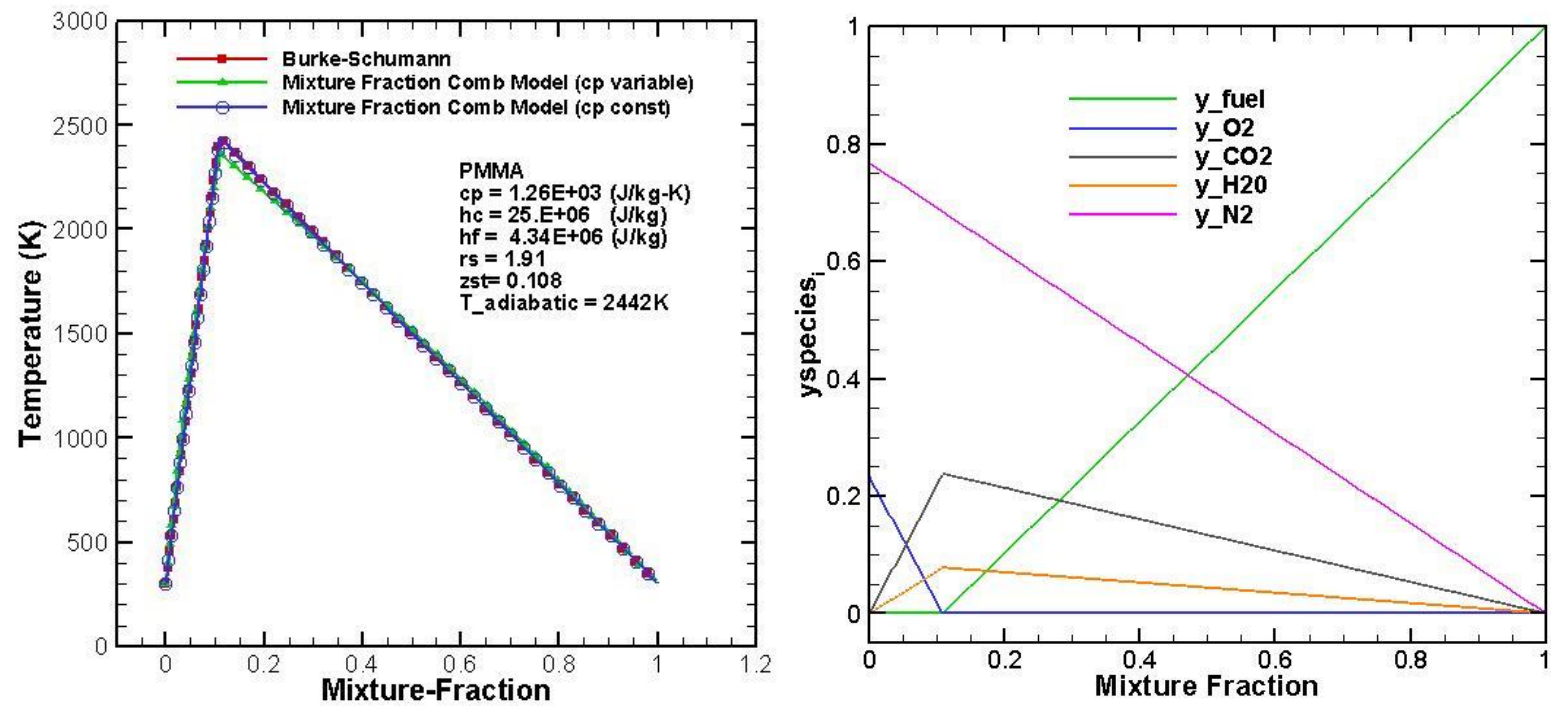


Figure 37. (a) Calibration of the mixture fraction combustion model with Burke-Schumann solution with constant specific heat (PMMA), (b) mapping of species mass fraction with mixture fraction and chemical state relationships.

5.2 Numerical Configuration

The numerical configuration corresponds to a turbulent wall-flame fueled by thermally degrading PMMA and ventilated by a cross-stream of air; this configuration was previously studied experimentally at the University of California at Berkeley [49], [51], [82]. The simulation was performed in a domain of length 40δ , width 8δ , and height 8δ , where $\delta = 1\text{ cm}$ is the measured integral length-scale of the incoming turbulent flow. The mean flow velocity is $U_\infty = 2\text{ m/s}$ and the Reynolds number based on the integral length-scale and the mean flow velocity is $Re = 1212$. The size of the computational grid is $256 \times 96 \times 48$ points in the streamwise, wall-normal and spanwise directions and corresponds to $\Delta x = \Delta y = \Delta z = 1.5\text{ mm}$ at the center of the domain. A smooth hyperbolic tangent function was used in the wall-normal direction to efficiently cluster the grid nodes near the wall, $\Delta y_{min} = 0.04\delta = 0.4\text{ mm}$. Grid convergence tests have shown that this level of grid resolution is adequate to resolve most effects due to turbulent fluctuations ($(v_t/v_{mol}) \sim 0.01$) as well as the wall gradients; therefore, while performed using a large eddy simulation framework (see Chapter 2), the simulations are close to achieving direct numerical simulation (DNS) quality and are considered hereafter as (slightly coarse) DNS.

A synthetic turbulence inflow method due to Batten *et al.* [30] is used to prescribe turbulent inflow conditions. This technique requires the specification of a time scale of turbulence τ_b calculated from the turbulent kinetic energy k , and the turbulent dissipation rate ϵ . Several controlled forcing planes are introduced to match target profiles for the Reynolds shears stresses (for isotropic turbulence $\langle u'v' \rangle = 0$). The technique

introduces a forcing term in the wall-normal momentum equation that amplifies the velocity fluctuations in that direction. The outflow boundary condition is prescribed through a hyperbolic convective equation based on a mean convective velocity. At the wall, fuel injection is specified using a mixed convective-diffusive boundary conditions,

$$\dot{m}_w'' = \dot{m}_w'' Z_w - \rho_w D_w \left(\frac{\partial Z}{\partial y} \right)_w \quad (2)$$

where \dot{m}_w'' is the PMMA mass flow rate per unit wall surface area. \dot{m}_w'' is specified based on experimental data; the simulation corresponds to a fuel injection region (the pyrolysis region) that is 4 cm wide, $10\delta < x_p < 14\delta$. The upstream region of the pyrolysis zone ($0 < x < 10\delta$) is described with a slip-wall condition, so that the boundary layer starts growing at the edge of the pyrolysis region. The wall thermal boundary condition is a critical issue that needs to be treated accurately if one wants to simulate the variations of the wall heat flux; the present simulations are performed using a crude model in which the wall is assumed to be isothermal at 300 K; work is in progress to remove this simplification and to implement a more elaborate description of the wall surface temperatures. The simulation is allowed to run for several convective time scales and statistics are taken by sampling over 10 time scales.

The experimental configuration corresponds to a momentum-driven PMMA-fueled wall flame characterized by different cross-flow air velocities and different turbulent intensities. The air cross-flow is produced by a wind-tunnel testing facility providing controlled grid-generated quasi-isotropic turbulence. Figure 34a presents a comparison between the streamwise variations of the measured and simulated turbulence

intensity (the test section in this plot correspond to values of x between 10 and 40 cm); the simulated variations for the case of a turbulence intensity of 5% are in good agreement with experimental data; the simulations confirm the experimental observation that the turbulence decay in the test section is slow and that the turbulence intensity can be considered as approximately constant. Figure 34b presents the streamwise variations of turbulent kinetic energy in a log-log plot; the simulation results agree with the classical power law decay law: $k/U_\infty^2 = (x - x_o/M)^{-n}$ with $n = 1.2$ and $x_o = 0$ where x_o is the virtual origin and M is the experimental mesh spacing [16]. Experimental mesh spacing used by Zhou ranged in values from 0.5 to 1.5 cm and set the flow's integral length scales [49].

Note that the experimental configuration corresponds to a full flame spread problem in which the PMMA slab is first ignited at the leading (upstream) edge and the pyrolysis region and associated wall flame are subsequently allowed to spread downstream and consume the entire PMMA sample. In the experiments, the size and location of the pyrolysis region and wall flame are time-dependent properties. We adopt in the present study a quasi-steady view point: we neglect the spreading properties of the pyrolysis/flame region, assume that the pyrolysis region has a constant width of $x_p = 4$ cm, and compare the simulation results to experimental data taken at the moment when $x_p = 4$ cm.

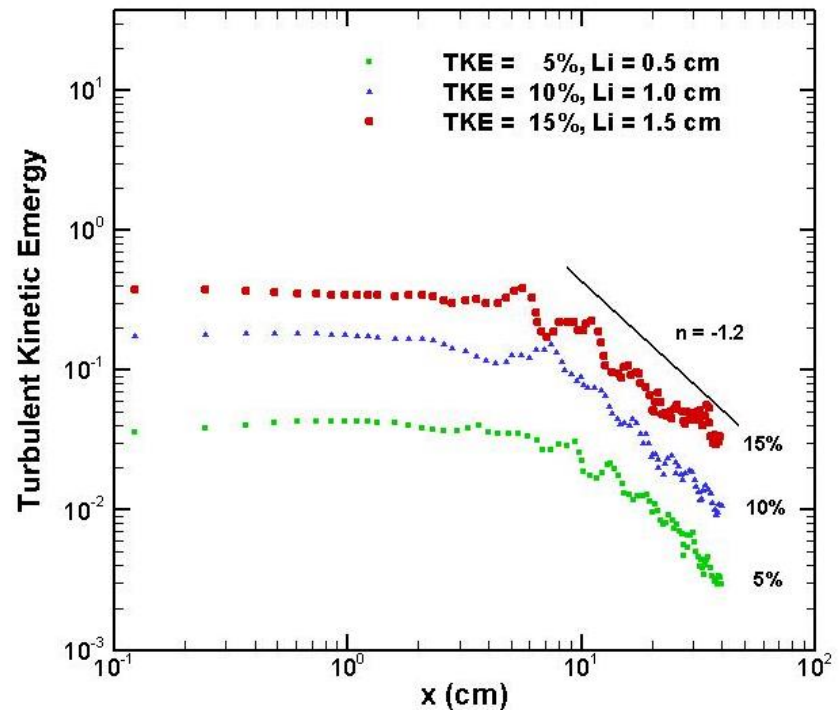
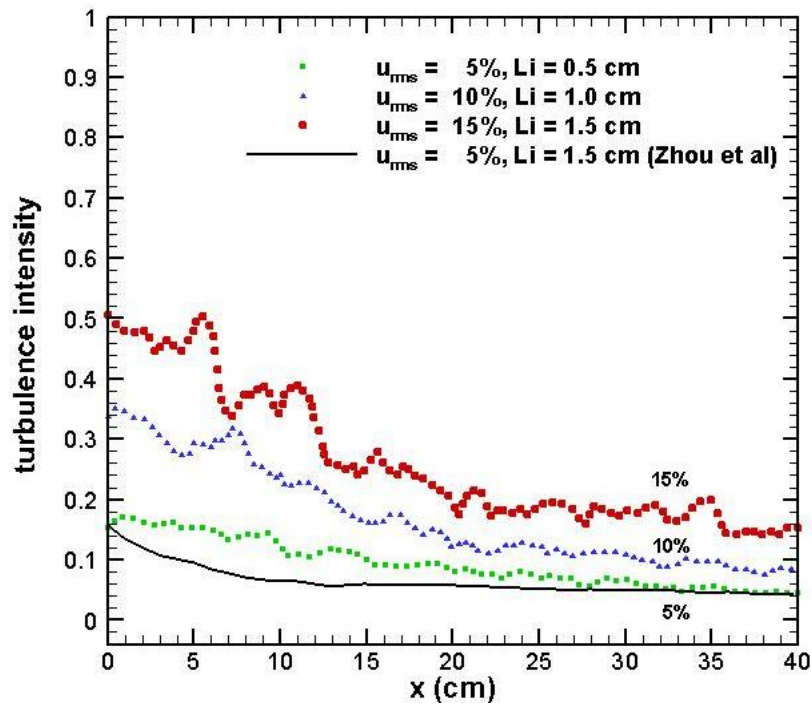


Figure 38. 2nd order statistical analysis: (a) Spatial variation of turbulence intensity profiles featuring weak-to-moderate intensity levels; solid line represents experimental data of Zhou et al. (b) turbulent kinetic energy variations plotted in log-log coordinates showing a power law rate of decay coefficient ($n=1.2$)

5.3 Wall-flame results

Figure 35 presents a three-dimensional visual representation of the configuration. It shows an instantaneous snapshot of the flame surface as it develops in the direction of the flow subject to turbulent perturbations. This snapshot corresponds to a weakly turbulent level of 5%.

Figure 36 and Figure 37 presents time/spatial averages of mixture fraction and temperature iso-contours for the case of $U_\infty = 2 \text{ m/s}$ at a turbulent intensity level $I = 5\%$ and 15% . The diffusion flame is observed to develop along the wall; conditions are only weakly turbulent and controlled by the momentum of the inflow.

The mixture fraction variations presented in Figures 35a & 36a clearly show the location and width of the pyrolysis region, as well as the downstream mixing of the fuel. The flame is identified as the iso-surface where mixture fraction is equal to its stoichiometric value, $z_f = 0.108$; the flame envelope is depicted in Figure 36b and 37d by a solid line. The flame is shorter for $I = 15\%$, which may be explained by enhanced fuel-air mixing due to turbulence. Note that in the simulations, the flame length is reduced by 6 cm when going from $I = 5\%$ to $I = 15\%$; in comparison, in the experiments, the change in flame size is estimated to be 4 cm. Also, the maximum gas temperature is reduced for $I = 15\%$; this may be explained by enhanced flame-wall interactions that lead in turn to higher thermal losses to the cold wall. This issue will be re-visited once a more elaborate wall temperature model is implemented.

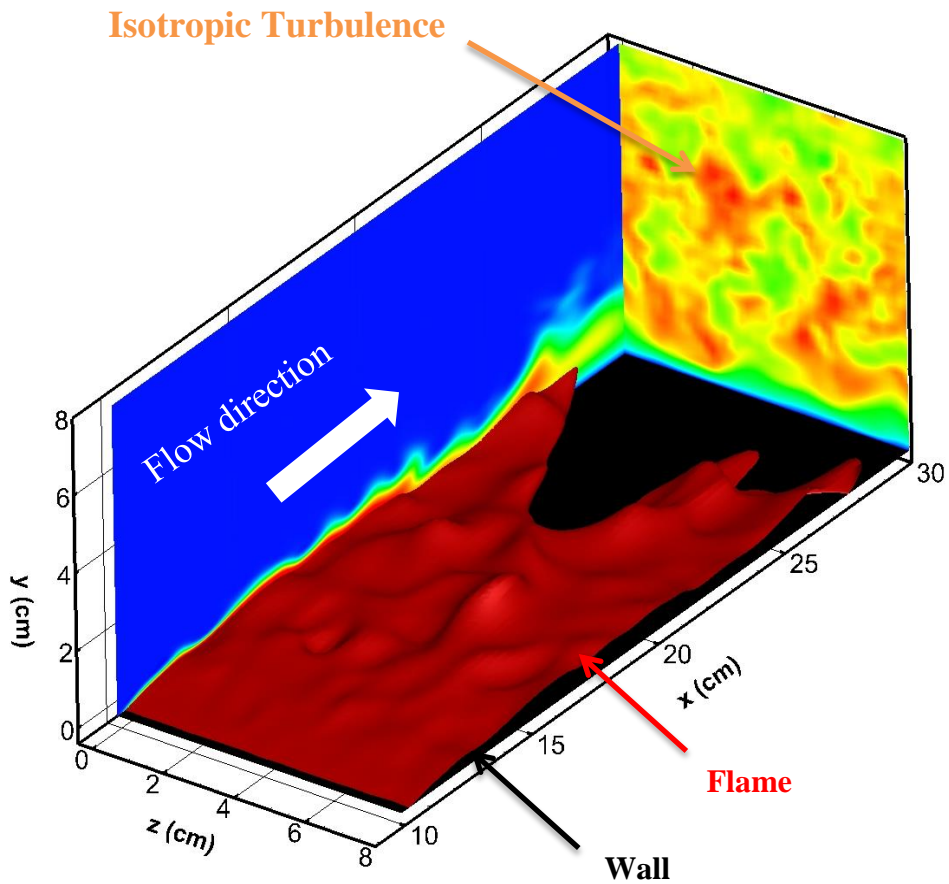


Figure 39. Large-eddy simulation of turbulent non-premixed wall-flame subject to isotropic turbulence perturbations at $I = 5\%$ intensity level. Flame location is identified as an iso-surface of stoichiometric mixture fraction, $z_f = 0.108$ for polymethyl methacrylate fuel. The pyrolysis products originate from a small burning region at the wall with length $x_p = 4 \text{ cm}$ beginning at $x = 10 \text{ cm}$.

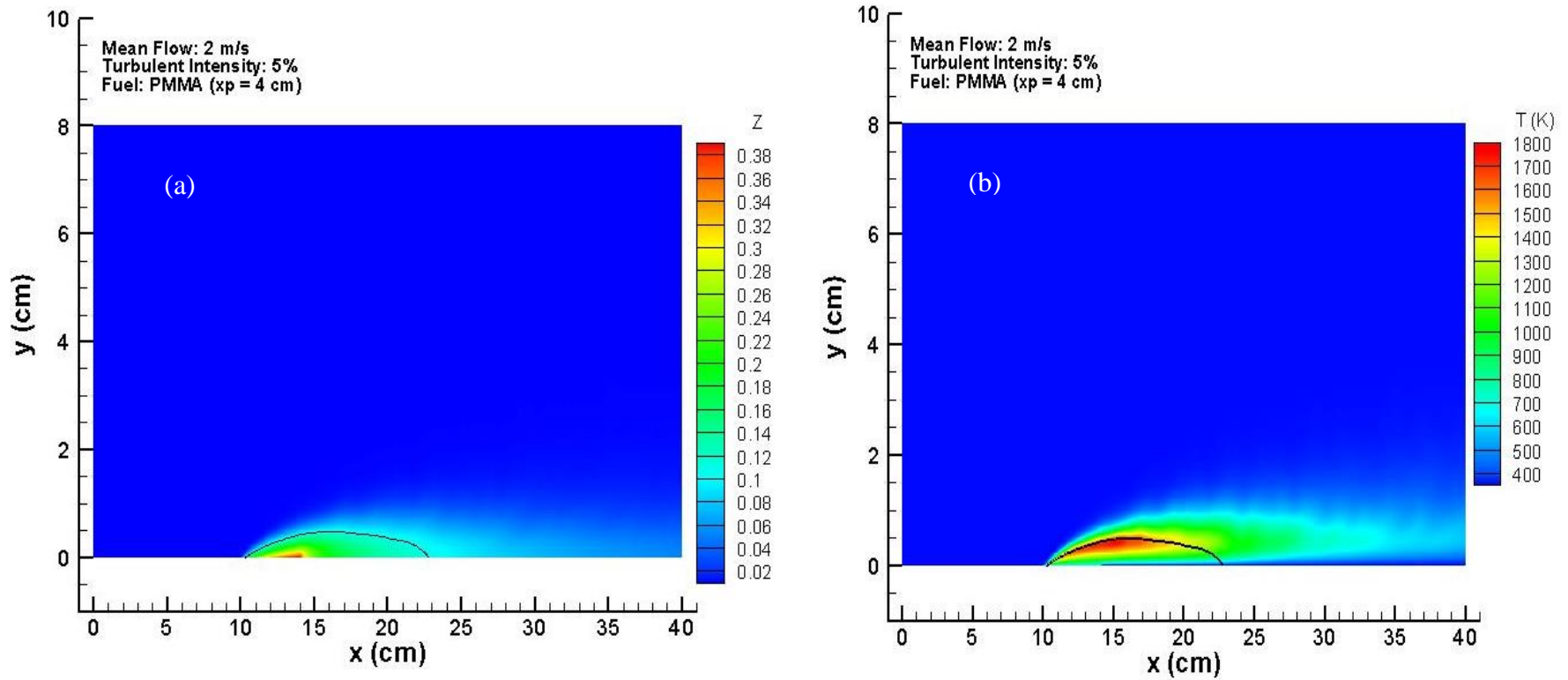


Figure 40. Averaged contours of: (a) mixture fraction and (b) temperature for turbulent intensity $I = 5\%$; note that the flame length is identified by a solid black line (stoichiometric mixture fraction value) $x_f = 10$ cm

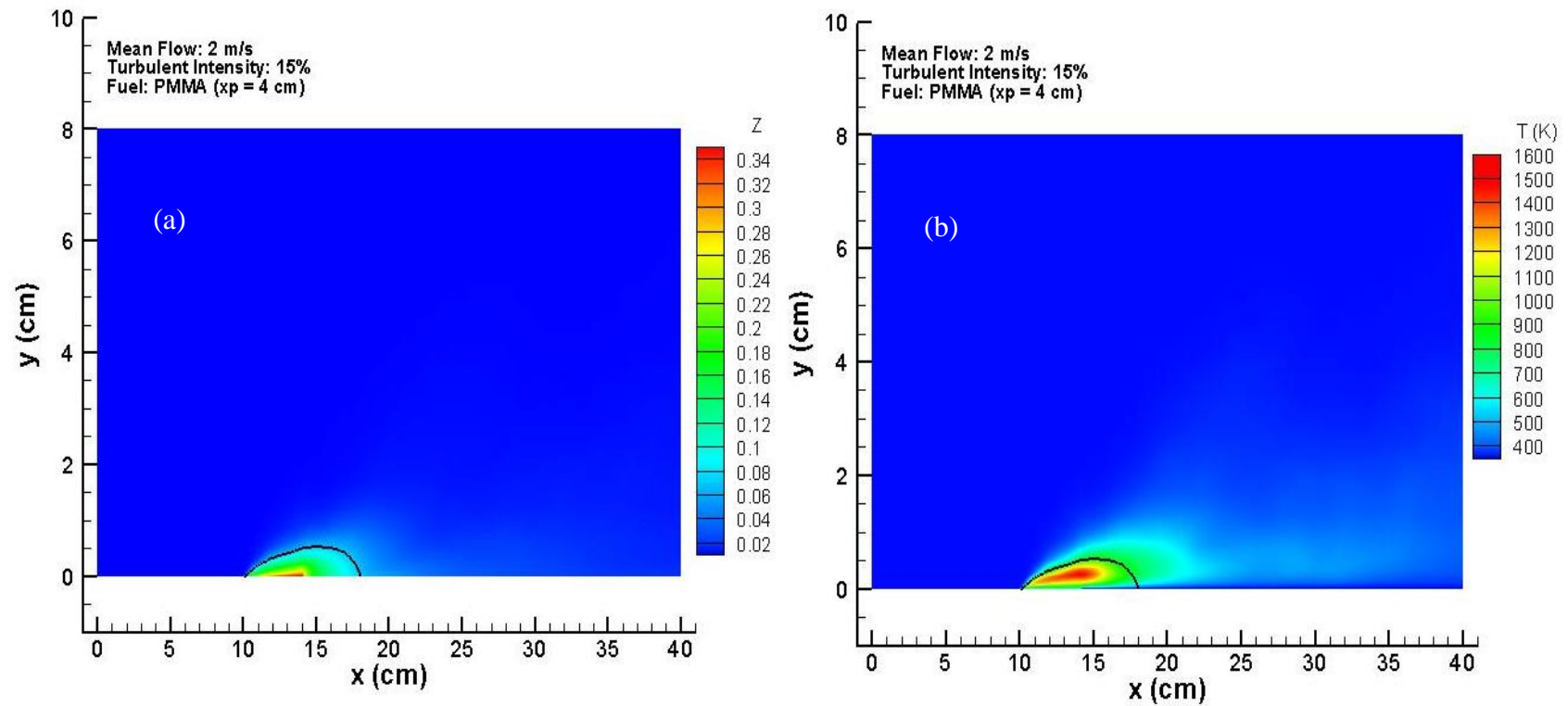


Figure 41. Averaged contours of: (a) mixture fraction and (b) temperature for turbulent intensity $I = 15\%$; note that the flame length is identified by a solid black line (stoichiometric mixture fraction value) $x_f = 4$ cm

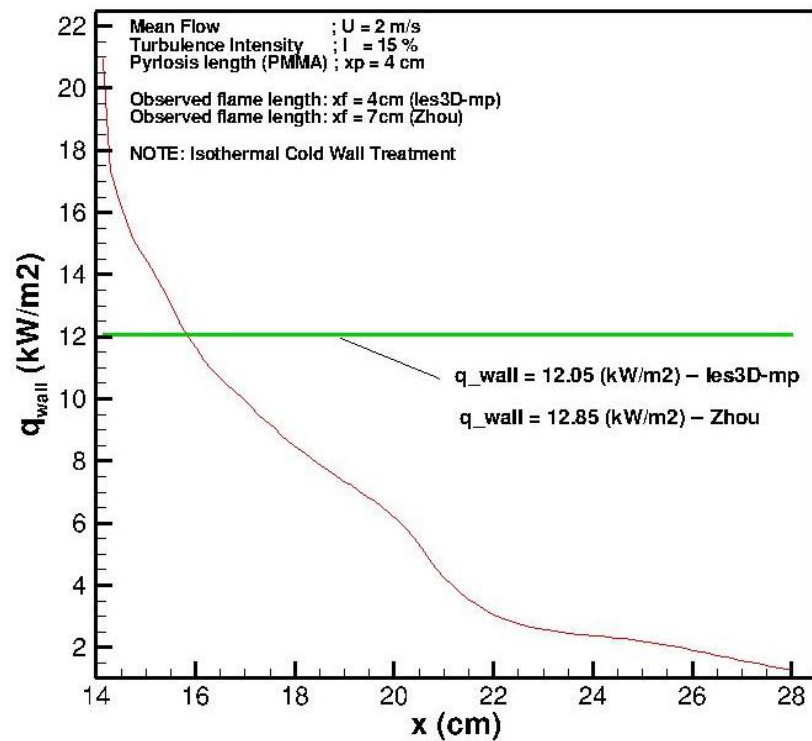
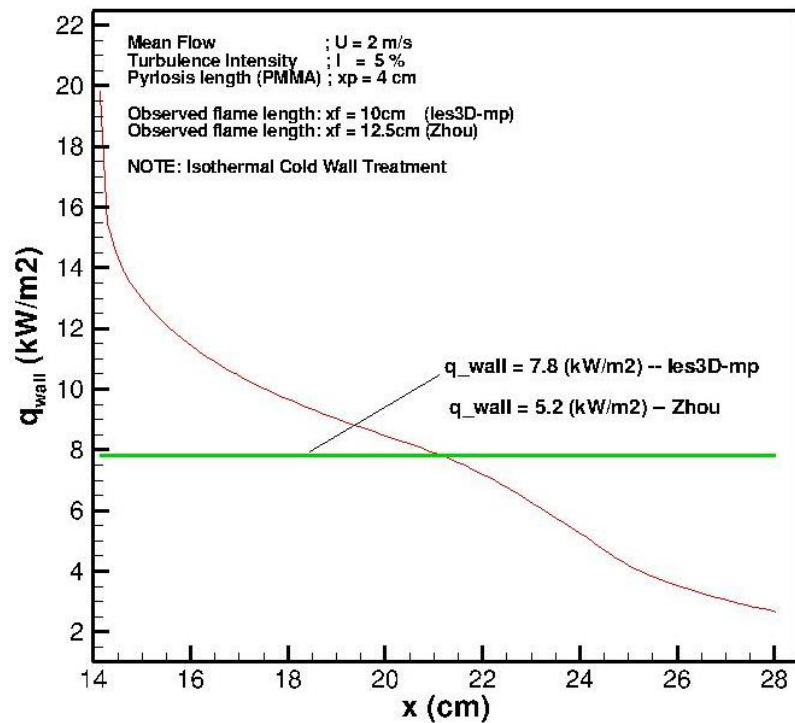


Figure 43. Average profiles of surface heat flux in the flame region: (a) spatial and averaged value of heat flux for $I = 5\%$, (b) spatial and averaged value of heat flux for $I = 15\%$.

Figure 38 shows profiles of mean surface heat flux along the length of the flame length region for both $I = 5\%$ and $I = 15\%$ test cases. An averaged value of each profile is calculated (within the flame envelope) and compared to the measurements by Zhou et al. Note that the flame length for each case is: $x_f = 10\text{ cm}$ ($I = 15\%$) and $x_f = 4\text{ cm}$ ($I = 5\%$); this decrease in flame length is accompanied by an increase in surface heat flux due to the stronger interaction between flame and the wall.

5.4 Summary

The results in this chapter are aimed at validating an in-house Computational Fluid Dynamics (CFD) solver developed for high-resolution numerical simulations of boundary layer combustion. The study considers a simple non-premixed wall flame configuration in which the fuel corresponds to pyrolysis products supplied by a thermally-degrading flat sample of polymethyl methacrylate (PMMA) and the oxidizer corresponds to a cross-flow of ambient air with controlled mean velocity and turbulence properties. This configuration was previously studied experimentally at the University of California at Berkeley [49], [51], [82]; the air cross-flow features moderate turbulence levels, i.e. a free stream velocity of 2 m/s and turbulence intensities between 5 and 15%. Comparisons between numerical results and experimental data are made in terms of flame structure, flame length and surface heat flux. The comparisons are encouraging but remain qualitative. Quantitative comparisons in terms of wall heat flux are in progress; these comparisons require a detailed description of the wall surface temperature based on a solution of the heat transfer processes taking place inside the solid wall.

Chapter 6: Conclusions and Future Work

6.1 Conclusions

A CFD-based fire modeling tool has been developed and introduced as part of this PhD work to study problems relating to turbulent fire spread over flammable/non-flammable solids. An introduction to the fire modeling field has been presented in Chapter 1 highlighting the technical challenges and the current state of the art in the field, and introduction to turbulence modeling field has also been emphasized as it is relevant to this research topic. This work also seeks to contribute to the state of the art in modeling boundary layer combustion problems by introducing the numerical framework to handle reacting flows, turbulence models, and a suite of validation studies, in boundary layer configurations.

6.2 Key Contributions

1. An advanced CFD based fire modeling tool has been introduced by adapting a preexisting numerical simulation solver from a boundary layer flow code to a code with variable mass density and combustion capabilities. The solver extends the present state of the art in fire modeling (limited to laminar flows) by providing a high quality numerical tool to study the heat transfer aspects of turbulent wall flame phenomena. In addition, and to the author's knowledge, this work provides the first LES computational study of horizontal flame spread in the open literature.

2. Key verification studies have been conducted where the mathematical consistency of the numerical equations developed have been rigorously examined. Two canonical configurations have been devised corresponding to an isothermal one-dimensional binary mixing case, and a two-dimensional weakly compressible Poiseuille flow with temperature controlled mass density variations. The binary mixing case features a transient configuration with strong variations in mass density due to the difference in molecular weights of the mixing constituents. The mixing is diffusion controlled since the model does not consider gravity and provides adequate conditions for spatial and temporal order of accuracy analysis. The variable mass density Poiseuille flow problem provides a classical canonical configuration used in internal turbulent flows: pressure driven, fully developed flow with heat transfer. The numerical experiments in this case were aimed at showing the spatial scheme's characteristics, the expected results were obtained through grid refinement studies. Further studies were considered for classical laminar boundary layer flow (Blasius flow) with successful comparisons with theoretical velocity profiles and wall-shear stress profiles; this demonstrates the boundary layer modeling capability and the use of inflow/outflow conditions in providing correct numerical and physical results. Chapter 3 of this thesis presents a detailed description of the summary discussed above.

3. Canonical validation studies have been devised and executed by providing configurations that exploit important areas found in the modeling of fires, that is: turbulent flow modeling, heat transfer, and mass transfer effects. A high resolution technique, i.e., large eddy simulation, is used as the main turbulence model for two

numerical experiments in turbulent channel flow. The difference in configuration lies in the inclusion of variable property heat transfer; comparisons made with benchmark results demonstrate the effect of heat transfer on the turbulence statistics and also shows excellent agreement with channel data from direct numerical simulations (DNS) for both cases. The effect of mass transfer is demonstrated in the third and last case, through a turbulent boundary layer case (Spalart et al) with injection of slow velocity fluid at the surface to mimic the mass transfer conditions found in the thermal degradation of fuels in fire scenarios. Chapter 4 of this thesis presents a detailed description of the cases discussed above.

4. A turbulent wall-fire problem is modeled and compared with the experimental results available in the literature for momentum driven concurrent flow spread. Small-scale fire size features are emphasized such that flame heat transfer properties are convectively dominated. Turbulence properties are calibrated such that the numerical inflow conditions match the quasi-isotropic turbulence fluctuations specified experimentally. The combustion modeled is also calibrated for PMMA fuel and compared to fast-chemistry Burke-Schumann model providing an initial framework for air-PMMA fuel combustion. Flame structure, flame length and wall surface heat flux properties demonstrate the capability of the solver in handling turbulent wall flame dynamics.

6.3 *Future Work*

Several problems of interest can be extended from the use of the fire modeling tool presented in this thesis. To the author's perspective the following list presents the most promising areas of future work:

1. An immediate area of modeling interest is to extend the present study from an anchored wall-flame configuration to a full horizontal flame spread problem by making use of the coupled gas-phase solid-phase solid wall capability. This simple extension provides the correct configuration to facilitate direct comparison and validation with the turbulent flame spread database of Zhou et al [49], [50]. The full spread problem enables detailed comparison of surface convective heat fluxes and flame length at several pyrolysis heights with mean flows and turbulent intensities. A successful simulation would provide the first complete LES calculation of momentum driven concurrent flow flame spread.
2. Numerical modeling of turbulent boundary layers featuring buoyancy driven flow physics presents an important configuration relevant to fire spread problems. A preliminary validation study on turbulent buoyancy driven boundary layers developing over a hot vertical plate is strongly suggested to demonstrate the solver's ability to accurately model buoyant flows near the outflow boundary, and to evaluate the use of sponge regions of hyper-viscosity or accelerated flow fields. The database of Tsuji et al [86], providing low and high order kinematic and scalar statistics is widely available for validation and comparative studies. A natural extension to

combustion is to model the interaction of turbulent buoyancy driven non-premixed flames over flammable vertical walls by conducting wall resolved LES calculations. The LES combustion component can be validated with the selected experimental configuration corresponding to the classical non-spreading vertical wall fire experiments studied by Ahmad & Faeth [87].

3. Also of importance is the pyrolysis thermal degradation process that significantly contributes to the flame spread and fire growth in typical enclosure fires. This key area will be addressed by incorporating a pyrolysis solver to provide the gaseous volatiles through the solid phase combustion modeling of the fuel, this will contribute in providing a more accurate description of the heat release rate and thermal degradation in the flame spread problem independent from a priori experimental conditions. ThermaKin developed by Federal Aviation Administration (FAA) and by Dr. Stanislav Stoliarov of the Fire Protection Engineering Faculty at the University of Maryland is proposed as a boundary condition into LES-BLAC [88].

Appendix A: Finite Differences Discretization

2D U-momentum equation (les_solve_uhat.f90)

$$\frac{\partial}{\partial t}(g_i) + \frac{\partial}{\partial x_j} \left(\overline{g_j^{x_i} u_i^{x_j}{}^t} \right) = -\frac{\partial}{\partial x_i}(p) + \frac{\partial}{\partial x_j}(\tau_{ij})$$

$$\tau_{ij} = \begin{cases} \frac{\overline{\mu^{x_i}{}^{x_j}}}{\mu^{x_i}{}^{x_j}} \left[\frac{\partial \overline{u_i}^t}{\partial x_j} + \frac{\partial \overline{u_j}^t}{\partial x_i} \right], & \text{if } i \neq j \\ 2\mu \left[\frac{\partial \overline{u_i}^t}{\partial x_j} - \frac{1}{3} \frac{\partial \overline{u_k}^t}{\partial x_k} \delta_{ij} \right], & \text{if } i = j \end{cases}$$

uuE:

$$\frac{1}{4} \left(\frac{u_{i,j}^n + u_{i,j}^{n+1}}{2} + \frac{u_{i+1,j}^n + u_{i+1,j}^{n+1}}{2} \right) \left[\begin{array}{l} \frac{1}{8} \left\{ \begin{array}{l} u_{i,j}^n (\rho_{i,j}^{n+1} + \rho_{i+1,j}^{n+1} + \rho_{i,j}^n + \rho_{i+1,j}^n) + \\ u_{i,j}^{n+1} (\rho_{i,j}^{n+1} + \rho_{i+1,j}^{n+1} + \rho_{i,j}^n + \rho_{i+1,j}^n) \end{array} \right\} \\ + \frac{1}{8} \left\{ \begin{array}{l} u_{i+1,j}^n (\rho_{i+1,j}^{n+1} + \rho_{i+2,j}^{n+1} + \rho_{i+1,j}^n + \rho_{i+2,j}^n) + \\ u_{i+1,j}^{n+1} (\rho_{i+1,j}^{n+1} + \rho_{i+2,j}^{n+1} + \rho_{i+1,j}^n + \rho_{i+2,j}^n) \end{array} \right\} \end{array} \right]$$

uuW:

$$\frac{1}{4} \left(\frac{u_{i,j}^n + u_{i,j}^{n+1}}{2} + \frac{u_{i-1,j}^n + u_{i-1,j}^{n+1}}{2} \right) \left[\begin{array}{l} \frac{1}{8} \left\{ \begin{array}{l} u_{i,j}^n (\rho_{i,j}^{n+1} + \rho_{i+1,j}^{n+1} + \rho_{i,j}^n + \rho_{i+1,j}^n) + \\ u_{i,j}^{n+1} (\rho_{i,j}^{n+1} + \rho_{i+1,j}^{n+1} + \rho_{i,j}^n + \rho_{i+1,j}^n) \end{array} \right\} \\ + \frac{1}{8} \left\{ \begin{array}{l} u_{i-1,j}^n (\rho_{i-1,j}^{n+1} + \rho_{i,j}^{n+1} + \rho_{i-1,j}^n + \rho_{i,j}^n) + \\ u_{i-1,j}^{n+1} (\rho_{i-1,j}^{n+1} + \rho_{i,j}^{n+1} + \rho_{i-1,j}^n + \rho_{i,j}^n) \end{array} \right\} \end{array} \right]$$

uvN:

$$\frac{1}{2} \left(\frac{u_{i,j}^n + u_{i,j}^{n+1}}{2} \frac{u_{i,j+1}^n + u_{i,j+1}^{n+1}}{2} \right) \left[\begin{array}{l} \frac{weW}{8} \left\{ \begin{array}{l} v_{i,j}^n (\rho_{i,j}^{n+1} + \rho_{i,j+1}^{n+1} + \rho_{i,j}^n + \rho_{i,j+1}^n) + \\ v_{i,j}^{n+1} (\rho_{i,j}^{n+1} + \rho_{i,j+1}^{n+1} + \rho_{i,j}^n + \rho_{i,j+1}^n) \end{array} \right\} \\ + \frac{weE}{8} \left\{ \begin{array}{l} v_{i+1,j}^n (\rho_{i+1,j}^{n+1} + \rho_{i+2,j}^{n+1} + \rho_{i+1,j}^n + \rho_{i+2,j}^n) + \\ v_{i+1,j}^{n+1} (\rho_{i+1,j}^{n+1} + \rho_{i+2,j}^{n+1} + \rho_{i+1,j}^n + \rho_{i+2,j}^n) \end{array} \right\} \end{array} \right]$$

uvS:

$$\frac{1}{2} \left(\frac{u_{i,j}^n + u_{i,j}^{n+1}}{2} \frac{u_{i,j-1}^n + u_{i,j-1}^{n+1}}{2} \right) \left[\begin{array}{l} \frac{weW}{8} \left\{ \begin{array}{l} v_{i,j-1}^n (\rho_{i,j-1}^{n+1} + \rho_{i,j}^{n+1} + \rho_{i,j-1}^n + \rho_{i,j}^n) + \\ v_{i,j-1}^{n+1} (\rho_{i,j-1}^{n+1} + \rho_{i,j}^{n+1} + \rho_{i,j-1}^n + \rho_{i,j}^n) \end{array} \right\} \\ + \frac{weE}{8} \left\{ \begin{array}{l} v_{i+1,j-1}^n (\rho_{i+1,j-1}^{n+1} + \rho_{i+1,j}^{n+1} + \rho_{i+1,j-1}^n + \rho_{i+1,j}^n) + \\ v_{i+1,j-1}^{n+1} (\rho_{i+1,j-1}^{n+1} + \rho_{i+1,j}^{n+1} + \rho_{i+1,j-1}^n + \rho_{i+1,j}^n) \end{array} \right\} \end{array} \right]$$

duudx: $(uuE - uuW)/\Delta x_c$

duvdy: $(uvN - uvS)/\Delta y$

d2udx2:

$$\left[\frac{\mu_E}{\Delta x} \left(\frac{u_{i+1,j}^n + u_{i+1,j}^{n+1}}{2} - \frac{u_{i,j}^n + u_{i,j}^{n+1}}{2} \right) - \frac{\mu_W}{\Delta x} \left(\frac{u_{i,j}^n + u_{i,j}^{n+1}}{2} - \frac{u_{i-1,j}^n + u_{i-1,j}^{n+1}}{2} \right) \right] \frac{1}{\Delta x_c}$$

ddxdudx:

$$\left\{ \begin{array}{l} \left[\frac{\mu_E}{\Delta x} \left(\frac{u_{i+1,j}^n + u_{i+1,j}^{n+1}}{2} - \frac{u_{i,j}^n + u_{i,j}^{n+1}}{2} \right) - \frac{\mu_W}{\Delta x} \left(\frac{u_{i,j}^n + u_{i,j}^{n+1}}{2} - \frac{u_{i-1,j}^n + u_{i-1,j}^{n+1}}{2} \right) \right] \frac{1}{\Delta x_c} \\ -\frac{2}{3} \left[\frac{\mu_E}{\Delta x} \left(\frac{u_{i+1,j}^n + u_{i+1,j}^{n+1}}{2} - \frac{u_{i,j}^n + u_{i,j}^{n+1}}{2} + \frac{v_{i+1,j}^n + v_{i+1,j}^{n+1}}{2} - \frac{v_{i+1,j-1}^n + v_{i+1,j-1}^{n+1}}{2} \right) \right] \frac{1}{\Delta x_c} \\ -\frac{\mu_W}{\Delta x} \left(\frac{u_{i,j}^n + u_{i,j}^{n+1}}{2} - \frac{u_{i-1,j}^n + u_{i-1,j}^{n+1}}{2} + \frac{v_{i,j}^n + v_{i,j}^{n+1}}{2} - \frac{v_{i,j-1}^n + v_{i,j-1}^{n+1}}{2} \right) \right] \frac{1}{\Delta x_c} \end{array} \right\}$$

ddydvdx:

$$\left[\frac{\mu_N}{\Delta x_c} \left(\frac{v_{i+1,j}^n + v_{i+1,j}^{n+1}}{2} - \frac{v_{i,j}^n + v_{i,j}^{n+1}}{2} \right) - \frac{\mu_S}{\Delta x_c} \left(\frac{v_{i+1,j-1}^n + v_{i+1,j-1}^{n+1}}{2} - \frac{v_{i,j-1}^n + v_{i,j-1}^{n+1}}{2} \right) \right] \frac{1}{\Delta y}$$

ddyduy (handled explicit or implicit) :

$$\left[\frac{\mu_N}{\Delta y_c} \left(\frac{u_{i,j+1}^n + u_{i,j+1}^{n+1}}{2} - \frac{u_{i,j}^n + u_{i,j}^{n+1}}{2} \right) - \frac{\mu_S}{\Delta y_c} \left(\frac{u_{i,j}^n + u_{i,j}^{n+1}}{2} - \frac{u_{i,j-1}^n + u_{i,j-1}^{n+1}}{2} \right) \right] \frac{1}{\Delta y}$$

dpx:

$$-\left[\frac{P_{i+1,j}^n - P_{i,j}^n}{\Delta x_c} \right]$$

2D V-momentum equation (les_solve_vhat.f90)

vuE:

$$\frac{1}{2} \left(\frac{v_{i,j}^n + v_{i,j}^{n+1}}{2} + \frac{v_{i+1,j}^n + v_{i+1,j}^{n+1}}{2} \right) \left[\begin{array}{l} \frac{weN}{8} \left\{ \begin{array}{l} u_{i,j+1}^n (\rho_{i,j+1}^{n+1} + \rho_{i,j+2}^{n+1} + \rho_{i,j+1}^n + \rho_{i,j+2}^n) + \\ u_{i,j+1}^{n+1} (\rho_{i,j+1}^{n+1} + \rho_{i,j+2}^{n+1} + \rho_{i,j+1}^n + \rho_{i,j+2}^n) \end{array} \right\} \\ + \frac{weS}{8} \left\{ \begin{array}{l} u_{i,j}^n (\rho_{i,j}^{n+1} + \rho_{i,j+1}^{n+1} + \rho_{i,j}^n + \rho_{i,j+1}^n) + \\ u_{i,j}^{n+1} (\rho_{i,j}^{n+1} + \rho_{i,j+1}^{n+1} + \rho_{i,j}^n + \rho_{i,j+1}^n) \end{array} \right\} \end{array} \right]$$

vuW:

$$\frac{1}{2} \left(\frac{v_{i,j}^n + v_{i,j}^{n+1}}{2} + \frac{v_{i-1,j}^n + v_{i-1,j}^{n+1}}{2} \right) \left[\begin{array}{l} \frac{weN}{8} \left\{ \begin{array}{l} u_{i-1,j+1}^n (\rho_{i-1,j+1}^{n+1} + \rho_{i-1,j+2}^{n+1} + \rho_{i-1,j+1}^n + \rho_{i-1,j+2}^n) + \\ u_{i-1,j+1}^{n+1} (\rho_{i-1,j+1}^{n+1} + \rho_{i-1,j+2}^{n+1} + \rho_{i-1,j+1}^n + \rho_{i-1,j+2}^n) \end{array} \right\} \\ + \frac{weS}{8} \left\{ \begin{array}{l} u_{i-1,j}^n (\rho_{i-1,j}^{n+1} + \rho_{i-1,j+1}^{n+1} + \rho_{i-1,j}^n + \rho_{i-1,j+1}^n) + \\ u_{i-1,j}^{n+1} (\rho_{i-1,j}^{n+1} + \rho_{i-1,j+1}^{n+1} + \rho_{i-1,j}^n + \rho_{i-1,j+1}^n) \end{array} \right\} \end{array} \right]$$

vvN:

$$\frac{1}{4} \left(\frac{v_{i,j}^n + v_{i,j}^{n+1}}{2} + \frac{v_{i,j+1}^n + v_{i,j+1}^{n+1}}{2} \right) \left[\begin{array}{l} \frac{weW}{8} \left\{ \begin{array}{l} v_{i,j}^n (\rho_{i,j}^{n+1} + \rho_{i,j+1}^{n+1} + \rho_{i,j}^n + \rho_{i,j+1}^n) + \\ v_{i,j}^{n+1} (\rho_{i,j}^{n+1} + \rho_{i,j+1}^{n+1} + \rho_{i,j}^n + \rho_{i,j+1}^n) \end{array} \right\} \\ + \frac{weE}{8} \left\{ \begin{array}{l} v_{i,j+1}^n (\rho_{i,j+1}^{n+1} + \rho_{i,j+2}^{n+1} + \rho_{i,j+1}^n + \rho_{i,j+2}^n) + \\ v_{i,j+1}^{n+1} (\rho_{i,j+1}^{n+1} + \rho_{i,j+2}^{n+1} + \rho_{i,j+1}^n + \rho_{i,j+2}^n) \end{array} \right\} \end{array} \right]$$

vvS:

$$\frac{1}{4} \left(\frac{v_{i,j}^n + v_{i,j}^{n+1}}{2} + \frac{v_{i,j-1}^n + v_{i,j-1}^{n+1}}{2} \right) \left[\frac{weW}{8} \left\{ \begin{array}{l} v_{i,j}^n (\rho_{i,j}^{n+1} + \rho_{i,j+1}^{n+1} + \rho_{i,j}^n + \rho_{i,j+1}^n) + \\ v_{i,j}^{n+1} (\rho_{i,j}^{n+1} + \rho_{i,j+1}^{n+1} + \rho_{i,j}^n + \rho_{i,j+1}^n) \end{array} \right\} \right. \\ \left. + \frac{weE}{8} \left\{ \begin{array}{l} v_{i,j-1}^n (\rho_{i,j-1}^{n+1} + \rho_{i,j}^{n+1} + \rho_{i,j-1}^n + \rho_{i,j}^n) + \\ v_{i,j-1}^{n+1} (\rho_{i,j-1}^{n+1} + \rho_{i,j}^{n+1} + \rho_{i,j-1}^n + \rho_{i,j}^n) \end{array} \right\} \right]$$

duudx: $(vuE - vuW)/\Delta x$

dvvdy: $(vvN - vvS)/\Delta y_c$

d2vdx2:

$$\left[\frac{\mu_E}{\Delta x_c} \left(\frac{v_{i+1,j}^n + v_{i+1,j}^{n+1}}{2} - \frac{v_{i,j}^n + v_{i,j}^{n+1}}{2} \right) - \frac{\mu_W}{\Delta x_c} \left(\frac{v_{i,j}^n + v_{i,j}^{n+1}}{2} - \frac{v_{i-1,j}^n + v_{i-1,j}^{n+1}}{2} \right) \right] \frac{1}{\Delta x}$$

ddydvdy_E:

$$\left\{ -\frac{2}{3} \left[\frac{\mu_N}{\Delta x} \left(\frac{u_{i,j+1}^n + u_{i,j+1}^{n+1}}{2} - \frac{u_{i-1,j+1}^n + u_{i-1,j+1}^{n+1}}{2} \right) \right. \right. \\ \left. \left. - \frac{\mu_S}{\Delta x} \left(\frac{u_{i,j}^n + u_{i,j}^{n+1}}{2} - \frac{u_{i-1,j}^n + u_{i-1,j}^{n+1}}{2} \right) \right] \frac{1}{\Delta y_c} \right\}$$

ddxdudy:

$$\left[\frac{\mu_E}{\Delta y_c} \left(\frac{u_{i,j+1}^n + u_{i,j+1}^{n+1}}{2} - \frac{u_{i,j}^n + u_{i,j}^{n+1}}{2} \right) - \frac{\mu_W}{\Delta y_c} \left(\frac{u_{i-1,j+1}^n + u_{i-1,j+1}^{n+1}}{2} - \frac{u_{i-1,j}^n + u_{i-1,j}^{n+1}}{2} \right) \right] \frac{1}{\Delta x}$$

d2vdy2 + ddydvdy_I (handled explicit or implicit) :

$$\begin{aligned} & \left[\frac{\mu_N}{\Delta y} \left(\frac{v_{i,j+1}^n + v_{i,j+1}^{n+1}}{2} - \frac{v_{i,j}^n + v_{i,j}^{n+1}}{2} \right) - \frac{\mu_S}{\Delta y} \left(\frac{v_{i,j}^n + v_{i,j}^{n+1}}{2} - \frac{v_{i,j-1}^n + v_{i,j-1}^{n+1}}{2} \right) \right] \frac{1}{\Delta y_c} \\ & + \frac{1}{3} \left[\frac{\mu_N}{\Delta y} \left(\frac{v_{i,j+1}^n + v_{i,j+1}^{n+1}}{2} - \frac{v_{i,j}^n + v_{i,j}^{n+1}}{2} \right) \right. \\ & \left. - \frac{\mu_S}{\Delta y} \left(\frac{v_{i,j}^n + v_{i,j}^{n+1}}{2} - \frac{v_{i,j-1}^n + v_{i,j-1}^{n+1}}{2} \right) \right] \frac{1}{\Delta y_c} \end{aligned}$$

dpdy:

$$- \left[\frac{P_{i,j+1}^n - P_{i,j}^n}{\Delta y_c} \right]$$

2D scalar equation (les_scalar_cd.f90) – central difference option

$$\frac{\partial}{\partial t}(\rho c) + \frac{\partial}{\partial x_j} \left(g_j \bar{c}^{x_j t} \right) = + \frac{\partial}{\partial x_j} \left[\frac{\bar{c}^{x_j t}}{\rho \alpha^{x_j}} \frac{\partial}{\partial x_j} (\bar{c}^t) \right]$$

cuE:

$$\frac{1}{8} u_{i,j}^n (\rho_{i,j}^{n+1} + \rho_{i+1,j}^{n+1} + \rho_{i,j}^n + \rho_{i+1,j}^n) \left(\frac{c_{i,j}^n + c_{i,j}^{n+1}}{2} + \frac{c_{i+1,j}^n + c_{i+1,j}^{n+1}}{2} \right)$$

cuW:

$$\frac{1}{8} u_{i-1,j}^n (\rho_{i-1,j}^{n+1} + \rho_{i,j}^{n+1} + \rho_{i-1,j}^n + \rho_{i,j}^n) \left(\frac{c_{i-1,j}^n + c_{i-1,j}^{n+1}}{2} + \frac{c_{i,j}^n + c_{i,j}^{n+1}}{2} \right)$$

cvN:

$$\frac{1}{8} v_{i,j}^n (\rho_{i,j}^{n+1} + \rho_{i,j+1}^{n+1} + \rho_{i,j}^n + \rho_{i,j+1}^n) \left(\frac{c_{i,j}^n + c_{i,j}^{n+1}}{2} + \frac{c_{i,j+1}^n + c_{i,j+1}^{n+1}}{2} \right)$$

cvS:

$$\frac{1}{8} v_{i,j-1}^n (\rho_{i,j-1}^{n+1} + \rho_{i,j}^{n+1} + \rho_{i,j-1}^n + \rho_{i,j}^n) \left(\frac{c_{i,j-1}^n + c_{i,j-1}^{n+1}}{2} + \frac{c_{i,j}^n + c_{i,j}^{n+1}}{2} \right)$$

dcudx: (cuE – cuW)/Δx

dcvdy: (cvN – cvS)/Δy

d2cdx2:

$$\left[\frac{(\rho\alpha)_E}{\Delta x_c} \left(\frac{c_{i+1,j}^n + c_{i+1,j}^{n+1}}{2} - \frac{c_{i,j}^n + c_{i,j}^{n+1}}{2} \right) - \frac{(\rho\alpha)_W}{\Delta x_c} \left(\frac{c_{i,j}^n + c_{i,j}^{n+1}}{2} - \frac{c_{i-1,j}^n + c_{i-1,j}^{n+1}}{2} \right) \right] \frac{1}{\Delta x}$$

d2cdy2:

$$\left[\frac{(\rho\alpha)_N}{\Delta y_c} \left(\frac{c_{i,j+1}^n + c_{i,j+1}^{n+1}}{2} - \frac{c_{i,j}^n + c_{i,j}^{n+1}}{2} \right) - \frac{(\rho\alpha)_S}{\Delta y_c} \left(\frac{c_{i,j}^n + c_{i,j}^{n+1}}{2} - \frac{c_{i,j-1}^n + c_{i,j-1}^{n+1}}{2} \right) \right] \frac{1}{\Delta y}$$

Bibliography

- [1] D. Atkins, “Revolutionizing Science and Engineering Through Cyberinfrastructure: Report of the National Science Foundation Blue-Ribbon Advisory Panel on Cyberinfrastructure,” Jul. 2003.
- [2] “Fire Dynamics Simulator (Version 5) Technical Reference Guide (NIST Special Publication 1018-5),” 2007.
- [3] “OpenFoam (Open Source CFD Tool box),” 2011.
- [4] “Fire Dynamics Tool (FDT) Quantitative Fire Hazard Analysis Methods for the U.S. Nuclear Regulatory Commission Fire Protection Inspection Program,” 2004.
- [5] S. M. Olenick, “An Updated International Survey of Computer Models for Fire and Smoke,” *Journal of Fire Protection Engineering*, vol. 13, no. 2, pp. 87–110, May 2003.
- [6] W. Jones, “State of the art in zone modeling of fires,” 2001.
- [7] V. Novozhilov, “Computational fluid dynamics modeling of compartment fires,” *Progress in Energy and Combustion Science*, vol. 27, no. 6, pp. 611–666, Jan. 2001.
- [8] A. Trouvé and Y. Wang, “Large eddy simulation of compartment fires,” *International Journal of Computational Fluid Dynamics*, vol. 24, no. 10, pp. 449–466, Dec. 2010.
- [9] K. McGrattan, R. McDermott, J. Floyd, S. Hostikka, G. Forney, and H. Baum, “Computational fluid dynamics modelling of fire,” *International Journal of Computational Fluid Dynamics*, vol. 26, no. 6–8, pp. 349–361, Jul. 2012.
- [10] N. Peters, *Turbulent Combustion (Google eBook)*. Cambridge University Press, 2000, p. 304.
- [11] F. C. Lockwood and N. G. Shah, “A new radiation solution method for incorporation in general combustion prediction procedures,” *Symposium (International) on Combustion*, vol. 18, no. 1, pp. 1405–1414, Jan. 1981.
- [12] C. DIBLASI, “Modeling chemical and physical processes of wood and biomass pyrolysis,” *Progress in Energy and Combustion Science*, vol. 34, no. 1, pp. 47–90, Feb. 2008.
- [13] C. Lautenberger and C. Fernandez-Pello, “Generalized pyrolysis model for combustible solids,” *Fire Safety Journal*, vol. 44, no. 6, pp. 819–839, Aug. 2009.

- [14] C. DiBlasi, "Modeling and simulation of combustion processes of charring and non-charring solid fuels," *Progress in Energy and Combustion Science*, vol. 19, no. 1, pp. 71–104, Jan. 1993.
- [15] D. Wu, D. Guillemin, and A. W. Marshall, "A modeling basis for predicting the initial sprinkler spray," *Fire Safety Journal*, vol. 42, no. 4, pp. 283–294, Jun. 2007.
- [16] N. Ren, H. R. Baum, and A. W. Marshall, "A comprehensive methodology for characterizing sprinkler sprays," *Proceedings of the Combustion Institute*, vol. 33, no. 2, pp. 2547–2554, Jan. 2011.
- [17] A. Lecoustre, V. Narayanan, P. Baum, H.R. Trouve, "Local Extinction of Diffusion Flames in Fires," *Fire Safety Science*, vol. 10, pp. 583–595.
- [18] P. . Spalart, "Strategies for turbulence modelling and simulations," *International Journal of Heat and Fluid Flow*, vol. 21, no. 3, pp. 252–263, Jun. 2000.
- [19] D. K. Chapman, "Computational Aerodynamics Development and Outlook," *AIAA Journal*, vol. 17, no. 12, May 1979.
- [20] E. Balaras, C. Benocci, and U. Piomelli, "Two-layer approximate boundary conditions for large-eddy simulations," *AIAA Journal*, vol. 34, no. 6, May 1996.
- [21] U. Piomelli and E. Balaras, "W ALL L AYER M ODELS FOR LARGE EDDY SIMULATIONS," *Annual Review of Fluid Mechanics*, vol. 34, no. 1, pp. 349–374, Jan. 2002.
- [22] T. S. Lund and P. Moin, "Large-eddy simulation of a concave wall boundary layer," *International Journal of Heat and Fluid Flow*, vol. 17, no. 3, pp. 290–295, Jun. 1996.
- [23] P. Moin and K. Mahesh, "DIRECT NUMERICAL SIMULATION: A Tool in Turbulence Research," *Annual Review of Fluid Mechanics*, vol. 30, no. 1, pp. 539–578, Jan. 1998.
- [24] A. Keating, "Large eddy simulation of heat transfer in turbulent channel flow and in the turbulent flow downstream of a backward facing step," University of Queensland, 2003.
- [25] P. Spalart, "Direct simulation of a turbulent boundary layer up to $R_j = 1410$," *Journal of Fluid Mechanics*, vol. 187, pp. 61–98, 1988.
- [26] H. LE, P. MOIN, and J. KIM, "Direct numerical simulation of turbulent flow over a backward-facing step," *Journal of Fluid Mechanics*, vol. 330, pp. 349–374, 1997.

- [27] S. Lee, S. K. Lele, and P. Moin, "Simulation of spatially evolving turbulence and the applicability of Taylor's hypothesis in compressible flow," *Physics of Fluids A: Fluid Dynamics*, vol. 4, no. 7, p. 1521, Jul. 1992.
- [28] P. Na, Ya, Moin, "Direct numerical simulation of turbulent boundary layers with adverse pressure gradient and separation (Tech Report TF-68)," 1996.
- [29] K. Akselvoll and P. Moin, "Large-eddy simulation of turbulent confined coannular jets," *Journal of Fluid Mechanics*, vol. 315, pp. 387–411, 1996.
- [30] Batten, P, Goldberg, U and S. Chakravarthy, "Interfacing Statistical Turbulence Closures with Large-Eddy Simulation," *AIAA Journal*, vol. 42, no. 3, May 2004.
- [31] H. J. Spille-Kohoff, A, Kaltenbach, "Generation of Turbulent Inflow Data with a Prescribed Shear-Stress Profile," in *Third ASFOR International Conference on DNS/LES*, 2001.
- [32] A. Celani, M. Cencini, A. Mazzino, and M. Vergassola, "Active and passive fields face to face," *New Journal of Physics*, vol. 6, no. 1, pp. 72–72, Jul. 2004.
- [33] P. Kim, J, Moin, *Transport of passive scalars in a turbulent channel flow in Turbulent Shear Flows 6*. Berlin, Heidelberg: Springer Berlin Heidelberg, 1989, pp. 85–96.
- [34] N. Kasagi and O. Iida, "Progress in direct numerical simulation of turbulent heat transfer," in *Proceedings of the 5th ASME/JSME Joint Thermal Engineering Conference*, 1999.
- [35] N. Kasagi, Y. Tomita, and A. Kuroda, "Direct numerical simulation of passive scalar field in a turbulent channel flow," *ASME Transactions Journal of Heat Transfer*, vol. 114, pp. 598–606, Aug. 1992.
- [36] W.-P. Wang and R. H. Pletcher, "On the large eddy simulation of a turbulent channel flow with significant heat transfer," *Physics of Fluids*, vol. 8, no. 12, p. 3354, Dec. 1996.
- [37] T. Nicoud, F, Poinso, "Direct numerical simulation of a channel flow with variable properties," in *First International Symposium on Turbulence and Shear Flow Phenomena*, 1999.
- [38] J. N. De Ris, "Spread of a laminar diffusion flame," *Symposium (International) on Combustion*, vol. 12, no. 1, pp. 241–252, Jan. 1969.
- [39] R. A. Altenkirch, R. Eichhorn, and P. C. Shang, "Buoyancy effects on flames spreading down thermally thin fuels," *Combustion and Flame*, vol. 37, no. null, pp. 71–83, Jan. 1980.

- [40] L. Zhou, A. C. Fernandez-Pello, and R. Cheng, "Flame spread in an opposed turbulent flow," *Combustion and Flame*, vol. 81, no. 1, pp. 40–49, Jul. 1990.
- [41] I. S. Wichman, F. A. Williams, and I. Glassman, "Theoretical aspects of flame spread in an opposed flow over flat surfaces of solid fuels," *Symposium (International) on Combustion*, vol. 19, no. 1, pp. 835–845, Jan. 1982.
- [42] I. S. Wichman, "Theory of opposed-flow flame spread," *Progress in Energy and Combustion Science*, vol. 18, no. 6, pp. 553–593, Jan. 1992.
- [43] S. Bhattacharjee, J. West, and R. A. Altenkirch, "Determination of the spread rate in opposed-flow flame spread over thick solid fuels in the thermal regime," *Symposium (International) on Combustion*, vol. 26, no. 1, pp. 1477–1485, Jan. 1996.
- [44] S. Bhattacharjee, M. D. King, S. Takahashi, T. Nagumo, and K. Wakai, "Downward flame spread over poly(methyl) methacrylate," *Proceedings of the Combustion Institute*, vol. 28, no. 2, pp. 2891–2897, Jan. 2000.
- [45] G. H. Markstein and J. de Ris, "Upward fire spread over textiles," *Symposium (International) on Combustion*, vol. 14, no. 1, pp. 1085–1097, Jan. 1973.
- [46] A. Wu, P. K., Orloff, L., Tewarson, "Assessment of Material Flammability With the FSG Propagation Model and Laboratory Test Methods in 13th Joint Panel Meeting of the UJNR Panel on Fire Research and Safety," 1997.
- [47] A. Tewarson and S. D. Ogden, "Fire behavior of polymethylmethacrylate," *Combustion and Flame*, vol. 89, no. 3–4, pp. 237–259, Jun. 1992.
- [48] J. QUINTIERE, M. HARKLEROAD, and Y. HASEMI, "Wall Flames and Implications for Upward Flame Spread," *Combustion Science and Technology*, vol. 48, no. 3–4, pp. 191–222, Jul. 1986.
- [49] L. Zhou, "Solid Fuel Flame Spread and Mass Burning in Turbulent Flow," PhD Thesis University of California at Berkeley, USA, 1991.
- [50] L. Zhou and A. C. Fernandez-Pello, "Turbulent, concurrent, ceiling flame spread: The effect of buoyancy," *Combustion and Flame*, vol. 92, no. 1–2, pp. 45–59, Jan. 1993.
- [51] L. Zhou and A. C. Fernandez-Pello, "Concurrent turbulent flame spread," *Symposium (International) on Combustion*, vol. 23, no. 1, pp. 1709–1714, Jan. 1991.

- [52] M. Germano, U. Piomelli, P. Moin, and W. H. Cabot, “A dynamic subgrid-scale eddy viscosity model,” *Physics of Fluids A: Fluid Dynamics*, vol. 3, no. 7, p. 1760, Jul. 1991.
- [53] C. Pierce, “Progress-variable approach for large-eddy simulation of turbulent combustion,” Stanford University, 2001.
- [54] C. Pierce and P. Moin, “Progress-variable approach for large-eddy simulation of non-premixed turbulent combustion,” *Journal of Fluid Mechanics*, 2004.
- [55] S. Pope, *Turbulent flows*. Cambridge University Press, 2000.
- [56] D. K. Lilly, “A proposed modification of the Germano subgrid-scale closure method,” *Physics of Fluids A: Fluid Dynamics*, vol. 4, no. 3, p. 633, Mar. 1992.
- [57] G. Erlebacher, M. Y. Hussaini, C. G. Speziale, and T. A. Zang, “Toward the large-eddy simulation of compressible turbulent flows,” *Journal of Fluid Mechanics*, vol. 238, pp. 155–185.
- [58] P. Moin, K. Squires, W. Cabot, and S. Lee, “A dynamic subgrid-scale model for compressible turbulence and scalar transport,” *Physics of Fluids A: Fluid Dynamics*, vol. 3, no. 11, p. 2746, Nov. 1991.
- [59] T. Ma, “Large-eddy Simulation of Variable Density Flows,” University of Maryland at College Park, 2006.
- [60] B. P. Leonard, “A stable and accurate convective modelling procedure based on quadratic upstream interpolation,” *Computer Methods in Applied Mechanics and Engineering*, vol. 19, no. 1, pp. 59–98, Jun. 1979.
- [61] T. S. Lund, X. Wu, and K. D. Squires, “Generation of Turbulent Inflow Data for Spatially-Developing Boundary Layer Simulations,” *Journal of Computational Physics*, vol. 140, no. 2, pp. 233–258, Mar. 1998.
- [62] A. Keating, U. Piomelli, E. Balaras, and H.-J. Kaltenbach, “A priori and a posteriori tests of inflow conditions for large-eddy simulation,” *Physics of Fluids*, vol. 16, no. 12, p. 4696, Nov. 2004.
- [63] G. D. Prisco, “Hybrid RANS LES Simulation of non-equilibrium boundary layers,” University of Maryland at College Park, 2007.
- [64] I. Orlanski, “A simple boundary condition for unbounded hyperbolic flows,” *Journal of Computational Physics*, vol. 21, no. 3, pp. 251–269, Jul. 1976.
- [65] P. J. Roache, *Verification and validation in computational science and engineering*. Albuquerque, N.M.: Hermosapublishers, 1998, p. 446 pg.

- [66] P. J. Roache, "Verification of Codes and Calculations," *AIAA Journal*, vol. 36, no. 5, pp. 696–702, May 1998.
- [67] "Guide for the Verification and Validation of Computational Fluid Dynamics Simulations," 1998.
- [68] M. Abanto, Juan, Pelletier, D, Garon, A, Trepanier, Jean-Yves, Reggio, "Verification of some Commercial CFD Codes on Atypical CFD Problems," in *43rd AIAA Aerospace Sciences Meeting and Exhibit 10-13 January 2005 (AIAA 2005-682)*, 2005.
- [69] W. Kleb, B, Wood, "CFD: A Castle in the Sand? (AIAA)," in *34th AIAA Fluid Dynamics Conference and Exhibit 28 June - 1 July 2004*, 2004.
- [70] L. Shunn and F. Ham, "Method of manufactured solutions applied to variable-density flow solvers," ... *Research Briefs-2007, Center for Turbulence ...*, 2007.
- [71] R. D. Moser, J. Kim, and N. N. Mansour, "Direct numerical simulation of turbulent channel flow up to $Re_{\tau}=590$," *Physics of Fluids*, vol. 11, no. 4, p. 943, Apr. 1999.
- [72] F. Nicoud, "Numerical study of a channel flow with variable properties," *Center for Turbulent Research, Annual Research*, 1998.
- [73] H. Coleman and F. Stern, "Uncertainties and CFD code validation," *Journal of Fluids Engineering*, vol. 119, pp. 795–803, 1997.
- [74] U. Piomelli and E. Balaras, "Wall-layer models for large-eddy simulations," *Annual review of fluid mechanics*, 2002.
- [75] I. Marusic, R. Mathis, and N. Hutchins, "High Reynolds number effects in wall turbulence," *International Journal of Heat and Fluid Flow*, vol. 31, no. 3, pp. 418–428, Jun. 2010.
- [76] J. Klewicki, "Reynolds number dependence, scaling, and dynamics of turbulent boundary layers," *Journal of fluids engineering*, vol. 132, no. 9, pp. 1–48, 2010.
- [77] W. Kays and M. Crawford, *Convective heat and mass transfer*. McGraw-Hill Series in Mechanical Engineering, 1980.
- [78] P. Levesque, "Trends and patterns of United States fire losses," 2013.
- [79] J. Hall, "The total cost of fire in the United States," 2012.

- [80] L. Orloff, J. De Ris, and G. H. Markstein, "Upward turbulent fire spread and burning of fuel surface," *Symposium (International) on Combustion*, vol. 15, no. 1, pp. 183–192, Jan. 1975.
- [81] J. Quintiere, "The application of flame spread theory to predict material performance," *Journal of Research of the National Bureau of Standards*, vol. 1, pp. 91–70, 1988.
- [82] L. Zhou and A. C. Fernandez-Pello, "Solid fuel combustion in a forced, turbulent, flat plate flow: The effect of buoyancy," *Symposium (International) on Combustion*, vol. 24, no. 1, pp. 1721–1728, Jan. 1992.
- [83] V. B. Apte, R. W. Bilger, A. R. Green, and J. G. Quintiere, "Wind-aided turbulent flame spread and burning over large-scale horizontal PMMA surfaces," *Combustion and Flame*, vol. 85, no. 1–2, pp. 169–184, May 1991.
- [84] J. L. Consalvi, Y. Pizzo, and B. Porterie, "Numerical analysis of the heating process in upward flame spread over thick PMMA slabs," *Fire Safety Journal*, vol. 43, no. 5, pp. 351–362, Jul. 2008.
- [85] W. XIE and P. DESJARDIN, "An embedded upward flame spread model using 2D direct numerical simulations," *Combustion and Flame*, vol. 156, no. 2, pp. 522–530, Feb. 2009.
- [86] T. Tsuji and Y. Nagano, "Velocity and temperature measurements in a natural convection boundary layer along a vertical flat plate," *Experimental Thermal and Fluid Science*, vol. 2, no. 2, pp. 208–215, Apr. 1989.
- [87] T. Ahmad and G. M. Faeth, "Turbulent wall fires," *Symposium (International) on Combustion*, vol. 17, no. 1, pp. 1149–1160, Jan. 1979.
- [88] S. I. Stoliarov, S. Crowley, R. E. Lyon, and G. T. Linteris, "Prediction of the burning rates of non-charring polymers☆," *Combustion and Flame*, vol. 156, no. 5, pp. 1068–1083, May 2009.